Stochastic phase space methods for non-equilibrium systems

Alexander Joseph Muir McAlpine Ferrier

A dissertation submitted in partial fulfillment

of the requirements for the degree of

Doctor of Philosophy

of

University College London.

Department of Physics and Astronomy

University College London

October 26, 2021

I, Alexander Joseph Muir McAlpine Ferrier, confirm that the work presented in this thesis is my own. Where information has been derived from other sources, I confirm that this has been indicated in the work.

Publications

Parts of this thesis can be found in the following publications:

The work in chapter 3 is included in the publication [1] K. Dunnett, A. Ferrier, A. Zamora, G. Dagvadorj, and M. H. Szymanska, Properties of the signal mode in the polariton optical parametric oscillator regime, Phys. Rev. B **98**, 165307 (2018).

The work in chapter 4 has been submitted for publication, and can be found in preprint at [2] A. Ferrier, A. Zamora, G. Dagvadorj, and M. H. Szymanska, Searching for the kardar-parisi-zhang phase in microcavity polaritons, arXiv (2020), preprint, ArXiv:2009.05177.

Part of the work in chapter 5 is included in the publication [3] P. Deuar, A. Ferrier, M. Matuszewski, G. Orso, and M. H. Szymanska, Fully quantum scalable description of driven-dissipative lattice models, PRX Quantum **2**, 010319 (2021).

Abstract

This thesis details investigations in the use of stochastic phase space methods to study driven dissipative quantum systems. While these methods are useful in a wide array of physical contexts, the work I present here is primarily concerned with exciton-polaritons in semiconductor microcavities, quasiparticles that result from the strong coupling between photons confined to the cavity and excitons in the quantum well layer. Exciton-polaritons have all of the archetypal properties of open many-body quantum systems: driving by an external laser, dissipation from photons escaping the cavity, and nonlinearity from the interactions between excitons.

Two different stochastic phase space methods are explored in this thesis. The truncated Wigner method is a semiclassical method, in the sense that it neglects some quantum correlations, which is already widely used to simulate polariton systems. Here, I use it to study the optical parametric oscillator (OPO) regime, where polaritons from the driven mode scatter to coherently occupy additional modes. I first explore the variations in momentum structures in the OPO regime with the drive strength, before then studying the spatial correlations, finding the first numerical evidence of the 2D Kardar-Parisi-Zhang universality, a universality class unique to non-equilibrium systems, in polariton OPO.

I next employ the positive-P method, which provides fully quantum and scalable numerical simulations of open quantum systems. I investigate stronger quantum correlations that can arise from interference effects in driven-dissipative Bose-Hubbard Lieb lattices, using physical parameters accessible to current polariton micropillar experiments. Finally, I outline preliminary investigations into adapting the positive-P method to models with coupled bosons and qubits, relevant to experiments in superconducting circuit QED.

Impact Statement

Driven-dissipative quantum systems encompass many of the experimental platforms at the forefront of developments in quantum information technologies and quantum simulation, including cavity QED, circuit QED, quantum dots, arrays of coupled cavities and the focus of much of this thesis: exciton-polaritons in semiconductor microcavities. Keeping pace with and understanding new results within these fields requires appropriate numerical methods, particularly those scalable to large systems where direct exact solutions of quantum mechanics become intractable due to the exponentially growing complexity with system size. Stochastic phase space methods provide one direction by which this need can be met and, as is demonstrated in this thesis and related work by collaborators, are particularly well suited to systems where either or both external drive and/or dissipation are important factors.

The work in this thesis focuses on two different stochastic phase space methods, and broadly follows the recent shift in the focus of microcavity polariton experiments. The semiclassical truncated Wigner method is well established as a tool for studying non-equilibrium statistical physics in microcavity polariton systems; my truncated Wigner simulations of the polariton OPO regime continue this trend, culminating in the much sought after observation of the uniquely non-equilibrium behaviour described by the 2D Kardar-Parisi-Zhang universality class in a polariton system in chapter 4; this has been the subject of a plethora of recent analytical work, but has not been tested experimentally or numerically until now. Meanwhile, as polariton experiments move towards creating lattices with increased confinement and quantum correlations, we propose the positive-P method as an ideal numerical tool for studying the driven-dissipative lattice models implemented in these experiments. Examples provided by my work in chapter 5 demonstrate the accuracy and scalability of this method in situations with nontrivial quantum

correlations in parameter regimes relevant to polariton lattices. Through that work, I have also developed strong collaborations with researchers at the Institute of Physics, Polish Academy of Sciences, in Warsaw. By focusing on using physical parameters typical of current microcavity polariton experiments in both cases, I hope to inspire and enable experimental verifications of my main results, or related collaborations, in the near future. Additionally, with my work in chapter 6, I aim to begin the process of extending the positive-P method, and its wide array of benefits for driven-dissipative settings, to coupled spin-boson systems.

To disseminate my work within the scientific community, results produced for this thesis have been published in papers in *Physical Review B* and *PRX Quantum*, with a third paper submitted for publication and currently available in preprint.

Acknowledgements

For both useful and interesting discussions throughout my PhD, I would like to thank my supervisor Marzena Szymańska, and all the current and former members that I have shared my time in the group with: Galbadrakh Dagvadorj, Conor McKeever, Richard Juggins, Cristóbal Lledó, Paul Brookes, Igor Timofeev, Themistoklis Mavrogordatos, Paolo Comaron, and especially Alejandro Zamora, who collaborated with me on my first projects and guided me on all the basic technical things I needed to get started. I would like to thank Fabrizio Sidoli and the entire LCN IT support team: when one's research is primarily computational in nature, having competent and responsive technical support does not go unnoticed. For their guidance on the work of chapter 5, as well as their hospitality during my two visits to the Institute of Physics in Warsaw, I would like to thank Michał Matuszewski and Piotr Deuar; being able to interact with Piotr and his wealth of experience with stochastic phase space methods I feel has greatly accelerated my own practical knowledge with regards to the main subject of this thesis. I would also like to thank the experimental research groups of Jacqueline Bloch and Alberto Amo for useful discussions about the work of chapter 5 and relevant details of polariton micropillar experiments.

On more personal notes, I would like to thank my A level physics teacher, whose unyielding enthusiasm towards any former student of hers pursuing further education and beyond in physics has no doubt helped push me to my current position. Finally, and most importantly, I would like to thank my parents for continuing to provide for me well beyond what I would consider necessary, allowing me to spend the past few years with the task of completing my PhD as my only real source of anxiety.

Contents

List of Figures

List of Tables

Chapter 1

Introduction

Since the first introduction of what is now known as the Wigner function in 1932 [5], phase space methods have become an important tool for the understanding of quantum systems. While phase space methods have found many applications in closed systems [6–15], it is in the context of driven-dissipative quantum systems, such as are embodied by many photonic platforms now relevant to applications in quantum computation and simulation, that these methods truly flourish. This thesis will explore several applications of stochastic phase space methods, specifically the truncated Wigner method and the positive-P method, to problems involving driven-dissipative many-body quantum systems, primarily in the context of exciton-polaritons in semiconductor microcavities.

1.1 Exciton-polaritons in semiconductor microcavities

An archetypal driven-dissipative quantum system, and one which will serve as the physical context for most of the work in this thesis, is that of exciton-polaritons in semiconductor microcavities. I will use this section to overview the relevant physics of microcavity polariton systems.

1.1.1 Microcavities, quantum wells and the strong coupling limit

Polariton systems consist of two components: photons trapped in the microcavity and excitons trapped in the quantum well(s). The microcavity is made up of what are known as distributed Bragg reflectors, which are constructed from many alternating layers of semiconductor with different refractive indices to create a large overall reflectivity [16–18]. In a planar microcavity (i.e. one with a single pair of parallel reflectors), the momentum of

the photons is restricted along the direction perpendicular to the reflectors. If we consider how the energy, $\hbar\omega_C$, of photons trapped in the cavity varies with their wavevector $\boldsymbol{q}$:

$$\omega_C = \tilde{c}q = \tilde{c}\sqrt{q_z^2 + k^2}\,, \tag{1.1}$$

where q_z, the component of the wavevector perpendicular to the reflectors, is fixed, $\boldsymbol{k}$ is the in-plane wavevector, and $\tilde{c}$ here is the speed of light in the cavity. For small angles of incidence, that is $k \ll q_z$, we can expand in orders of k to give

$$\omega_C \approx \tilde{c}q_z + \frac{\tilde{c}k^2}{2q_z} = \omega_C(0) + \frac{\hbar k^2}{2m_C}\,. \tag{1.2}$$

The confinement of the photons by the cavity generates a small effective mass, $m_C = \hbar q_z/\tilde{c}$, for their motion in the plane of the cavity [17, 18].

A quantum well is a layer of semiconductor in which the electrons (and holes) are confined to move in two dimensions. Electrons in the quantum well can be excited from the valence band to the conduction band by the photons in the cavity. In the quantum well, the resulting conduction band electron and valence band hole can form a bound state called an exciton. Provided that the density of excitons does not become so large that the fermionic nature of the constituent electrons and holes must be taken into account, we can treat the excitons as bosonic particles in two dimensions, similar to the cavity photons. The excitons also have a parabolic dispersion with in-plane wavevector, $\omega_X = \omega_X(0) + \frac{\hbar k^2}{2m_X}$, albeit with a much larger mass than the cavity photons; exciton masses are of the order of the mass of an electron, while the effective mass of the photons can typically be around 10^5 times smaller [17]. Unlike photons, the excitons in the quantum well will interact with each other, which has important consequences for the behaviour of the polaritons.

The excitons can convert back into photons, resulting in a continuous coherent interconversion of photons and excitons in the cavity, i.e. Rabi oscillations with some frequency Ω_R. In the case where the $\hbar\Omega_R$ is much larger than other energy scales in the system, such as dissipation and the exciton-exciton interactions, we enter what is known as the strong coupling limit. It then becomes more convenient to treat the excitations

in the system as a hybridisation between the cavity photons and quantum well excitons, which are referred to as polaritons. The transformation from the exciton-photon basis to that of the upper and lower polaritons is given by

$$\begin{pmatrix} \hat{\Psi}_{LP}(\boldsymbol{k}) \\ \hat{\Psi}_{UP}(\boldsymbol{k}) \end{pmatrix} = \begin{pmatrix} X(\boldsymbol{k}) & C(\boldsymbol{k}) \\ -C(\boldsymbol{k}) & X(\boldsymbol{k}) \end{pmatrix} \begin{pmatrix} \hat{\Psi}_X(\boldsymbol{k}) \\ \hat{\Psi}_C(\boldsymbol{k}) \end{pmatrix}, \tag{1.3}$$

where $X(\boldsymbol{k})$, $C(\boldsymbol{k})$ are known as the Hopfield coefficients [19], and are such as to diagonalise the Hamiltonian

$$\hat{H}_{XC} = \hbar \sum_{\boldsymbol{k}} \begin{pmatrix} \hat{\Psi}_X^\dagger(\boldsymbol{k}) & \hat{\Psi}_C^\dagger(\boldsymbol{k}) \end{pmatrix} \begin{pmatrix} \omega_X(\boldsymbol{k}) & \frac{\Omega_R}{2} \\ \frac{\Omega_R}{2} & \omega_C(\boldsymbol{k}) \end{pmatrix} \begin{pmatrix} \hat{\Psi}_X(\boldsymbol{k}) \\ \hat{\Psi}_C(\boldsymbol{k}) \end{pmatrix}. \tag{1.4}$$

This Hamiltonian describes the exciton-photon system before considering the external drive, dissipation or exciton-exciton interactions, where $\hat{\Psi}^\dagger_{X,C}(\boldsymbol{k})$,$\hat{\Psi}_{X,C}(\boldsymbol{k})$ are the creation and annihilation operators for excitons (X) or photons (C) with in-plane wavevector $\boldsymbol{k}$. The resulting upper/lower polariton dispersions are

$$\omega_{UP,LP} = \frac{1}{2}\left(\omega_C + \omega_X \pm \sqrt{(\omega_C - \omega_X)^2 + \Omega_R^2}\right). \tag{1.5}$$

An example of these dispersions, alongside a rough diagram of the microcavity polariton system, is shown in Fig. 1.1. An additional convenience of the polariton formalism is that in many situations, such as those considered in this thesis, the upper polariton branch is often practically unoccupied, allowing us to further simplify our theoretical description to one containing only one field: the lower polaritons [20, 21].

1.1.2 Driving and the optical parametric oscillator regime

Defining features of the physics of microcavity polaritons are drive and decay. Since photons can escape from the cavity, as well as due to the decay of excitons by non-radiative means, polaritons are constantly lost from the system. This means that in order to maintain a finite population of polaritons in the system, it must be driven externally by a laser. There are two categories of driving that are used in experiments: coherent pumping and incoherent pumping. In the incoherently pumped case, polaritons are injected into the sys-

tem, for example by driving with a laser tuned far above the lower polariton dispersion, and relax to produce a large population near the bottom of the lower polariton dispersion [22–24]. In coherent pumping, a laser is tuned to be resonant with, or close to resonant with, the lower polariton dispersion, resulting in a large occupation of polaritons with wavevector $\boldsymbol{k}$ corresponding to the driving laser (the pump state). Unlike in the incoherently pumped case, the phase of the polaritons is locked to that of the driving laser.

A special case of the coherently driven system can occur when the driving laser is tuned near the point of inflection of the lower polariton dispersion. Due to the strong polariton-polariton interactions inherited from their excitonic component, as well as the peculiar shape of the lower polariton dispersion, pairs of polaritons in the pump state can scatter from each other to occupy two other states, conventionally named the signal and idler for the state below/above the pump in momentum respectively, in a way that is triply resonant, while conserving energy and momentum ($2\boldsymbol{k}_p = \boldsymbol{k}_s + \boldsymbol{k}_i$, $2\omega_p = \omega_s + \omega_i$ where p, s, i denote the pump, signal, idler). Between certain thresholds in pump power, this results in the appearance of (at least) two additional largely occupied modes and is known as the optical parametric oscillator (OPO) regime [25–28], in analogy to similar situations in nonlinear optics.

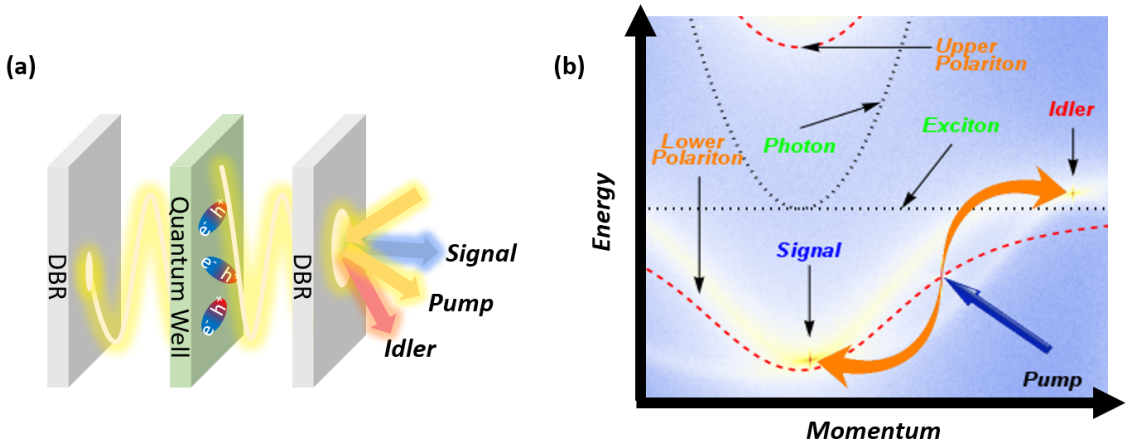

Figure 1.1: (a) Diagram of polaritons in a semiconductor microcavity, with coherently driven pump mode scattering into signal and idler modes. (b) An example of exciton and photon dispersions and the corresponding upper and lower polariton dispersions, showing signal, pump and idler modes (spectrum image courtesy of Galbadrakh Dagvadorj).

1.1.3 Coherence and order in polariton systems

Since the polaritons are bosons, many polaritons can occupy the same state. In equilibrium systems, such as liquid helium and cold atomic gases, this leads to effects such as Bose-Einstein condensation (BEC) and superfluidity. Polaritons provide a useful platform for exploring if and how these effects occur in systems that are both two dimensional, and out of thermal equilibrium.

Superfluidity is most commonly known for dissipationless flow, but also has a number of other defining properties such as irrotationality and the possibility of forming quantised vortices (points around which the phase rotates by an integer multiple of 2π) [29]. Experiments have separately demonstrated many of these properties in various regimes of polaritons. The first of these was the demonstration of reduced scattering of a coherently pumped polariton fluid from a defect [30]. Since then the creation of 'bullets' of polaritons that flow without friction [31], as well as vortices and persistent currents [32], have been demonstrated within the OPO regime. Additionally, vortices have been observed in the incoherently driven case [33], and the presence of a superfluid (i.e. irrotational) fraction has been confirmed theoretically [34].

Intrinsically linked with superfluidity is the idea of off-diagonal long range order [35]. This is where spatial correlations $\langle\hat{\Psi}^\dagger(\boldsymbol{r})\hat{\Psi}(\boldsymbol{r}')\rangle$ remain non-zero as $|\boldsymbol{r}-\boldsymbol{r}'|\to\infty$, as occurs, for example, in BEC. While true off-diagonal long range order cannot occur in two dimensional systems beyond zero temperature [36], there have been many cases observed where, in the small system sizes of actual microcavities, order effectively extends over the entire system [17]. Further investigations reveal that the true nature of the ordering that occurs in polariton systems is something more similar to the Berezinskii–Kosterlitz–Thouless (BKT) transition [37–39], where the transition from a disordered state, with exponentially decaying spatial correlations, to a quasi-ordered state, with spatial correlations that decay algebraically with distance, is mediated by the binding of vortex-antivortex pairs [40]. Truncated Wigner simulations have been used to show that this transition is indeed driven by vortex binding in polariton systems [37, 39], and have studied the phase ordering behavour [41, 42]. While state of the art experiments have reached the limit of thermal equilibrium in polaritons and show the expected equilib-

rium BKT behaviour [37], other studies further from equilibrium show deviations, such as faster algebraic decay in the quasi-ordered phase than is allowed by equilibrium BKT, that are indicative of the non-equilibrium nature of the system [38, 39]. Expanding from the latter case, recent theoretical work has established connections between polariton systems and a distinctly non-equilibrium class of universal behaviour known as the Kardar-Parisi-Zhang (KPZ) universality [43, 44], as will be discussed further in chapter 4, although experimental verifications of this have yet to be achieved.

1.1.4 Polariton lattices

A more recent development in polariton experiments is to form lattices to further confine the polaritons [45–64]. A number of different ways of creating lattice potentials for microcavity polaritons have been implemented. For example, depositing a thin layer of metal, usually gold, on top of select regions of the microcavity locally increases the photon energy, confining the polaritons to the regions without the metal layer [47, 48]. Stronger trapping potentials have been made by surface acoustic waves applied to the microcavity; this creates a periodic potential for both the excitons and the photons, due to the modulations caused in the strain in the quantum well, and both the length and refractive index of the cavity, respectively [46, 49, 50].

One of the most explored ways of generating strong lattice potentials for the polaritons is through the direct etching of the microcavity into structures known as micropillars [45, 51–60, 64]. Micropillar lattices have been implemented in a wide array of geometries with interesting physical properties. These include the 1D Su-Schrieffer-Heeger model (a 1D chain that has alternating values of the hopping strength between adjacent sites) with topological edge modes [55], 2D honeycomb lattices (i.e. graphene) [57, 60], which have also been engineered with strong artificial magnetic fields induced by spatial variation of the lattice spacing [64], and both quasi-1D and 2D Lieb lattices (see chapter 5 for details and diagrams), which exhibit a flat band due to destructive interference preventing the motion of particles through the lattice [54, 56, 58, 59].

1.2 Overview of phase space methods

The application of phase space methods in quantum mechanics involves converting from the formalism of operators, to one of functions of some phase space variables. This section will give a broad conceptual overview of what phase space methods are and how they work. Chapter 2 will give the standard derivations of the specific methods I use in my work, while chapter 6 will include similar derivations for new methods I have begun developing for systems of coupled spins and bosons.

1.2.1 Coherent states and phase space

While Wigner originally used a phase space of position and momentum [5], as is traditional from classical phase space methods, a more common approach in modern applications is to instead use the coherent state basis for bosonic systems. For a bosonic mode with creation and annihilation operators $\hat{a}^\dagger$ and $\hat{a}$ respectively, with $[\hat{a},\hat{a}^\dagger]=1$, the coherent states $|\alpha\rangle$ are defined as

$$|\alpha\rangle = e^{-\frac{1}{2}|\alpha|^2} e^{\alpha\hat{a}^\dagger}|0\rangle\,, \tag{1.6}$$

where $|0\rangle$ is the vacuum state, and are the eigenstates of the annihilation operator $\hat{a}|\alpha\rangle = \alpha|\alpha\rangle$ [65]. We can then define the phase space used for our methods using the complex number(s) α for each mode in the system [6, 65–70].

The key step in generating any phase space representation is the mapping from the density operator $\hat{\rho}$, which describes the state of the system, to a (quasi)probability distribution $P(\alpha)$ over the phase space variables. There are a number of choices for how this can be performed, which lead to a selection of different phase space representations such as the Wigner [5] representation or the P representation [66, 67], and futher generalisations of this such as the positive-P representation [69] can provide additional benefits. In general, the properties of our mapping onto the phase space representation will allow us to convert from the equation for evolution of the density operator $\hat{\rho}$, typically of the form of a Gorini-Kossakowski-Sudarshan-Lindblad (GKSL) master equation for open quantum systems such as those studied in this thesis, to an equation for the evolution of the distribution $P(\alpha)$. Either directly, as is the case for the positive-P distribution [69–71], or after

appropriate approximations in the case of truncated Wigner [6, 65–68], this will take the form of a Fokker-Planck equation, which can be converted to stochastic differential equations for trajectories of the phase space variables α which sample the distribution $P(\alpha)$. These can be solved numerically, and quantum mechanical observables can be calculated by averaging corresponding products of phase space variables over many realisations, for example as given by Fig. 1.2 (f). This is the essence of stochastic phase space methods.

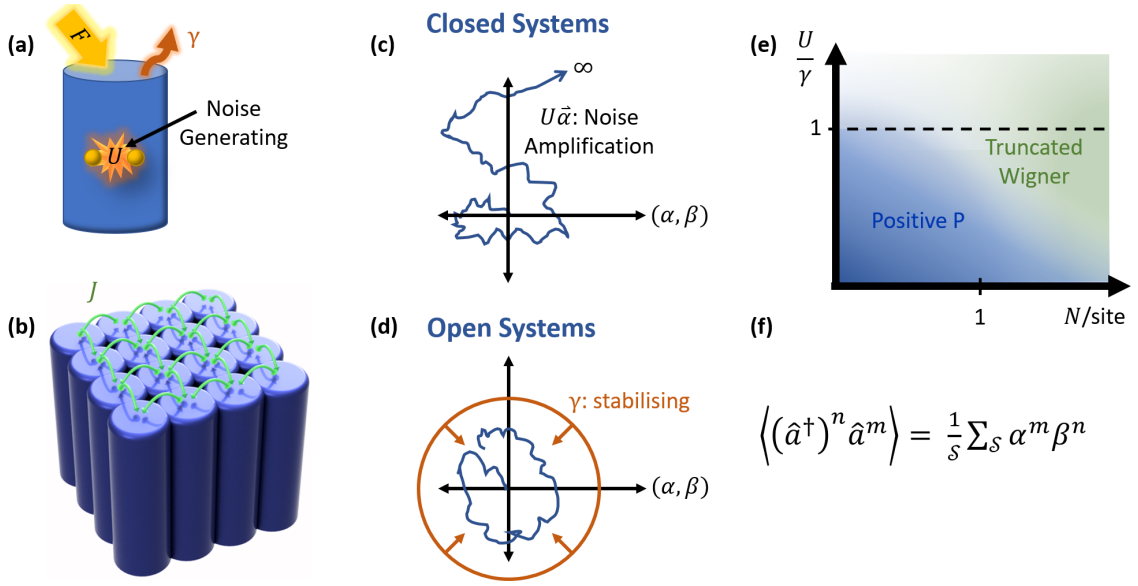

Figure 1.2: Illustration of the application of the positive-P method to the driven-dissipative Bose-Hubbard model. (a) Single site with coherent drive F, dissipation γ, and local interactions U, which generate the noise terms. (b) Example of a 2D lattice with hopping J between sites. (c) In closed systems, noise self amplifies, causing trajectories to eventually escape to infinity. (d) In open systems, dissipation has the effect of stabilising the trajectories. (e) Sketch of relative regimes of usefulness of truncated Wigner and positive-P methods (see Fig. 1.3 for details). (f) Quantum mechanical observables are calculated by averaging appropriate products of phase space variables over stochastic realisations.

1.2.2 Applications of phase space methods to driven-dissipative systems

In some of their earliest applications in quantum optics, phase space methods were used to treat driven-dissipative models with a single bosonic mode [68, 72]. In the context of microcavity polaritons, the truncated Wigner method was first used in [73]. Since then, the truncated Wigner method has achieved extensive use in this field for the study of order and correlations in polariton condensates and OPO [39, 41, 42, 74] and has become the

go-to numerical method for direct comparison with microcavity polariton experiments [37, 75–77].

While the positive-P method has been used for closed systems [13–15], there is a known issue with its applicability to such systems, as the self amplification of the noise by nonlinear terms eventually makes it impossible to obtain useful results at long times [70, 71]. As such, the positive-P method turns out to be much better suited to driven-dissipative systems, where it is known that sufficiently strong dissipation can completely stabilise the stochastic trajectories against the onset of this noise amplification catastrophe [3, 71], allowing both dynamics and steady state behaviour to be simulated. In [3], to which some of the work in this thesis is contributed, we thoroughly characterised the regimes of usefulness of the positive-P method in the parameter space of the driven-dissipative Bose-Hubbard model.

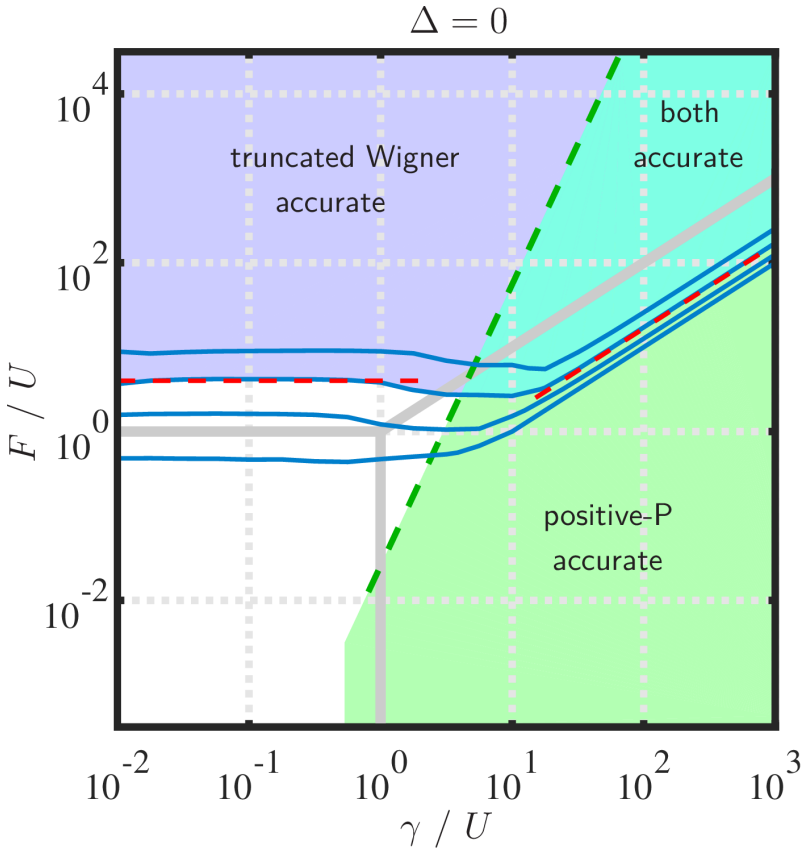

Figure 1.3: Comparison of the regimes of usefulness of the truncated Wigner and positive-P methods for the driven-dissipative Bose-Hubbard model. Reproduced with permission from [3].

A conceptual summary of our results in [3] is illustrated by Fig. 1.2. In particular, we found that, under sufficiently dissipative conditions, the positive-P method provides a powerful tool for performing fully quantum numerical simulations of the driven-dissipative Bose-Hubbard model, which is both capable of capturing nontrivial quantum correlations and scalable to systems with large numbers of sites. The regimes of validity of the positive-P and truncated Wigner methods were also found to be complementary, with the truncated Wigner method being accurate for large occupations and the positive-P method being numerically stable for strong dissipation (see Fig. 1.3). My direct contributions to [3] in terms of numerical results, along with follow up work, are given in chapter 5.

1.3 Summary of contributions

To close this introductory chapter, I will give a brief overview of the main results which are detailed in the rest of this thesis, and their implications in the context of the background presented here. Chapters 3 and 4 concern truncated Wigner simulations of the polariton OPO. Chapter 3 focuses on the different momentum structures that can occur in the OPO regime when varying the strength of the external drive. The results therein can also be found published in [1]. This work explores the relation between the common three-mode analytical descriptions of the OPO regime and the behaviour observed in my simulations, which do not restrict how many modes can become occupied by the scattering processes. In particular, it determines at which pump strengths the three-mode description is valid and where it breaks down. These results are important for comparing analytical studies of OPO to real or numerical experiments, for example the subsequent work in chapter 4. Continuing the study of the nature of coherence and order in the polariton OPO regime, the work in chapter 4 investigates connections between the polariton OPO regime and the Kardar-Parisi-Zhang (KPZ) universality. A previous analytical study of this connection [44] predicted that, for specific values of the pump strength, the polariton OPO system should display signatures of the KPZ universality. Using truncated Wigner simulations I show that, at those pump strengths, spatial correlations take a form mostly consistent with the appearance of the KPZ scaling phase, and also rule out the

alternative possibility of a vortex dominated phase due to alterations to vortex-vortex interactions under the KPZ equation [78, 79]. This work can be found in preprint at [2].

The aforementioned work in [3] demonstrates the use of the positive-P method in simulating the driven-dissipative Bose-Hubbard model. My specific contributions to the results presented there, given in chapter 5, focus on reproducing results showing strong bunching of local second order correlations resulting from interference on the dark sites of a Lieb lattice [4] using the positive-P method, as well as its scalability to systems much larger than achieved in that reference. Further work in chapter 5 explores the altering of these interference effects to instead produce antibunching, which is often taken as a sign of quantum correlations due to being impossible to reproduce with purely classical physics, and the optimisation of such effects for regimes accessible to current polariton micropillar experiments. Finally, in chapter 6, I investigate how the positive-P method may be extended to models with coupled spins and bosons, such as the driven-dissipative Jaynes-Cummings-Hubbard model, which in future may allow for the strengths of the positive-P method to be applied to studying appropriate parameter regimes of many systems of this kind in cavity and circuit QED.

Chapter 2

Derivations of phase space methods for polaritons

In this chapter I will give detailed derivations that lead to the stochastic differential equations that are solved in the simulations considered in later chapters. While these derivations are fairly standard, I include them here for completeness, and in order to define my methods fully.

2.1 Truncated Wigner for the lower polariton model

This section concerns the method I use to produce the results presented in chapters 3 and 4. Here, I will introduce the Wigner representation and the truncated Wigner approximation (TWA) in detail, and show how it is used to generate the stochastic differential equations I solve numerically for those projects.

2.1.1 The Wigner representation for a single mode

I will begin by introducing the fundamental principles of the Wigner representation for the simplest case of a single bosonic mode. For a single bosonic mode, we can define the Wigner quasiprobability distribution as a Fourier transform of a corresponding characteristic function χ_W defined as the expectation value of a displacement operator $\hat{D}$ [65, 68].

In full, this is given by

$$\begin{aligned} W(\alpha,\alpha^*) &= \frac{1}{\pi^2}\int d^2\lambda\ \chi_W(\lambda,\lambda^*)e^{\lambda^*\alpha-\lambda\alpha^*}, \\ \chi_W(\lambda,\lambda^*) = \mathrm{Tr}[\hat{\rho}\hat{D}] &= \frac{1}{\pi^2}\int d^2\alpha\ W(\alpha,\alpha^*)e^{\lambda\alpha^*-\lambda^*\alpha}, \\ \hat{D} &= e^{\lambda\hat{a}^\dagger-\lambda^*\hat{a}}, \end{aligned} \tag{2.1}$$

where the integrals here are over the entire complex plane. The characteristic function $\chi_W(\lambda,\lambda^*)$ can be used to generate the operator correspondences [65, 68], sometimes also referred to as Bopp operators [6], that can be used to convert between creation/annihilation operators acting on the density operator to differential operators of the phase space variables acting on the quasiprobability distribution. We do this by considering derivatives of the characteristic function. For example, let us first consider

$$\frac{\partial\chi_W}{\partial\lambda} = \mathrm{Tr}[\hat{\rho}\frac{\partial\hat{D}}{\partial\lambda}] = \frac{1}{\pi^2}\int d^2\alpha\ W(\alpha,\alpha^*)\frac{\partial}{\partial\lambda}e^{\lambda\alpha^*-\lambda^*\alpha}.$$

Using the Baker-Campbell-Hausdorff formula, we can rewrite $\hat{D}$ in two other ways [65]:

$$\hat{D} = e^{\lambda\hat{a}^\dagger}e^{-\lambda^*\hat{a}}e^{-\frac{1}{2}|\lambda|^2} = e^{-\lambda^*\hat{a}}e^{\lambda\hat{a}^\dagger}e^{\frac{1}{2}|\lambda|^2}. \tag{2.2}$$

If we use the first of these two options we can proceed in the following way:

$$\begin{aligned} \mathrm{Tr}[\hat{\rho}\frac{\partial}{\partial\lambda}\left(e^{\lambda\hat{a}^\dagger}e^{-\lambda^*\hat{a}}e^{-\frac{1}{2}|\lambda|^2}\right)] &= \frac{1}{\pi^2}\int d^2\alpha\ W(\alpha,\alpha^*)\alpha^*e^{\lambda\alpha^*-\lambda^*\alpha}, \\ \mathrm{Tr}[\hat{\rho}(\hat{a}^\dagger-\frac{1}{2}\lambda^*)\hat{D}] &= \frac{1}{\pi^2}\int d^2\alpha\ W(\alpha,\alpha^*)\alpha^*e^{\lambda\alpha^*-\lambda^*\alpha}, \\ \mathrm{Tr}[\hat{\rho}\hat{a}^\dagger\hat{D}]-\frac{1}{2}\lambda^*\chi_W &= \frac{1}{\pi^2}\int d^2\alpha\ \alpha^*W(\alpha,\alpha^*)\alpha^*e^{\lambda\alpha^*-\lambda^*\alpha}, \\ \mathrm{Tr}[\hat{\rho}\hat{a}^\dagger\hat{D}] &= \frac{1}{\pi^2}\int d^2\alpha\ W(\alpha,\alpha^*)(\alpha^*-\frac{1}{2}\frac{\partial}{\partial\alpha})e^{\lambda\alpha^*-\lambda^*\alpha}, \end{aligned} \tag{2.3}$$

where in the final line we have used that $\lambda^*e^{\lambda\alpha^*-\lambda^*\alpha} = -\frac{\partial}{\partial\alpha}e^{\lambda\alpha^*-\lambda^*\alpha}$. Integrating by parts at this stage, provided that $W(\alpha,\alpha^*)$ falls off sufficiently fast as $\alpha\to\infty$ that we can

neglect the boundary terms, gives the final step

$$\mathrm{Tr}[\hat{\rho}\hat{a}^{\dagger}\hat{D}] = \frac{1}{\pi^2}\int d^2\alpha\, e^{\lambda\alpha^* - \lambda^*\alpha}(\alpha^* + \frac{1}{2}\frac{\partial}{\partial\alpha})W(\alpha,\alpha^*)\,, \tag{2.4}$$

which can be summarised as the operator correspondence $\hat{\rho}\hat{a}^{\dagger} \leftrightarrow (\alpha^* + \frac{1}{2}\frac{\partial}{\partial\alpha})W$. If we instead use the second way of writing $\hat{D}$ in (2.2) we can use similar steps to produce a different operator correspondence

$$\begin{aligned}
\mathrm{Tr}[\hat{\rho}\frac{\partial}{\partial\lambda}\left(e^{-\lambda^*\hat{a}}e^{\lambda\hat{a}^{\dagger}}e^{\frac{1}{2}|\lambda|^2}\right)] &= \frac{1}{\pi^2}\int d^2\alpha\, W(\alpha,\alpha^*)\alpha^* e^{\lambda\alpha^* - \lambda^*\alpha}\,,\\
\mathrm{Tr}[\hat{\rho}\hat{D}(\hat{a}^{\dagger} + \frac{1}{2}\lambda^*)] &= \frac{1}{\pi^2}\int d^2\alpha\, W(\alpha,\alpha^*)\alpha^* e^{\lambda\alpha^* - \lambda^*\alpha}\,,\\
\mathrm{Tr}[\hat{a}^{\dagger}\hat{\rho}\hat{D}] + \frac{1}{2}\lambda^*\chi_W &= \frac{1}{\pi^2}\int d^2\alpha\, \alpha^* W(\alpha,\alpha^*)\alpha^* e^{\lambda\alpha^* - \lambda^*\alpha}\,,\\
\mathrm{Tr}[\hat{a}^{\dagger}\hat{\rho}\hat{D}] &= \frac{1}{\pi^2}\int d^2\alpha\, W(\alpha,\alpha^*)(\alpha^* + \frac{1}{2}\frac{\partial}{\partial\alpha})e^{\lambda\alpha^* - \lambda^*\alpha}\,,\\
\mathrm{Tr}[\hat{a}^{\dagger}\hat{\rho}\hat{D}] &= \frac{1}{\pi^2}\int d^2\alpha\, e^{\lambda\alpha^* - \lambda^*\alpha}(\alpha^* - \frac{1}{2}\frac{\partial}{\partial\alpha})W(\alpha,\alpha^*)\,,
\end{aligned} \tag{2.5}$$

where we have also invoked the cyclicity of the trace for rearranging the left hand side between the second and third lines. Between the above, and the equivalent constructions for $\frac{\partial\chi_W}{\partial\lambda^*}$, we find a set of four operator correspondences in total, for applying $\hat{a}$ or $\hat{a}^{\dagger}$ to $\hat{\rho}$ from either side, which can also be applied recursively to convert any operator as a product of creation and annihilation operators applied to the density operator to the Wigner representation. These are given by:

$$\hat{a}\hat{A}[\hat{\rho}] \leftrightarrow \left(\alpha + \frac{1}{2}\frac{\partial}{\partial\alpha^*}\right)\tilde{A}[W(\alpha,\alpha^*)]\,, \tag{2.6a}$$

$$\hat{a}^{\dagger}\hat{A}[\hat{\rho}] \leftrightarrow \left(\alpha^* - \frac{1}{2}\frac{\partial}{\partial\alpha}\right)\tilde{A}[W(\alpha,\alpha^*)]\,, \tag{2.6b}$$

$$\hat{A}[\hat{\rho}]\hat{a} \leftrightarrow \left(\alpha - \frac{1}{2}\frac{\partial}{\partial\alpha^*}\right)\tilde{A}[W(\alpha,\alpha^*)]\,, \tag{2.6c}$$

$$\hat{A}[\hat{\rho}]\hat{a}^{\dagger} \leftrightarrow \left(\alpha^* + \frac{1}{2}\frac{\partial}{\partial\alpha}\right)\tilde{A}[W(\alpha,\alpha^*)]\,, \tag{2.6d}$$

with the notation $\hat{A}[\hat{\rho}]$ being shorthand for any operator that acts from either or both sides on $\hat{\rho}$, and $\tilde{A}[W(\alpha,\alpha^*)]$ being the equivalent differential operator of the phase space

variables acting on $W(\alpha,\alpha^*)$. In this way we are able to convert the GKSL master equation for the time evolution of $\hat{\rho}$ to an equation for the time evolution of the Wigner distribution $W(\alpha,\alpha^*)$.

2.1.2 The master equation and evolution of the Wigner distribution

To demonstrate how this works, and eventually what is meant by the truncated Wigner approximation, I will now cover the example of the lower polariton model that leads to the equation used for my simulations. The starting point for this will be a GKSL master equation for the lower polariton model (2.8) [18]. The GKSL master equation is the general form of the evolution of $\hat{\rho}$ when assuming Markovian dissipation, meaning that the dissipation at each time is unaffected by the state of the system at previous times, allowing the evolution of the system to be expressed in terms of a single time parameter t. The Markovian approximation is valid provided that the rate of the coupling between the system and the external bath (the dissipation rate) is slow compared to the frequencies of the bath modes i.e. of the photons escaping the cavity [65]. This will normally be the case for the sorts of semiconductor microcavities being modelled in my work [18].

I consider a finite system size $L\times L$, which results in discrete momentum modes $\boldsymbol{k}=2\pi\boldsymbol{n}/L$, where the components of $\boldsymbol{n}$, n_x,n_y, are integers. Also, to aid in simulating the system computationally and avoid attempting to consider an infinite number of momentum modes, I discretise space on an $N\times N$ grid, with area element $dV=L^2/N^2$. This is equivalent to enforcing a momentum cutoff $k_{max}=2\pi N/L=2\pi/\sqrt{dV}$, and we will see below that it plays a role in justifying the TWA in this model. From this point on, I will simplify the notation $\hat{\Psi}(\boldsymbol{k})\equiv\hat{\Psi}_{LP}(\boldsymbol{k})$. Additionally, operators with momentum arguments are related to those with spatial arguments by a two dimensional discrete Fourier transform

$$\hat{\Psi}(\boldsymbol{k})=\frac{\sqrt{dV}}{N}\sum_{\boldsymbol{x}}e^{i\boldsymbol{k}\cdot\boldsymbol{x}}\hat{\Psi}(\boldsymbol{x})\,,\ \hat{\Psi}(\boldsymbol{x})=\frac{1}{N\sqrt{dV}}\sum_{\boldsymbol{k}}e^{-i\boldsymbol{k}\cdot\boldsymbol{x}}\hat{\Psi}(\boldsymbol{k})\,. \tag{2.7}$$

The GKSL master equation is given by

$$\frac{\partial\hat{\rho}}{\partial t}=-\frac{i}{\hbar}\left[\hat{H},\hat{\rho}\right]+\kappa\sum_{\boldsymbol{k}}2\hat{\Psi}(\boldsymbol{k})\hat{\rho}\hat{\Psi}^\dagger(\boldsymbol{k})-\hat{\Psi}^\dagger(\boldsymbol{k})\hat{\Psi}(\boldsymbol{k})\hat{\rho}-\hat{\rho}\hat{\Psi}^\dagger(\boldsymbol{k})\hat{\Psi}(\boldsymbol{k})\,, \tag{2.8}$$

where

$$\begin{aligned}
\hat{H} &= \hat{H}_{LP} + \hat{H}_{int} + \hat{H}_{pump}\,, \\
\hat{H}_{LP} &= \hbar \sum_{\boldsymbol{k}} \omega_{LP}(\boldsymbol{k}) \hat{\Psi}^{\dagger}(\boldsymbol{k}) \hat{\Psi}(\boldsymbol{k})\,, \\
\hat{H}_{int} &= \frac{\hbar g}{2} dV \sum_{\boldsymbol{x}} \hat{\Psi}^{\dagger}(\boldsymbol{x}) \hat{\Psi}^{\dagger}(\boldsymbol{x}) \hat{\Psi}(\boldsymbol{x}) \hat{\Psi}(\boldsymbol{x})\,, \\
\hat{H}_{pump} &= \hbar dV \sum_{\boldsymbol{x}} F_p(\boldsymbol{x},t) \hat{\Psi}^{\dagger}(\boldsymbol{x}) + F_p^*(\boldsymbol{x},t) \hat{\Psi}(\boldsymbol{x})\,,
\end{aligned}$$

g is the polariton-polariton interaction strength, κ is the dissipation rate, and the coherent pump has a plane wave form $F_p(\boldsymbol{x},t) = \tilde{f}_p e^{i(\boldsymbol{k}_p \cdot \boldsymbol{x} - \omega_p t)}$.

The operator correspondences for the momentum modes take the same form as given in (2.6) for each mode's phase space variable $\Psi(\boldsymbol{k},t)$. To obtain the equivalent expressions for the phase space variables $\Psi(\boldsymbol{x},t)$ of the spatial modes we can use the Fourier transforms

$$\begin{aligned}
\Psi(\boldsymbol{k},t) &= \frac{\sqrt{dV}}{N} \sum_{\boldsymbol{x}} e^{i\boldsymbol{k}\cdot\boldsymbol{x}} \Psi(\boldsymbol{x},t)\,,\ \Psi(\boldsymbol{x},t) = \frac{1}{N\sqrt{dV}} \sum_{\boldsymbol{k}} e^{-i\boldsymbol{k}\cdot\boldsymbol{x}} \Psi(\boldsymbol{k},t)\,, \\
\frac{\partial}{\partial \Psi(\boldsymbol{x},t)} &= \frac{\sqrt{dV}}{N} \sum_{\boldsymbol{k}} e^{i\boldsymbol{k}\cdot\boldsymbol{x}} \frac{\partial}{\Psi(\boldsymbol{k},t)}\,,\ \frac{\partial}{\partial \Psi(\boldsymbol{k},t)} = \frac{1}{N\sqrt{dV}} \sum_{\boldsymbol{x}} e^{-i\boldsymbol{k}\cdot\boldsymbol{x}} \frac{\partial}{\Psi(\boldsymbol{x},t)}\,,
\end{aligned} \tag{2.9}$$

leading to

$$\hat{\Psi}(\boldsymbol{x}) \hat{A}[\hat{\rho}] \leftrightarrow \left(\Psi(\boldsymbol{x},t) + \frac{1}{2dV} \frac{\partial}{\partial \Psi^*(\boldsymbol{x},t)} \right) \tilde{A}[W]\,, \tag{2.10a}$$

$$\hat{\Psi}^{\dagger}(\boldsymbol{x}) \hat{A}[\hat{\rho}] \leftrightarrow \left(\Psi^*(\boldsymbol{x},t) - \frac{1}{2dV} \frac{\partial}{\partial \Psi(\boldsymbol{x},t)} \right) \tilde{A}[W]\,, \tag{2.10b}$$

$$\hat{A}[\hat{\rho}] \hat{\Psi}(\boldsymbol{x}) \leftrightarrow \left(\Psi(\boldsymbol{x},t) - \frac{1}{2dV} \frac{\partial}{\partial \Psi^*(\boldsymbol{x},t)} \right) \tilde{A}[W]\,, \tag{2.10c}$$

$$\hat{A}[\hat{\rho}] \hat{\Psi}^{\dagger}(\boldsymbol{x}) \leftrightarrow \left(\Psi^*(\boldsymbol{x},t) + \frac{1}{2dV} \frac{\partial}{\partial \Psi(\boldsymbol{x},t)} \right) \tilde{A}[W]\,. \tag{2.10d}$$

Applying these to equation (2.8) and converting all terms to real space gives an equation for the time evolution of the Wigner distribution of the polariton system. Details of this are given in appendix A. Ultimately, this gives the complete evolution equation for the

Wigner distribution as [18]

$$\frac{\partial W}{\partial t} = \sum_{\boldsymbol{x}} \left(-\frac{\partial}{\partial \Psi} \left\{ \left[\left(-i\omega_{LP}(-i\boldsymbol{\nabla}) - ig\left(|\Psi|^2 - \frac{1}{dV} \right) - \kappa \right) \Psi - iF_p \right] W \right\} \right.$$
$$- \frac{\partial}{\partial \Psi^*} \left\{ \left[\left(i\omega_{LP}(-i\boldsymbol{\nabla}) + ig\left(|\Psi|^2 - \frac{1}{dV} \right) - \kappa \right) \Psi^* + iF_p^* \right] W \right\}$$
$$\left. + \frac{\kappa}{dV} \frac{\partial^2 W}{\partial \Psi^* \partial \Psi} + \frac{ig}{4dV^2} \frac{\partial^2}{\partial \Psi^* \partial \Psi} \left\{ \frac{\partial}{\partial \Psi^*} [\Psi^* W] - \frac{\partial}{\partial \Psi} [\Psi W] \right\} \right) , \quad (2.11)$$

where for brevity we have suppressed the arguments here for $\Psi \equiv \Psi(\boldsymbol{x},t)$, $F_p \equiv F_p(\boldsymbol{x},t)$, and their complex conjugates.

2.1.3 The truncated Wigner approximation

Equation (2.11) looks like a Fokker-Planck equation except for the final third order derivative terms. If the third order terms can be neglected, then the Wigner function obeys a Fokker-Planck equation and therefore evolves like a classical probability distribution. This is the truncated Wigner approximation (TWA). In this case, we can find an equation for distinct stochastic trajectories of the phase space variables $\Psi(\boldsymbol{x},t)$ [18, 39, 73]. The first order derivative terms (drift terms) in the Fokker-Planck equation give the deterministic part of the evolution of $\Psi(\boldsymbol{x},t)$, while the second order derivative term (diffusion term) gives the stochastic part of the evolution of $\Psi(\boldsymbol{x},t)$. Specifically, for a general Fokker-Planck equation of the form

$$\frac{\partial P(\boldsymbol{v})}{\partial t} = \sum_j -\frac{\partial}{\partial v_j} \left(A_j(\boldsymbol{v}) P(\boldsymbol{v}) \right) + \sum_{j,j'} \frac{\partial^2}{\partial v_j \partial v_{j'}} \left(\frac{1}{2} D_{j,j'}(\boldsymbol{v}) P(\boldsymbol{v}) \right) , \quad (2.12)$$

where $P(\boldsymbol{v})$ is a probability distribution over some set of variables $\boldsymbol{v}$, and $A_j(\boldsymbol{v})$, $D_{j,j'}(\boldsymbol{v})$ are the components of the drift vector and diffusion matrix respectively, the corresponding stochastic differential equations that generate trajectories of the variables $\boldsymbol{v}$ are

$$\frac{\partial v_j}{\partial t} = A_j(\boldsymbol{v}) + \sum_{j'} B_{j,j'}(\boldsymbol{v}) \xi_{j'}(t) , \quad (2.13)$$

with uncorrelated real zero mean Gaussian noises $\xi_j(t)$ with $\langle \xi_j(t) \xi_{j'}(t') \rangle = \delta_{j,j'} \delta(t-t')$ [65, 80]. The matrix B is a (generally non-unique) decomposition of the diffusion matrix

chosen such that $D = BB^T$.

For the Fokker-Planck equation given after applying the TWA to (2.11), the diffusion matrix in the space of (Ψ, Ψ^*) is

$$D = \frac{\kappa}{dV}\begin{pmatrix} 0 & 1 \\ 1 & 0 \end{pmatrix}, \tag{2.14}$$

for which we can choose

$$B = \sqrt{\frac{\kappa}{2dV}}\begin{pmatrix} i & 1 \\ -i & 1 \end{pmatrix}. \tag{2.15}$$

This particular choice of B allows us to replace the two real Gaussian noises $\xi_j(\boldsymbol{x},t)$ for each position $\boldsymbol{x}$, that would occur in the construction given in (2.13), with a single complex Gaussian noise $\Gamma(\boldsymbol{x},t) = (\xi_2 + i\xi_1)/\sqrt{2}$. It can be seen that for real noises with $\langle \xi_j(\boldsymbol{x},t)\xi_{j'}(\boldsymbol{x}',t')\rangle = \delta_{\boldsymbol{x},\boldsymbol{x}'}\delta_{j,j'}\delta(t-t')$, the correlators of the corresponding complex noises are $\langle \Gamma(\boldsymbol{x},t)\rangle = \langle \Gamma(\boldsymbol{x},t)\Gamma(\boldsymbol{x}',t')\rangle = 0$ and $\langle \Gamma^*(\boldsymbol{x},t)\Gamma(\boldsymbol{x}',t')\rangle = \delta_{\boldsymbol{x},\boldsymbol{x}'}\delta(t-t')$. The resulting stochastic equation for the lower polariton model, which I use in my simulations, is

$$\begin{aligned}\frac{\partial \Psi(\boldsymbol{x},t)}{\partial t} = &\left(-i\omega_{LP}(-i\boldsymbol{\nabla}) - ig\left(|\Psi(\boldsymbol{x},t)|^2 - \frac{1}{dV}\right) - \kappa\right)\Psi(\boldsymbol{x},t) \\ &- iF_p(\boldsymbol{x},t) + \sqrt{\frac{\kappa}{dV}}\Gamma(\boldsymbol{x},t)\,.\end{aligned} \tag{2.16}$$

Under what conditions is it valid to make the TWA? In the case of open systems such as polaritons, we can justify neglecting the third order terms, which arise from the interactions, by comparing them directly to the diffusion term, which arises from the dissipation. Comparing the coefficients of these terms in equation (2.11) gives a specific condition for determining the validity of the TWA for the two dimensional polariton system based on the physical parameters g and κ of the system and the discretisation of space dV. Namely, the TWA is valid if $\kappa \gg g/dV$ [18, 39, 73]. We can interpret this condition as stating that, when the TWA is valid, the quantum correlations generated by the third order terms are effectively washed out by the dissipation. More generally, the TWA has also been seen to break down if occupations become too small [3, 81], as is shown by the results in Fig. 1.3.

As an additional note, while I have focused on the perspective of phase space methods here, equation (2.16) is in fact a more general result that can also be reached using the Martin-Siggia-Rose formalism on the semiclassical limit of the Keldysh functional integral for the system (keeping only up to quadratic order in the "quantum fields") [82].

2.2 Positive-P representation of the driven-dissipative Bose-Hubbard model

While the TWA works well for systems in the semiclassical limit, where the correlations generated by the truncated terms can safely be neglected, for problems where quantum correlations are more important, such as may be relevant for some current and future experiments with polariton lattices, a different approach is required. An alternative phase space method that I consider for this purpose is the positive-P method. This section will give an overview of the positive-P method and its application to the driven-dissipative Bose-Hubbard model, which provides a description of polariton lattices and similar photonic platforms. Results from this method in my work will be given in chapter 5.

2.2.1 Mapping to the positive-P representation

In the example of equation (2.11), it can be seen that in the Wigner representation the diffusion terms arise from the dissipation, while interactions give rise to higher order derivative terms; for the P representation diffusion comes from the two-body interactions, and there are no higher order terms [68]. However, the diffusion matrix can end up not being positive definite, which precludes the conversion from the Fokker-Planck equation to stochastic differential equations for trajectories [65]. A way around this problem can be found through a generalisation of the P distribution by doubling the dimension of the phase space; the diffusion in the Fokker-Planck equation of the resulting distribution can always be made positive, and as such this so-called positive-P distribution is a genuine probability distribution which contains all the information about the quantum system without approximations [69].

While operator correspondences for the positive-P representation can be derived in a way more analogous to that outlined above for the Wigner representation [83], a helpful

alternative way to proceed is by considering the mapping from the density operator $\hat{\rho}$ to the positive-P distribution $P(\alpha,\beta)$ via the kernel operator $\hat{\Lambda}(\alpha,\beta)$. For a system with M bosonic modes we can define this as

$$\hat{\rho} = \int d^{2M}\boldsymbol{\alpha}\, d^{2M}\boldsymbol{\beta}\, P(\boldsymbol{\alpha},\boldsymbol{\beta})\hat{\Lambda}(\boldsymbol{\alpha},\boldsymbol{\beta}), \tag{2.17}$$

$$\hat{\Lambda}(\boldsymbol{\alpha},\boldsymbol{\beta}) = \bigotimes_j \hat{\Lambda}_j(\alpha_j,\beta_j), \quad \hat{\Lambda}_j(\alpha_j,\beta_j) = \frac{|\alpha_j\rangle\langle\beta_j^*|}{\langle\beta_j^*|\alpha_j\rangle},$$

with $|\alpha_j\rangle$, $|\beta_j^*\rangle$ being local coherent states for mode j and $\boldsymbol{\alpha}$, $\boldsymbol{\beta}$ representing the vector of all the α_j, β_j respectively [3, 70, 84]. We can find the relation between creation and annihilation operators and differential operators of the phase space variables acting on $\hat{\Lambda} \equiv \hat{\Lambda}(\boldsymbol{\alpha},\boldsymbol{\beta})$ using the properties of coherent states. Firstly, that the coherent states are eigenstates of the annihilation operators quickly gives us two of these relations:

$$\hat{a}_j\hat{\Lambda} = \alpha_j\hat{\Lambda}, \tag{2.18a}$$

$$\hat{\Lambda}\hat{a}_j^\dagger = \beta_j\hat{\Lambda}. \tag{2.18b}$$

To get the opposite relations, we can use (1.6) to rewrite the kernel for each mode as

$$\hat{\Lambda}_j = e^{-\alpha_j\beta_j} e^{\alpha_j\hat{a}_j^\dagger}|0\rangle\langle 0|e^{\beta_j\hat{a}_j}. \tag{2.19}$$

Taking derivatives of (2.19), we can see that

$$\frac{\partial}{\partial\alpha_j}\hat{\Lambda}_j = \hat{a}_j^\dagger\hat{\Lambda}_j - \beta_j\hat{\Lambda}_j,$$
$$\frac{\partial}{\partial\beta_j}\hat{\Lambda}_j = \hat{\Lambda}_j\hat{a}_j - \alpha_j\hat{\Lambda}_j,$$

which can be rearranged to get the remaining relations

$$\hat{\Lambda}\hat{a}_j = \left(\alpha_j + \frac{\partial}{\partial\beta_j}\right)\hat{\Lambda}, \tag{2.20a}$$

$$\hat{a}_j^\dagger\hat{\Lambda} = \left(\beta_j + \frac{\partial}{\partial\alpha_j}\right)\hat{\Lambda}. \tag{2.20b}$$

By using the definition (2.17) with the set of relations (2.18) and (2.20), and then integrating by parts, we will once again be able to convert the GKSL master equation into a Fokker-Planck equation for $P(\boldsymbol{\alpha},\boldsymbol{\beta})$.

From these relations, it can be also seen how quantum mechanical observables are calculated within the positive-P representation. Using the example of a single mode, without loss of generalisation, for any normally ordered operator $(\hat{a}^\dagger)^n\hat{a}^m$

$$\begin{aligned}\langle(\hat{a}^\dagger)^n\hat{a}^m\rangle = \mathrm{Tr}[\hat{\rho}(\hat{a}^\dagger)^n\hat{a}^m] &= \mathrm{Tr}[\hat{a}^m\hat{\rho}(\hat{a}^\dagger)^n] \\ &= \int d^2\alpha\, d^2\beta\, P(\alpha,\beta)\,\mathrm{Tr}[\hat{a}^m\hat{\Lambda}(\hat{a}^\dagger)^n] \\ &= \int d^2\alpha\, d^2\beta\, P(\alpha,\beta)\alpha^m\beta^n\,, \end{aligned} \tag{2.21}$$

where in practice the average of phase space variables over the probability distribution $P(\alpha,\beta)$ represented by the integral on the final line can instead be calculated by averaging the quantity $\alpha^m\beta^n$ over a large enough number of stochastic trajectories of α,β that sample $P(\alpha,\beta)$ [3, 65, 69, 70, 84].

2.2.2 Driven-dissipative Bose-Hubbard model

The physical system I will apply the positive-P method to is the driven-dissipative Bose-Hubbard (DDBH) model. This model describes a lattice of spatially localised bosonic modes with local interactions and Markovian dissipation on each lattice site, and hopping between sites, as shown in Fig. 1.2 (a,b). The state of such a system evolves according to the following GKSL master equation

$$\frac{\partial\hat{\rho}}{\partial t} = -\frac{i}{\hbar}\left[\hat{H}_{BH},\hat{\rho}\right] + \sum_j \frac{\gamma_j}{2}\left(2\hat{a}_j\hat{\rho}\hat{a}_j^\dagger - \hat{a}_j^\dagger\hat{a}_j\hat{\rho} - \hat{\rho}\hat{a}_j^\dagger\hat{a}_j\right), \tag{2.22}$$

with local dissipation rate γ_j. The Hamiltonian in the most general case of arbitrary hopping connections can be expressed in the frame of the coherent drive as

$$\begin{aligned}\frac{1}{\hbar}\hat{H}_{BH} = &\sum_j\left(-\Delta_j\hat{a}_j^\dagger\hat{a}_j + \frac{U_j}{2}\hat{a}_j^\dagger\hat{a}_j^\dagger\hat{a}_j\hat{a}_j + F_j\hat{a}_j^\dagger + F_j^*\hat{a}_j\right) \\ &- \sum_{connected\,j,j'}\left(J_{j,j'}\hat{a}_j^\dagger\hat{a}_{j'} + J_{j,j'}^*\hat{a}_{j'}^\dagger\hat{a}_j\right), \end{aligned} \tag{2.23}$$

where $\Delta_j = \omega_p - \omega_j$ is the detuning between the energy of the coherent drive ω_p and the local on-site energy ω_j, U_j is the strength of the local two-body interactions, F_j is the strength of the coherent drive, and $J_{j,j'}$ is the strength of hopping between sites j and j'. In (2.23), the hopping is defined such that the second sum counts each pairing j, j only once. Details of the derivation of the positive-P equations for this system will be given below, and can also be found in [3, 84].

2.2.3 Obtaining the Fokker-Planck equation

As mentioned in section 2.2.1, we can obtain a Fokker-Planck equation for the positive-P distribution $P(\boldsymbol{\alpha},\boldsymbol{\beta})$ by expanding (2.22) using the definition (2.17). Explicitly, this leads to

$$\int d^{2M}\boldsymbol{\alpha}\, d^{2M}\boldsymbol{\beta}\, \frac{\partial P(\boldsymbol{\alpha},\boldsymbol{\beta})}{\partial t}\hat{\Lambda} = \int d^{2M}\boldsymbol{\alpha}\, d^{2M}\boldsymbol{\beta}\, P(\boldsymbol{\alpha},\boldsymbol{\beta}) \left(-\frac{i}{\hbar}\left[\hat{H}_{BH},\hat{\Lambda}\right] + \sum_j \frac{\gamma_j}{2}\left[2\hat{a}_j\hat{\Lambda}\hat{a}_j^\dagger - \hat{a}_j^\dagger\hat{a}_j\hat{\Lambda} - \hat{\Lambda}\hat{a}_j^\dagger\hat{a}_j\right]\right). \tag{2.24}$$

As detailed in appendix B.1, using the relations (2.18) and (2.20) to convert the quantum operators acting on $\hat{\Lambda}$ to differential operators of the phase space variables, and then integrating by parts, assuming $P(\boldsymbol{\alpha},\boldsymbol{\beta})$ behaves such that we can neglect boundary terms, ultimately reduces this to the following Fokker-Planck equation for $P(\boldsymbol{\alpha},\boldsymbol{\beta})$:

$$\begin{aligned}\frac{\partial P(\boldsymbol{\alpha},\boldsymbol{\beta})}{\partial t} = \sum_j \Bigg\{ &\frac{\partial^2}{\partial\alpha_j^2}\left[-\frac{iU_j}{2}\alpha_j^2 P(\boldsymbol{\alpha},\boldsymbol{\beta})\right] + \frac{\partial^2}{\partial\beta_j^2}\left[\frac{iU_j}{2}\beta_j^2 P(\boldsymbol{\alpha},\boldsymbol{\beta})\right] \\ &- \frac{\partial}{\partial\alpha_j}\left[\left(i\Delta_j\alpha_j - iU_j\alpha_j^2\beta_j - iF_j - \frac{\gamma_j}{2}\alpha_j + i\sum_{j'\neq j} J_{j,j'}\alpha_{j'}\right)P(\boldsymbol{\alpha},\boldsymbol{\beta})\right] \\ &- \frac{\partial}{\partial\beta_j}\left[\left(-i\Delta_j\beta_j + iU_j\alpha_j\beta_j^2 - iF_j^* - \frac{\gamma_j}{2}\beta_j - i\sum_{j'\neq j} J_{j,j'}^*\beta_{j'}\right)P(\boldsymbol{\alpha},\boldsymbol{\beta})\right]\Bigg\}.\end{aligned} \tag{2.25}$$

In terms of the general construction (2.12), the (α_j,β_j) components of the drift vector given in (2.25) are

$$A_j = \begin{pmatrix} i\Delta_j\alpha_j - iU_j\alpha_j^2\beta_j - iF_j - \frac{\gamma_j}{2}\alpha_j + i\sum_{j'\neq j} J_{j,j'}\alpha_{j'} \\ -i\Delta_j\beta_j + iU_j\alpha_j\beta_j^2 - iF_j^* - \frac{\gamma_j}{2}\beta_j - i\sum_{j'\neq j} J_{j,j'}^*\beta_{j'} \end{pmatrix}, \tag{2.26}$$

while those of the diffusion matrix are

$$D_{j,j} = iU_j \begin{pmatrix} -\alpha_j^2 & 0 \\ 0 & \beta_j^2 \end{pmatrix}, \tag{2.27}$$

for which one possible decomposition of the form $D = BB^T$ is

$$B_{j,j} = \begin{pmatrix} \sqrt{-iU_j}\alpha_j & 0 \\ 0 & \sqrt{iU_j}\beta_j \end{pmatrix}. \tag{2.28}$$

Inputting these into the form given in (2.13), gives the (Ito) stochastic differential equations for trajectories of $(\boldsymbol{\alpha}, \boldsymbol{\beta})$ as [3, 84]

$$\frac{\partial \alpha_j}{\partial t} = i\Delta_j\alpha_j - iU_j\alpha_j^2\beta_j - iF_j - \frac{\gamma_j}{2}\alpha_j + i\sum_{j'\neq j} J_{j,j'}\alpha_{j'} + \sqrt{-iU_j}\alpha_j\xi_j^{(\alpha)}, \tag{2.29a}$$

$$\frac{\partial \beta_j}{\partial t} = -i\Delta_j\beta_j + iU_j\alpha_j\beta_j^2 - iF_j^* - \frac{\gamma_j}{2}\beta_j - i\sum_{j'\neq j} J_{j,j'}^*\beta_{j'} + \sqrt{iU_j}\beta_j\xi_j^{(\beta)}, \tag{2.29b}$$

where $\xi_j^{(z)}$ are uncorrelated real Gaussian noises with $\langle \xi_j^{(z)}(t)\xi_{j'}^{(z')}(t')\rangle = \delta_{z,z'}\delta_{j,j'}\delta(t-t')$ and $\langle \xi_j^{(z)}(t)\rangle = 0$.

2.2.4 The Stratonovich correction

Practically, there is in fact one final step separating the equations (2.29) from those which I solve numerically. The stochastic differential equations, such as (2.29), which are produced from the Fokker-Planck equation, are given in terms of Ito stochastic calculus, where each step $t \to t + dt$ of the evolution is calculated using the noise at the previous time t, and not all the rules of deterministic calculus are valid. As such, the only correct method to numerically integrate these Ito stochastic differential equations directly is the simple Euler algorithm, which calculates the evolution after each small time step Δt as

$$v_j(t+\Delta t) \approx v_j(t) + \frac{\partial v_j(t)}{\partial t}\Delta t\,.$$

More sophisticated numerical integration algorithms that I use for my simulations instead calculate the Stratonovich integral, as they take advantage of the rules of deterministic

calculus remaining true for the Stratonovich stochastic calculus [80, 84–86]. A small correction to (2.29) is therefore needed to convert the stochastic differential equations from Ito to Stratonovich form, such that the Stratonovich integral my simulations calculate are in fact the trajectories that sample $P(\boldsymbol{\alpha},\boldsymbol{\beta})$.

In terms of the general form (2.13), converting from the Ito form to the Stratonovich form of this stochastic differential equation results in an alteration to the drift term by [80, 84]

$$A_j \to A_j - \frac{1}{2}\sum_{k,l} B_{k,l}\frac{\partial B_{j,l}}{\partial v_k}. \tag{2.30}$$

As an aside, it can be seen from this form that for the truncated Wigner method there was no Stratonovich correction, and both forms of the stochastic differential equations would be identical, as the B matrix chosen in section 2.1.3 did not depend on the phase space variables. Calculating this correction for B given by (2.28) gives, for the (α_j,β_j) components,

$$-\frac{1}{2}\left[\left(\sqrt{-iU_j}\alpha_j\tfrac{\partial}{\partial\alpha_j},\quad \sqrt{iU_j}\beta_j\tfrac{\partial}{\partial\beta_j}\right)\begin{pmatrix}\sqrt{-iU_j}\alpha_j & 0\\ 0 & \sqrt{iU_j}\beta_j\end{pmatrix}\right]^T = -\frac{iU}{2}\begin{pmatrix}-\alpha_j\\ \beta_j\end{pmatrix}, \tag{2.31}$$

which finally results in the Stratonovich form of the Ito stochastic differential equations (2.29) as

$$\frac{\partial\alpha_j}{\partial t} = i\Delta_j\alpha_j - iU_j\alpha_j^2\beta_j + \frac{iU}{2}\alpha_j - iF_j - \frac{\gamma_j}{2}\alpha_j + i\sum_{j'\neq j}J_{j,j'}\alpha_{j'} + \sqrt{-iU_j}\alpha_j\xi_j^{(\alpha)}, \tag{2.32a}$$

$$\frac{\partial\beta_j}{\partial t} = -i\Delta_j\beta_j + iU_j\alpha_j\beta_j^2 - \frac{iU}{2}\beta_j - iF_j^* - \frac{\gamma_j}{2}\beta_j - i\sum_{j'\neq j}J_{j,j'}^*\beta_{j'} + \sqrt{iU_j}\beta_j\xi_j^{(\beta)}. \tag{2.32b}$$

It is these equations that occur directly in the code that implements my numerical simulations using the positive-P method.

Chapter 3

Momentum structures in the polariton optical parametric oscillator

This chapter concerns the first of two projects using the truncated Wigner method for the lower polariton model, outlined in section 2.1. The work that is detailed in this chapter encompasses all my contributions to the results presented in [1]. While the object of study in this chapter is only the momentum distributions $|\Psi(\boldsymbol{k},t)|^2$, we will see that the truncated Wigner results still exhibit interesting behaviour that is not seen at the mean field level.

3.1 Outline of problem and research questions

The aim of this project was to look into how the momentum distributions that occur in the polariton OPO regime vary with the strength of the coherent drive. Typically, analytical studies of polariton OPO rely on a three-mode description, considering only the signal, pump and idler modes [20, 25, 44, 87–90]. While much progress can be made in this way, this approach has a number of shortcomings in fully capturing the behaviour of the real polariton OPO system. Firstly, more complicated structures, such as satellite states occupied by further scattering of polaritons out of the signal and idler modes [88, 91–94], will tend to occur to some degree. Secondly, even in the cases where the three-mode description is a good approximation, it lacks sufficient constraints to uniquely determine the momentum of the signal mode, which must be chosen as if it were an external parameter when using the three-mode model, despite not being a controlled parameter in both actual and numerical experiments. Specifically, solving for the steady state of the

three-mode mean field solution gives a set of three complex equations, providing six constraints, for determining seven variables: the amplitudes of the three modes, two of their phases (the model is invariant under changes in the relative phase between the signal and idler modes), and the energy and momentum of the signal mode; this leaves one of these variables, usually chosen to be the signal momentum, unconstrained [1, 88–90]. Solving the three-mode model therefore does not predict which signal momentum the actual system chooses.

In our work in [1], Kirsty Dunnet provided two possible options for estimating the correct signal momentum analytically, based on linear stability analysis [20, 87, 88, 90, 95–97] of pump-only and three-mode OPO solutions of the mean field Gross-Pitaevskii equation

$$\frac{\partial\Psi(\boldsymbol{x},t)}{\partial t} = \left(-i\omega_{LP}(-i\boldsymbol{\nabla}) - ig|\Psi(\boldsymbol{x},t)|^2 - \kappa\right)\Psi(\boldsymbol{x},t) - iF_p(\boldsymbol{x},t)\,. \tag{3.1}$$

The first estimate is that, since OPO occurs when the solution with only the pump mode occupied becomes unstable towards the occupation of modes at other momenta, the signal momentum is the momentum for which this instability is largest. Specifically, the pump-only solution $\Psi(\boldsymbol{x},t) = Pe^{-i\omega_p t + i\boldsymbol{k}_p\cdot\boldsymbol{x}}$ is unstable to fluctuations of the form

$$\Psi(\boldsymbol{x},t) = Pe^{-i\omega_p t + i\boldsymbol{k}_p\cdot\boldsymbol{x}} + \Delta P e^{-i(\omega_p+\omega)t + i(\boldsymbol{k}_p+\boldsymbol{\Delta}k)\cdot\boldsymbol{x}}\,, \tag{3.2}$$

when one of the eigenvalues ω of the linear response matrix, which results from substituting (3.2) into (3.1) and keeping only up to linear terms in ΔP, has a positive imaginary part, suggesting that the fluctuations grow rather than decay with time [1, 20, 87, 88, 90, 95–97]. We then identified this first estimate for the signal momentum as k_s^m, the momentum at which the imaginary part of that eigenvalue is maximum for each f_p [1]. The second estimate is that the signal momentum is chosen within the range of values for which the three-mode solution

$$\Psi(\boldsymbol{x},t) = Se^{-i\omega_s t + i\boldsymbol{k}_s\cdot\boldsymbol{x}} + Pe^{-i\omega_p t + i\boldsymbol{k}_p\cdot\boldsymbol{x}} + Ie^{-i\omega_i t + i\boldsymbol{k}_i\cdot\boldsymbol{x}}\,, \tag{3.3}$$

with $2\omega_p = \omega_s + \omega_i$ and $2\boldsymbol{k}_p = \boldsymbol{k}_s + \boldsymbol{k}_i$ is stable against the occupation of further satellite states. That is, when similarly considering the linear response matrix for fluctuations around this three-mode mean field solution [1, 88–90], none of the eigenvalues have a positive imaginary part. To determine if and under what conditions these estimates are useful, I performed numerical experiments using the truncated Wigner method, which can model the full structure of the OPO that occurs without the limitations of the analytical model.

As such, this project aimed to answer the following questions using truncated Wigner simulation of the polariton OPO:

- How does the structure of OPO change when varying the strength of the external drive between the OPO thresholds?
- At what values of the strength of the external drive is the three-mode description of polariton OPO a good approximation?
- How well do the proposed analytical estimates predict the correct value of the signal momentum in these cases?
- What occurs in the actual system at pump strengths for which the three-mode description has no stable solutions?

3.2 Technical details of simulations

Truncated Wigner simulations are carried out by numerically integrating equation (2.16), repeating for many different realisations of the noise, with physical observables being calculated in post-processing by averaging appropriate products of the phase space variables over the realisations. Numerical integration is performed using the XMDS2 package [85]. The XMDS script for this purpose was originally written by Galbadrakh Dagvadorj, and has since been edited by Alejandro Zamora and myself. I process the output of this using MATLAB. In the simulations considered in this chapter and in chapter 4, I use units defined in terms of the system parameters. Specifically, energies are measured in units of $\hbar\Omega_R/2$, time in units of $2/\Omega_R$ and lengths in units of $\sqrt{\hbar/(m_C\Omega_R)}$. The simulations for the project discussed in this chapter use an $N \times N = 256 \times 256$ point grid representing a

system size of $L \times L = 211.08772 \times 211.08772$. In preliminary tests, I used a system size of $L \times L = 256 \times 256$, but the system size was reduced in order to reduce dV and thereby increase the momentum range. For convenience, the simulations use periodic boundary conditions, but this needs to be taken into account when interpreting the results as it can produce effects near the edges that are unphysical for an actual flat microcavity. The time step size for the numerical integration is 10^{-2} time units.

A number of simplifications go into the lower polariton model used in the simulations, as described by equation (2.8). Firstly, since the exciton mass m_X is orders of magnitude larger than the cavity photon mass m_C, the exciton dispersion is treated as being flat, $\omega_X = \omega_X(0)$. Additionally I consider the case, and set the zero of energy such that, $\omega_X(0) = \omega_C(0) = 0$. This leads to the lower polariton dispersion taking the form (in the units defined above) $\omega_{LP}(\boldsymbol{k}) = \frac{1}{2}\left(k^2 - \sqrt{k^4+4}\right)$. Further, I neglect the momentum dependence of the polariton-polariton interactions that is inherited from the Hopfield coefficients; this approximation is valid provided that the resulting broadening of the interaction potential in space is insignificant on the scale of the discretisation of space in the simulation. This can be estimated by looking at the Fourier transform of the Hopfield coefficient $X(\boldsymbol{k})$, which I find falls to $\sim 2\%$ of its maximum value over the distance $\sqrt{dV}$ between points in the simulation, suggesting the momentum dependent interactions would still be well localised on this scale. Mean field simulations and the linear stability analysis without this approximation (using the full exciton-photon model) show a slight rescaling of the OPO thresholds, but otherwise display qualitatively similar behaviour, including equivalent values of k_s^m [1]. Finally, I consider the lower polariton dissipation rate κ to also be momentum independent; this is true exactly in the case $\kappa_X = \kappa_C = \kappa$, assuming that the dissipation rates of the excitons and photons, $\kappa_{X,C}$ respectively, are momentum independent themselves, since $\kappa = |X(\boldsymbol{k})|^2\kappa_X + |C(\boldsymbol{k})|^2\kappa_C$ and $|X(\boldsymbol{k})|^2 + |C(\boldsymbol{k})|^2 = 1$ [17, 18].

For the projects discussed in both this chapter and chapter 4, I use the same physical parameters $\hbar\Omega_R = 4.4\text{meV}$ and $m_C = 2.3 \times 10^{-5} m_e$, with m_e the electron mass. This results in the units defined above taking values of $2/\Omega_R \approx 0.3\text{ps}$ for time, and $\sqrt{\hbar/(m_C\Omega_R)} \approx 0.87\mu\text{m}$ for lengths. I use $\kappa = 0.045$ (corresponding to $\hbar\kappa \approx 0.1\text{meV}$)

and $g = 0.00118$. This set of physical parameters is chosen to match typical experiments in this field [32]. For these values, $dV \approx 0.68$ and $g/\kappa \approx 0.026$, and so the TWA is expected to hold quite well. I choose the pump to have $k_p = 1.3989905$, directed entirely along the x direction, where this precise value is used to ensure that k_p lies on the discrete momentum grid, and for its frequency to be on resonance with the lower polariton dispersion, $\omega_p = \omega_{LP}(\boldsymbol{k}_p)$. Having the pump frequency on resonance with the lower polariton dispersion places us in the optical limiter regime (i.e. where the pump mode is monostable), which has usually been considered in recent studies pertaining to order and superfluidity in the polariton OPO regime [32, 39, 44, 98], and conversely avoids the alternative situation where the pump mode is bistable, which occurs for $\omega_p - \omega_{LP}(\boldsymbol{k}_p) > \sqrt{3}\kappa$, and can result in different physics [20, 87, 88, 94, 95, 97, 99–102]. The pump strength $\tilde{f}_p$ is varied. Note also that for f_p values quoted below, the actual pump strength is $\tilde{f}_p = f_p/\sqrt{g}$; this was done for ease of comparison with certain theoretical models that rescale the fields so as to eliminate g, such as are used in the corresponding analytical work in [1].

3.3 Dependence of OPO behaviour on pump strength

As mentioned above, for this project I have run a series of numerical simulations of the polariton OPO using the truncated Wigner method, to investigate how the structure of OPO in momentum space varies with the strength of the external drive. I simulate for a range of pump powers between the lower threshold, at $f_p = 0.0135$, and the upper threshold, at $f_p = 0.0535$. The simulations are run until a steady state is reached, up to fluctuations from the noise, for the total occupation $\sum_{\boldsymbol{k}} |\Psi(\boldsymbol{k},t)|^2$, as well as for the form of $|\Psi(\boldsymbol{k},t)|^2$. The amount of time taken to achieve this can vary significantly depending on f_p, but for almost all cases running to $t = 160000$ (i.e. 48ns) is sufficient. To optimise the time taken to reach the steady state, I use numerical solutions of the steady state of the mean field Gross-Pitaevskii equation (3.1) as the initial conditions for the truncated Wigner simulations at the corresponding f_p. While technically this initial condition does not represent a physical Wigner distribution, the steady state should be independent of the initial conditions and this choice allows it to be obtained comparatively quickly [39]. For each case, I analysed where the maxima occur in the steady state momentum distribution

$|\Psi(\boldsymbol{k})|^2$, as well as the relative order of magnitude of these maxima. A minimum of 10 realisations were used for each f_p; while this would be insufficient for accurately calculating more noise dependent physical quantities, such as the correlation functions explored in later chapters, it is enough to confirm if the momenta, up to the resolution of the discrete momentum grid, and order of magnitude of the maxima in $|\Psi(\boldsymbol{k})|^2$ are not changing between realisations. In most cases, the values of $|\Psi(\boldsymbol{k})|^2$ at the maxima are so much larger than the contribution from the noise that, even when calculated from single realisations, the variation between them is only $\sim 1\%$. For f_p where this was not the case, as well as for all those I show in Fig. 3.2, an average over 100 realisations was used instead.

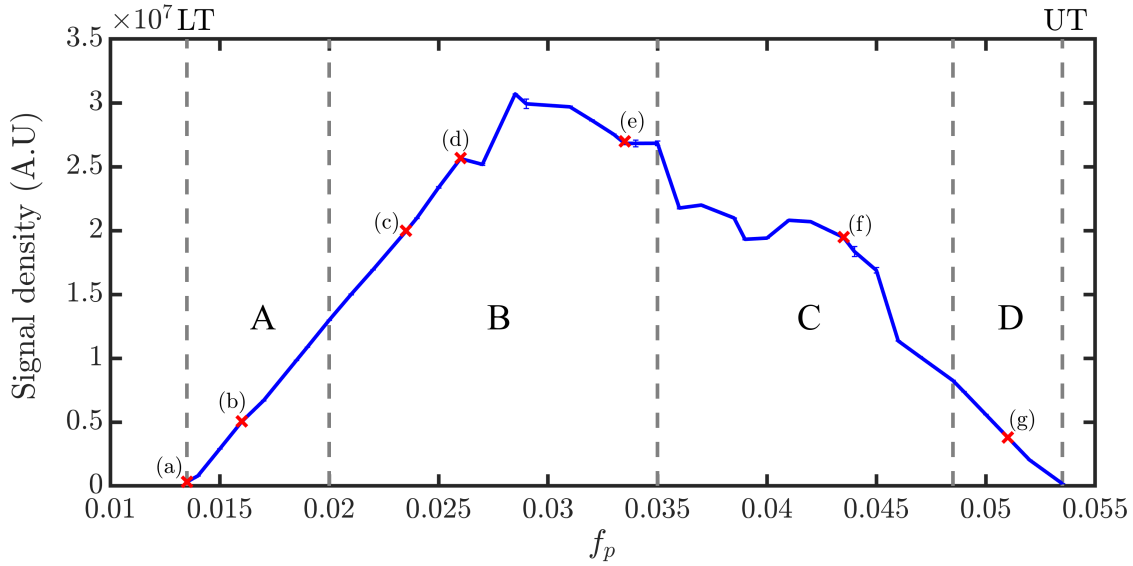

Figure 3.1: Density of signal across the OPO regime, showing upper (UT) and lower (LT) thresholds as well as the four main regions of different behaviours: rings (A), small satellites (B), large satellites (C), three-mode (D). Red crosses labelled (a)-(g) mark the examples shown in Fig. 3.2.

Fig. 3.1 shows the variation in the signal density with f_p. This 'signal density' is obtained by $\sum_{\boldsymbol{k}} |\Psi(\boldsymbol{k})|^2$ for all $\boldsymbol{k}$ within a rectangular filter

$$\frac{3\tilde{k}_s - k_p}{2} \leq k_x \leq \frac{\tilde{k}_s + k_p}{2}, \quad \frac{\tilde{k}_s - k_p}{2} \leq k_y \leq \frac{k_p - \tilde{k}_s}{2},$$

with $\tilde{k}_s = 0.1$. The OPO thresholds, which bound the range of f_p that I run simulations for, are predicted by the linear stability analysis as the minimum and maximum values

of f_p for which the pump mode is unstable towards the formation of OPO [1], and are confirmed by the signal densities in Fig. 3.1.

I identify that observed behaviour of $|\Psi(\boldsymbol{k})|^2$ can be broadly classified into four regions in f_p, that I have labelled A-D in Fig. 3.1. Examples of the various behaviours that occur are shown in Fig. 3.2, labelled (a)-(g). I will explain here how these examples demonstrate the four broad categories A-D. The simplest behaviour occurs in region D, near the upper threshold. Here the three-mode description, with distinct pump, signal and idler modes, holds well since all other features in $|\Psi(\boldsymbol{k})|^2$ beyond these main three maxima are negligible. An example of this is given in Fig. 3.2 (g).

One way in which the three-mode description can break down is due to the appearance of additional modes, known as satellite states, that can become occupied due to secondary scattering channels that involve the signal and/or idler polaritons [25, 91]. In region B, satellites become visible in $|\Psi(\boldsymbol{k})|^2$ on a logarithmic scale, but are at least an order of magnitude smaller than the main signal/idler, so the three-mode ansatz should still be a good approximation. The exact layout of these features in momentum space can vary significantly in this region, as shown by the various examples of it given by Fig. 3.2 (c)-(e). In contrast to this, in region C the occupation of the satellites becomes comparable to that of the primary signal/idler modes, and a three-mode description is no longer appropriate. One example of this is given by Fig. 3.2 (f).

Near the lower threshold, in region A, the three-mode description breaks down in a different way. Instead of a single mode, the signal and idler each consist of many maxima arranged around a ring in momentum space. This can be seen in Fig. 3.2 (b). While for the other examples, I usually found that the full momentum structure could already be seen in each single realisation, for this example at $f_p = 0.016$, only a subset of the full set of peaks around the ring would occur in each realisation, and averaging over many realisations was required to produce the full set of peaks and their relative magnitudes. On the lower threshold, the occupation around these rings is almost completely uniform, as shown in Fig. 3.2 (a).

It should be noted once again that the truncated Wigner simulations observe behaviour in these momentum distributions that cannot be seen at the level of the mean

field Gross-Pitaevskii equations. In particular, the mean field solution is entirely confined along the line $k_y = 0$; the fluctuations included by the truncated Wigner are required to observe the rich structure of broadening and scattering to modes with $k_y \neq 0$ shown in the various examples of Fig. 3.2 [1].

3.3.1 Comparison to analytical estimates of the signal momentum

A summary of the simulation results for all values of f_p considered is given in Fig. 3.3, which I also use to compare my results to the linear response analysis, and the estimates of the signal momentum derived from it. Firstly, one can see in these results the four broad categories of behaviours that I mark A-D in Fig. 3.1. Note, however, that the boundaries between these regions are not sharply defined, and for cases near the boundaries the observed momentum distributions will typically either vary smoothly between the two neighbouring classes of behaviour or alternate between them at different values of f_p.

Now, comparing to the linear response estimates, I will begin by looking at region D, where the three-mode description best approximates the actual behaviour. It can be seen in Fig. 3.3 that this region corresponds closely to a region of the phase diagram, near the upper OPO threshold, where the three-mode solution is stable. Furthermore, the momentum of the signal across this region corresponds closely to the value of k_s^m here; in fact the value of the signal peak is the closest value to k_s^m allowed by the discretisation of momentum in the numerical simulations.

While it fails to give as good predictions of the signal momentum in other cases where the three-mode approximation is valid, the estimate k_s^m is also useful in another situation: in region A, especially when very close to the lower OPO threshold, the values of k_s^m shown in Fig. 3.3, which are actually just the cross-section at $k_y = 0$ of a full ring of k_s^m values in the full two dimensional momentum space [1], correctly predict the diameter of the rings seen in the momentum distributions from the truncated Wigner simulations. We can therefore see that overall, the estimate k_s^m provides a good prediction of the behaviour close to the OPO threshold, where logically the instability of the pump mode plays the strongest role in the formation of the OPO state, but fails deeper within the OPO regime, where secondary scattering channels likely play a more important role.

For much of region B, the signal momentum loosely follows the shape of the corre-

sponding area of the phase diagram where the three-mode solution is stable. However, for many cases in this region the satellite states can become quite significant, so the stability of the three-mode solution is not a perfect predictor of the momentum of the main signal peak. Finally, the linear response analysis for the three-mode solution successfully predicts the presence of region C, where the three-mode approximation is not valid, as this corresponds to a large range of f_p for which the three-mode solution is not stable for any value of k_s.

3.4 Summary

To conclude this chapter, I am now in a position to provide definitive answers to the set of research questions set out in section 3.1.

- How does the structure of OPO change when varying the strength of the external drive between the OPO thresholds?

I have discovered that the behaviours that occur as the pump strength is varied across the OPO regime can be classified into four main categories. In increasing order of the pump strengths that they occur at, these are: A, where the maxima of the signal mode are distributed around a ring in momentum space; B, where satellite states occur but are at least an order of magnitude smaller than the signal mode; C, where satellite states become comparable in magnitude to the primary signal mode, and finally D, where any features beyond the main three modes are negligible.

- At what values of the strength of the external drive is the three-mode description of polariton OPO a good approximation?

The three-mode description is most valid in region D near the upper OPO threshold. It can also generally be a good approximation for the behaviour seen in region B, since although significant satellite states do occur there, they are small in occupation compared to the main signal and idler modes.

- How well do the proposed analytical estimates predict the correct value of the signal momentum in these cases?

While the two estimates generated by the linear response analysis are far from perfect predictions of the actual behaviours of the polariton OPO, they do provide some useful insight. Specifically, the presence or lack of stable three-mode solutions at a given f_p seems to successfully indicate the ranges of f_p where the three-mode approximation is valid (regions B, D), or breaks down (region C), respectively. The corresponding regions of stable three-mode solutions give an accurate, if rather imprecise, indication of the signal momentum chosen in region D, and can perhaps be considered to give a very crude approximation for the behaviour of the signal momenta across region B. Meanwhile, the estimate from the largest instability of the pump-only solution k_s^m accurately indicates which modes become occupied by the primary scattering channel for values of f_p near the upper and lower OPO thresholds, but loses its usefulness for predicting the behaviour of the more complicated forms of OPO that occur for intermediate pump strengths.

- What occurs in the actual system at pump strengths for which the three-mode description has no stable solutions?

As mentioned, the extent of region C, in which the three-mode description breaks down due to the presence of large satellite states, is correctly predicted by a corresponding lack of stable three-mode solutions across that range of pump strengths.

Overall, the understanding of the properties of the polariton OPO regime developed in this chapter will be useful going forward for any comparisons between the three-mode analytical model and actual or numerical experiments. This will become immediately apparent in the next chapter, where this knowledge will be used to help understand the relation and discrepancies between my numerical results and the predictions from the mapping of the three-mode model of OPO to the Kardar-Parisi-Zhang equation.

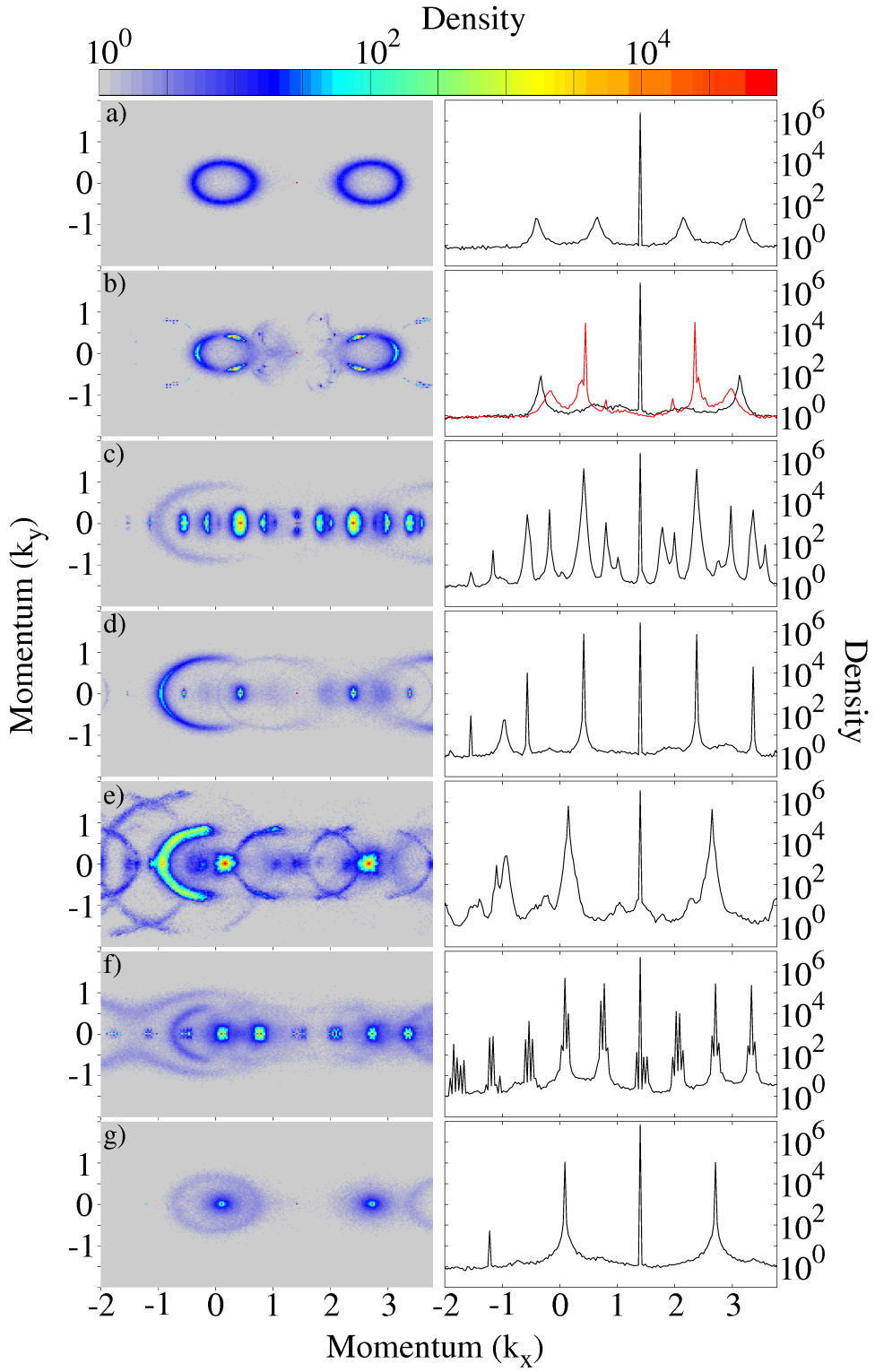

Figure 3.2: Momentum distributions $|\Psi(\boldsymbol{k})|^2$ on logarithmic scale for a) $f_p = 0.0135$, b) $f_p = 0.016$, c) $f_p = 0.0235$, d) $f_p = 0.026$, e) $f_p = 0.0335$, f) $f_p = 0.0435$, and g) $f_p = 0.051$. Left panels show $|\Psi(\boldsymbol{k})|^2$ in two dimensional $\boldsymbol{k}$-space while right panels show cut through $k_y = 0$, red line in right panel of b) shows a cut through $k_y = 0.327$. The colourmap for $|\Psi(\boldsymbol{k})|^2$ in left panels has been truncated to between 10^0 and 10^5 to increase visibility of the most significant maxima. Error bars have been omitted as they are negligible near the peaks.

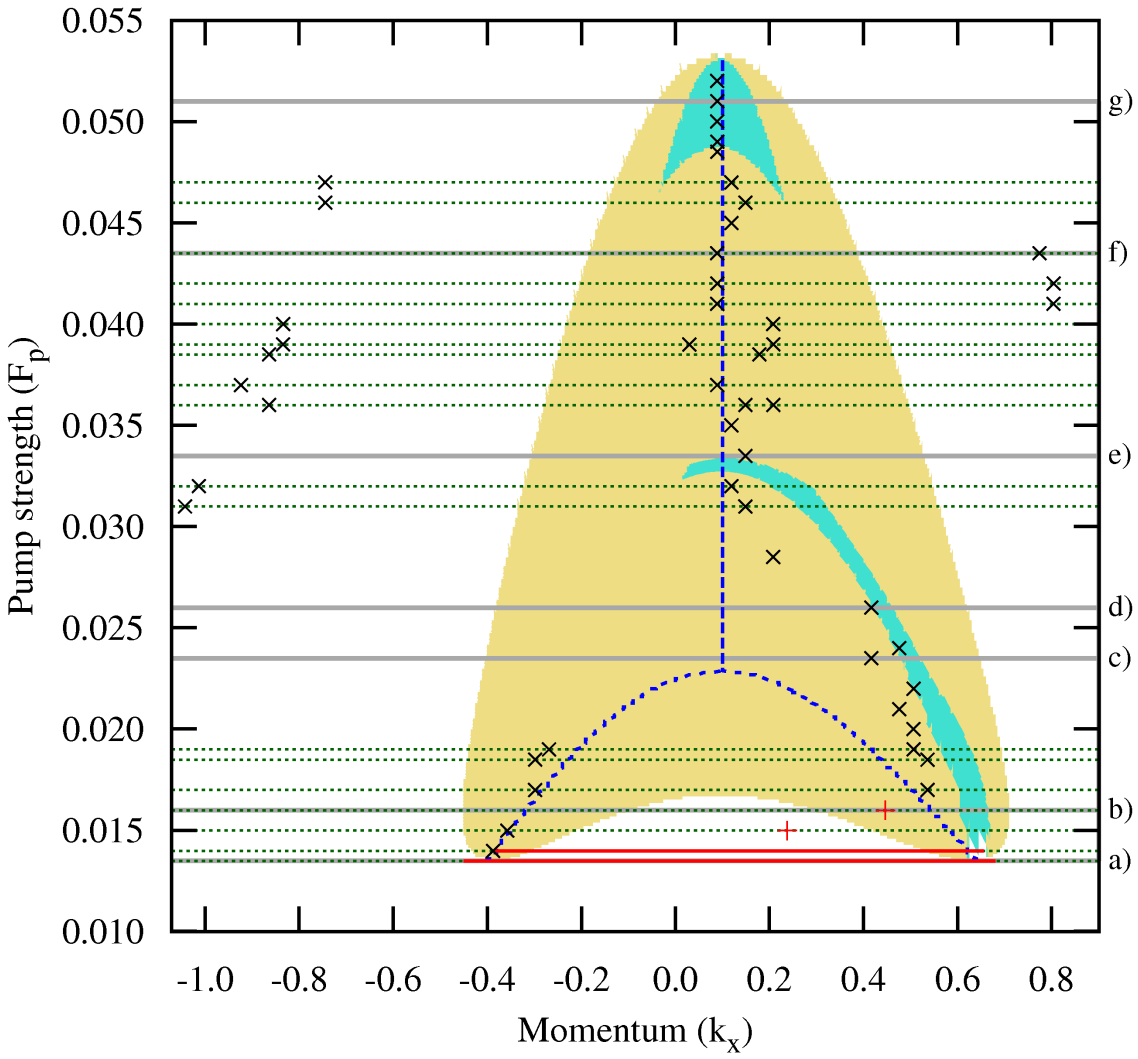

Figure 3.3: Summary of OPO behaviours with varying f_p, superimposed on linear stability diagram by Kirsty Dunnet. Data from truncated Wigner simulations: black crosses ($\times$) show largest magnitude peaks with $k_y = 0$, while red crosses (+) are instead used when peaks have $k_y \neq 0$; multiple crosses are shown at the same f_p if these peaks are within the same order of magnitude, and such cases are marked with a horizontal green dashed line for clarity; red lines near the lower OPO threshold indicate the diameter of rings of roughly uniform occupation; grey horizontal lines labelled (a)-(g) indicate the examples shown in Fig. 3.2. Linear response data by Kirsty Dunnet: shaded regions indicate where the pump mode only solution with pump strength f_p is unstable to linear fluctuations with momentum $(k_x, 0)$, cyan shaded regions show where the three-mode OPO solution with signal momentum $(k_x, 0)$ is stable to linear fluctuations to occupy further modes, while yellow shaded regions indicate where both the pump-only and three-mode solutions are unstable; the blue dashed line indicates the momentum k_s^m for which maxima occur in imaginary part of one eigenvalue of the linear response matrix for fluctuations around the pump-only solution.

Chapter 4

Observing the signatures of the Kardar-Parisi-Zhang universality in the polariton optical parametric oscillator

This chapter will outline the background and results of my efforts to observe predicted signatures of the relation between the OPO regime of microcavity polaritons and the Kardar-Parisi-Zhang (KPZ) universality, by performing numerical simulations using the truncated Wigner method. The relation between polartion OPO and KPZ was first outlined in [44]. Following on from that work, I began work to show that the behaviours predicted analytically therein can be observed in full multimode stochastic simulations of the polariton OPO system using the truncated Wigner method. The results of this work can be found in preprint at [2], and will be discussed in detail in this chapter.

4.1 The Kardar-Parisi-Zhang universality

Universality classes group systems, which may have very different microscopic physics, by their common behaviour at long length and time scales. Originally proposed as a model for the height of stochastically growing interfaces [103], the KPZ equation provides a universality class that is unique to non-equilibrium systems. The KPZ universality class encompasses a large number of such systems, including cell colonies [104, 105], burning paper [106–108], liquid crystal turbulence [109–111], and has recently also been shown to describe the phase fluctuations of the polariton field, both in the incoherently pumped [43]

and OPO [44] regimes. In the two dimensional and anisotropic case [44, 112, 113], the KPZ equation takes the form

$$\frac{\partial\theta}{\partial t} = D_x\frac{\partial^2\theta}{\partial x^2} + D_y\frac{\partial^2\theta}{\partial y^2} + \frac{\lambda_x}{2}\left(\frac{\partial\theta}{\partial x}\right)^2 + \frac{\lambda_y}{2}\left(\frac{\partial\theta}{\partial y}\right)^2 + \xi\,, \tag{4.1}$$

where $\xi(\boldsymbol{r},t)$ is Gaussian noise with $\langle\xi(\boldsymbol{r},t)\xi(\boldsymbol{r}',t')\rangle = 2\Delta\delta(\boldsymbol{r}-\boldsymbol{r}')\delta(t-t')$ and $\langle\xi(\boldsymbol{r},t)\rangle = 0$. When the phase fluctuations follow this equation, then this results in the spatial correlations of the polariton field taking a 'stretched exponential' form in the steady state; that is

$$\langle\hat{\Psi}^\dagger(\boldsymbol{R}+\boldsymbol{r})\hat{\Psi}(\boldsymbol{R})\rangle \sim \exp[-\tilde{r}^{2\chi}]\,, \tag{4.2}$$

where $\tilde{r} = \sqrt{(x/x_0)^2 + (y/y_0)^2}$ factors in the anisotropy of the system and χ is a universal exponent [44]. The roughness exponent χ for the KPZ class in two dimensions is not known analytically, but recent numerical studies tend to agree on a value of $\chi \approx 0.39$ [114–116].

When the KPZ equation describes a compact variable such as a phase, an additional complication arises from the possibility of vortices. In thermal equilibrium, which can be represented by setting $\lambda_x = \lambda_y = 0$ in equation (4.1), vortices and antivortices attract each other, resulting in the BKT transition to a quasi-ordered state with bound vortices at low enough temperature. However, when the phase obeys the KPZ equation, the interaction between vortices is altered, such that at large distances the vortices and antivortices repel each other, meaning that a sufficiently large system at sufficiently long times should always reach a disordered state with free vortices [78, 79].

The discrepancy between the observed algebraic order in experiments and simulations of polaritons [37–39] and the behaviour predicted by the KPZ equation arises due to the finite size of the microcavity. If the nonlinear coefficients $\lambda_{x,y}$ in equation (4.1) are small compared to the diffusion coefficients $D_{x,y}$, then the length scales for both the observability of the stretched exponential decay of correlations and for the unbinding of vortices become extremely large [43, 44, 78, 79]. While for most choices of parameters typical of current polariton experiments, the resulting coefficients of the KPZ equation are such that these length scales are much larger than the system size, there exists some

range of pump powers within the OPO regime for which the nonlinear coefficients $\lambda_{x,y}$ become large and the effects of KPZ physics should become observable [44].

4.2 Numerical techniques for exploring KPZ

In this chapter, I aim to investigate that prediction of [44] using truncated Wigner simulations. To do this I compare the behaviours of two observables for results with f_p inside and outside the window where the signatures of KPZ are predicted to become visible: if the KPZ scaling behaviour without vortices appears within that window of pump strengths, then it can be seen by looking at the first order spatial correlations of the signal mode, while if the vortex unbinding phase of [78, 79] occurs, it will also be visible in the average number of vortices in the signal mode. In this section, I will go over the technical details of my simulations for this project, and in particular how these observables are obtained from the truncated Wigner results.

As stated there, most of the details of the numerical simulations and their computational implementation for this chapter, including the values of physical parameters, are as given in section 3.2. The one exception is that the main results of this chapter are obtained using a larger system size: except where otherwise stated, the grid is $N \times N = 512 \times 512$ points representing an area of $L \times L = 422.17544 \times 422.17544$. This gives the same value of dV as stated in section 3.2, but the system is doubled in length.

4.2.1 Isolating the signal mode

Since the KPZ equation in the context of polariton OPO concerns the free phase between the signal and idler modes, any evidence of KPZ visible in the truncated Wigner simulations will be found by studying the behaviour of only the signal mode [44]. The first step in my analysis is therefore to isolate the signal mode from the full multimode stochastic complex number field $\Psi(\boldsymbol{k},t)$ output by the numerical integration of (2.16). I do this by first identifying the signal momentum k_s as the largest maximum in the momentum distribution in the region with $k_x < k_p$, and then isolating this signal mode by using a square filter around it in momentum space, including only $\Psi(\boldsymbol{k},t)$ with $\boldsymbol{k}$ within the range

$$\frac{3k_s - k_p}{2} \leq k_x \leq \frac{k_s + k_p}{2}, \quad \frac{k_s - k_p}{2} \leq k_y \leq \frac{k_p - k_s}{2}, \tag{4.3}$$

assuming that this signal peak occurs along $k_y = 0$, at $\boldsymbol{k} = (k_s, 0)$.

For quantities that can be calculated in momentum space, it is enough to simply only include momenta within the filter defined by (4.3). When the field in real space instead needs to be considered, I can define a filtered signal field in real space $\Psi_s(\boldsymbol{x},t)$ using the Fourier transforms (2.9). Specifically,

$$\Psi_s(\boldsymbol{x},t) = \frac{1}{N\sqrt{dV}} \sum_{\boldsymbol{k}\in\text{filter}} e^{-i\boldsymbol{k}\cdot\boldsymbol{x}}\Psi(\boldsymbol{k},t)\,, \tag{4.4}$$

where the momentum sum is over momenta within the ranges (4.3).

4.2.2 Calculating correlations in truncated Wigner

The primary object of study in this chapter will be the first order spatial correlations of the signal mode. The difference between the slow algebraic decay of these correlations in the quasi-ordered BKT phase, usually shown to occur in the polariton OPO regime [39], and the stretched exponential or exponential decay of correlations predicted for the KPZ scaling or vortex dominated phases respectively, will provide the clearest indication of the signatures of the underlying KPZ universality becoming visible within the predicted range of pump strengths. Here I will outline how this correlation function is defined and how I calculate it from the output of the truncated Wigner simulations.

In terms of operators, the normalised first order spatial correlation is defined as

$$g^{(1)}(\boldsymbol{r}) = \frac{\langle\hat{\Psi}^\dagger(\boldsymbol{R}+\boldsymbol{r})\hat{\Psi}(\boldsymbol{R})\rangle}{\sqrt{\langle\hat{\Psi}^\dagger(\boldsymbol{R}+\boldsymbol{r})\hat{\Psi}(\boldsymbol{R}+\boldsymbol{r})\rangle\langle\hat{\Psi}^\dagger(\boldsymbol{R})\hat{\Psi}(\boldsymbol{R})\rangle}}\,. \tag{4.5}$$

Converting this to the Wigner representation leads to a definition of the first order spatial correlations of the signal mode $g_s^{(1)}(\boldsymbol{r})$ in terms of the momentum filtered signal field $\Psi_s(\boldsymbol{x},t)$,

$$g_s^{(1)}(\boldsymbol{r}) = \frac{\langle\Psi_s^*(\boldsymbol{R}+\boldsymbol{r},t)\Psi_s(\boldsymbol{R},t)\rangle_{\boldsymbol{R}} - \frac{\delta_{\boldsymbol{r},\boldsymbol{0}}}{2dV}}{\langle\Psi_s^*(\boldsymbol{R},t)\Psi_s(\boldsymbol{R},t)\rangle_{\boldsymbol{R}} - \frac{1}{2dV}}\,, \tag{4.6}$$

where $\langle\ldots\rangle_{\boldsymbol{R}}$ represents averaging over stochastic realisations and over the auxiliary position $\boldsymbol{R}$. However, in practice $g_s^{(1)}(\boldsymbol{r})$ can be efficiently calculated in momentum space. Expanding (4.6) using the Fourier transform (4.4) leads to an equation that I use to

calculate $g_s^{(1)}(\boldsymbol{r})$ from the stochastic complex number fields $\Psi(\boldsymbol{k},t)$ in momentum space,

$$g_s^{(1)}(\boldsymbol{r}) = \frac{\langle \Psi^*(\boldsymbol{k},t)\Psi(\boldsymbol{k},t)e^{i\boldsymbol{k}\cdot\boldsymbol{r}}\rangle_{\boldsymbol{k}\in\text{filter}} - \frac{\delta_{\boldsymbol{r},\boldsymbol{0}}}{2}}{\langle \Psi^*(\boldsymbol{k},t)\Psi(\boldsymbol{k},t)\rangle_{\boldsymbol{k}\in\text{filter}} - \frac{1}{2}}, \tag{4.7}$$

where $\langle ... \rangle_{\boldsymbol{k}\in\text{filter}}$ represents averaging over stochastic realisations and over momenta $\boldsymbol{k}$ within the square filter around $(k_s, 0)$ defined by (4.3). Where appropriate, I also average over multiple separate time samples within the steady state. Error bars are calculated from the standard deviation of time samples being averaged over, treating them as approximately independent measurements.

4.2.3 Finding and counting vortices

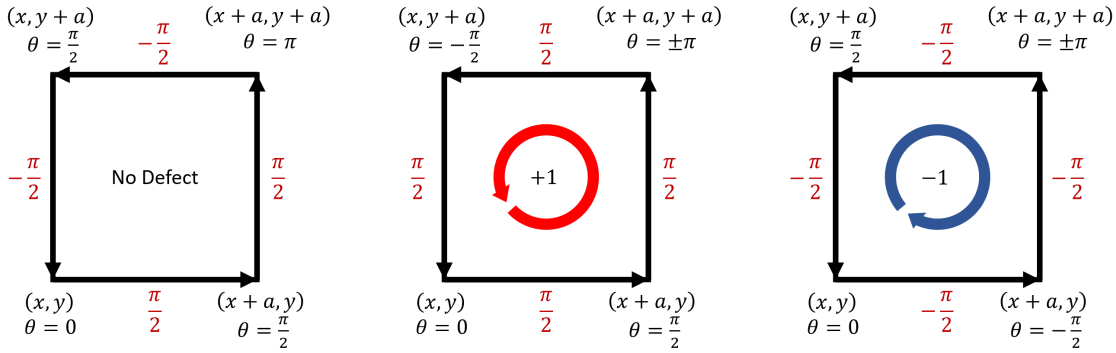

Figure 4.1: Diagram demonstrating the operation of the vortex finding algorithm. Examples of phase differences around a unit square in spatial grid for no defect $m = 0$ (left), a vortex $m = +1$ (center), and an antivortex $m = -1$ (right). Corners are labelled with their coordinates and example local values of θ, while the sides are labed with the phase difference $\Delta\theta$ along the direction of the arrows.

A second important observable, especially for distinguishing between the KPZ scaling and vortex dominated phases, is the average number of vortices in the signal field $\Psi_s(\boldsymbol{x},t)$. To determine this, I implement an algorithm that locates the position $\boldsymbol{x}$ of the vortices in $\Psi_s(\boldsymbol{x},t)$. Vortices are topological defects around which the phase θ of the field circulates by $2\pi m$, where the winding number m is a non-zero integer, typically $m = \pm 1$. Since in the simulation results, space is discretised on a grid with some spacing a, the algorithm determines whether there is no vortex $m = 0$, a vortex $m = +1$, or an antivortex $m = -1$, associated with each point $\boldsymbol{x} = (x,y)$ in the grid, by finding the total change in phase when taking the closed path around a unit square (i.e. of side length a) in the grid

$(x,y) \to (x+a,y) \to (x+a,y+a) \to (x,y+a) \to (x,y)$, and dividing by 2π. A diagram visualising this process for $m = 0, \pm 1$ is given in Fig. 4.1. In order to make sure vortices are correctly identified, the compactness of the phase variable $-\pi \leq \theta < \pi$ needs to be taken into account by making sure the change in θ between any two points is also kept within the interval $-\pi \leq \Delta\theta < \pi$. In practice, this is done by defining the change in θ between two points (x_1, y_1) and (x_2, y_2) as

$$\Delta\theta(x_1,y_1;x_2,y_2) = (\theta(x_2,y_2) - \theta(x_1,y_1) + \pi) \,\mathrm{mod} 2\pi - \pi\,, \tag{4.8}$$

from which I then obtain the locations of all the vortices and antivortices as effectively a spatial field of the winding number $m(\boldsymbol{x})$, for each stochastic realisation, given by

$$\begin{aligned} m(\boldsymbol{x}) = \frac{1}{2\pi} [&\Delta\theta(x,y;x+a,y) + \Delta\theta(x+a,y;x+a,y+a) \\ &+\Delta\theta(x+a,y+a;x,y+a) + \Delta\theta(x,y+a;x,y)]\,. \end{aligned} \tag{4.9}$$

The vortex winding number field $m(\boldsymbol{x})$ could have many potential applications for studying the behaviour and properties of vortices within the system. The simplest is the average number of vortices and antivortices within the system, which can be calculated as

$$n_{v+av} = \langle \sum_{\boldsymbol{x}} |m(\boldsymbol{x})| \rangle\,, \tag{4.10}$$

with $\langle ... \rangle$ representing averaging over stochastic realisations.

4.3 Finding the drive strength for observing KPZ

The first step in attempting to find evidence of KPZ physics, is to find an appropriate value of f_p that the analytical predictions tell us should show the signatures of KPZ at all length scales. The determining factor is the quantity $g_{KPZ} = (\lambda_x^2 \Delta)/(D_x^2 \sqrt{D_x D_y})$, which is derived from the coefficients of the KPZ equation (4.1). For cases with $g_{KPZ} \geq 1$, the length scale for seeing these signatures, which depends exponentially on $1/g_{KPZ}$ [43, 44], becomes small enough to be within the realistic sizes of actual microcavities.

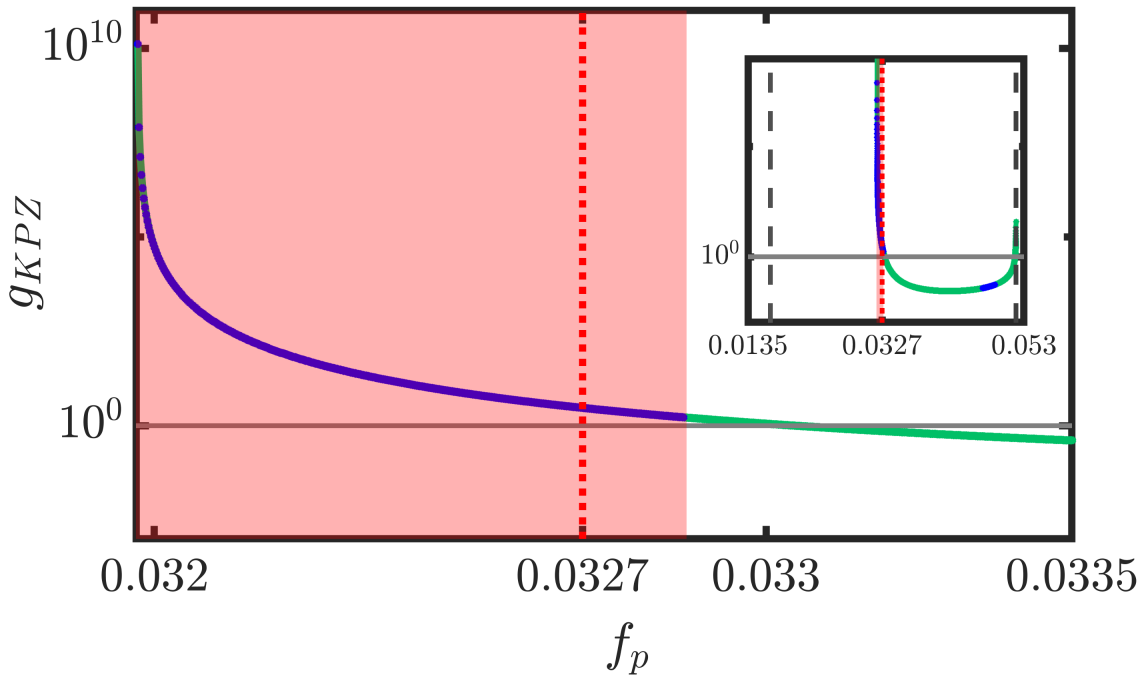

Figure 4.2: KPZ nonlinearity g_{KPZ} as a function of the pump strength f_p, generated from codes by Alejandro Zamora. The blue line shows where the three-mode ansatz, assumed in deriving the KPZ equation for OPO, is stable. The window where stretched exponential decay is expected to be visible at all length scales is given by $g_{KPZ} \geq 1$ (horizontal line marks $g_{KPZ} = 1$). The red shaded region shows where both three-mode OPO is stable and $g_{KPZ} \geq 1$. The dotted vertical red line marks $f_p = 0.0327$. Parameters are $k_p = 1.4$, $k_s = 0.2084$, $\gamma = 0.045$, $\hbar\Omega_R = 4.4$meV, as in numerical simulations (k_s is chosen to match that seen in the numerics at $f_p = 0.0327$). Inset shows the full range of f_p where OPO occurs, with the dashed vertical lines marking the OPO thresholds for this value of k_s.

For [44], Alejandro Zamora produced MATLAB codes to convert from the three-mode analytical model of polariton OPO to the corresponding coefficients of the KPZ equation (4.1). We use those again for this project to calculate the dependence of g_{KPZ} on f_p for the parameters used in my simulations. An example of this for the same parameters, using a signal momentum of $k_s = 0.1$, is given in [44], but as established in our previous work [1], which was the subject of chapter 3, the exact value of k_s chosen by the system cannot be determined with certainty from the three-mode analytical model, and instead needs to be provided to it from the numerics. As such, I progressed by using that example as a guide to suggest values of f_p which might be in the window for $g_{KPZ} \geq 1$, checking what actual value of k_s occurs for that f_p by running a small number of realisations of my stochastic simulations, and then recalculating g_{KPZ} as a function of f_p for that value

of k_s, to check that the value of f_p chosen does actually give $g_{KPZ} \geq 1$ when the correct value of k_s for it is used in the three-mode analytical model. For $f_p = 0.0327$, a value of $k_s = 0.2084$ was found to occur in my simulations. A plot of g_{KPZ} as a function of f_p for $k_s = 0.2084$ is shown in Fig. 4.2, indicating that $f_p = 0.0327$ does indeed give $g_{KPZ} \geq 1$ and so is a suitable example for searching for the KPZ behaviour.

To contrast with the results for $f_p = 0.0327$, I chose two other values of f_p outside of the window of $g_{KPZ} \geq 1$ to run simulations for, $f_p = 0.026$ and $f_p = 0.051$. These were chosen to provide one example of both larger and smaller f_p than the KPZ case $f_p = 0.0327$, and such that in all three cases the three-mode description holds to good approximation, in the sense that satellite modes are at least an order of magnitude smaller than the main signal peak, as I define in chapter 3. Values of the coefficients of the KPZ equation and g_{KPZ} for each of these f_p, calculated using their respective values of k_s, are given in table 4.1. Note that $f_p = 0.026$ actually also gives a large value of g_{KPZ}, but that the KPZ equation is not stable there due to negative values of D_x and D_y.

f_p	D_x	D_y	λ_x	λ_y	Δ	g_{KPZ}
0.051	0.5827	0.6751	-0.5430	-0.4805	0.0394	0.0546
0.0327	0.0337	0.0469	-0.5247	-0.4683	6.4509×10^{-4}	2.9717
0.026	-0.0068	-0.0111	-0.4466	-0.4284	9.3462×10^{-4}	464*

Table 4.1: Analytically calculated values of the coefficients of the KPZ equation, and the quantity g_{KPZ} derived from them, generated from codes by Alejandro Zamora, for example values of f_p used in my numerical simulations, at their respective values of k_s.

4.4 Signatures of KPZ in spatial correlations

This section concerns the main results of this chapter: the first order spatial correlations of the signal mode seen in the window of f_p where KPZ is analytically predicted to become observable. I will start by comparing the behaviour of these correlations between the three example values of f_p chosen in the previous section, before looking at how the correlations for $f_p = 0.0327$, within the window, fit to various functional forms, including the stretched exponential decay predicted for the KPZ scaling phase.

4.4.1 Contrasting correlations at different drive strengths

As a preliminary investigation into whether the signatures of the KPZ universality become visible within the predicted window in f_p, I compare the behaviour of the first order spatial correlations of the signal $g_s^{(1)}(\boldsymbol{r})$ found in my truncated Wigner simulations at $f_p = 0.0327$, within the window, to those at $f_p = 0.026$ and $f_p = 0.051$. In all cases, simulations are run starting from a mean field steady state initial condition until a time $t = 160000$, by which point a steady state, up to noise fluctuations, has been reached for the correlations $g_s^{(1)}(\boldsymbol{r})$. A total of 100 realisations are used for $f_p = 0.026$ and $f_p = 0.051$, while 400 realisations are used for the main result at $f_p = 0.0327$. I separately calculate the correlations along two perpendicular directions, purely along the x direction, $g_s^{(1)}(x, y = 0)$, and purely along the y direction, $g_s^{(1)}(x = 0, y)$, where, to reiterate, x is the direction parallel to the pump momentum. All results are generated using additional averaging over time samples within the steady state between $t = 120000$ and $t = 160000$.

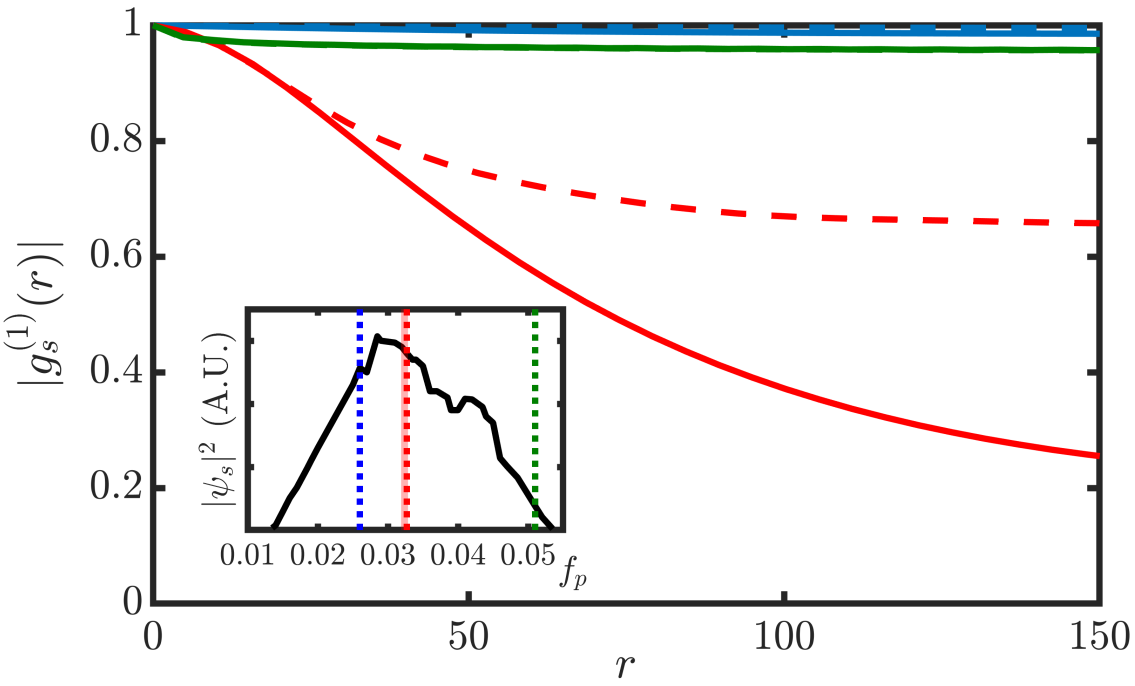

Figure 4.3: Comparison of $g_s^{(1)}(\boldsymbol{r})$ at different pump strengths $f_p = 0.026$ (blue), $f_p = 0.0327$ (red), and $f_p = 0.051$ (green), for $\boldsymbol{r}$ taken along the x (dashed lines) or y (solid lines) directions. Inset: Signal density versus pump strength f_p, reproduced from Fig. 3.1, with vertical dotted lines indicating the chosen f_p examples.

The comparison between these correlations can be seen in Fig. 4.3. There it can be seen that the decay of correlations for $f_p = 0.0327$ are dramatically faster than those outside the KPZ window, which are almost flat in comparison. Typically, within the OPO thresholds the correlations $g_s^{(1)}(\boldsymbol{r})$ decay algebraically [39], with the exponents of this decay becoming smaller for higher signal density states far from the OPO thresholds, hence the almost flat correlations for $f_p = 0.026$ and $f_p = 0.051$. That I observe a much faster decay of correlations for an even higher signal density state at $f_p = 0.0327$ gives a strong indication that signs of KPZ are being seen here, as the stretched exponential decay of correlations would be much faster than the slow algebraic decay that would be expected this far from the threshold without the influence of KPZ.

Not explained by the mapping of the polariton OPO to KPZ, is the strong anisotropy in the correlations that can be seen for $f_p = 0.0327$. The correlations decay significantly more slowly in the x direction than in the y direction. I discuss possible reasons for this further in section 4.4.3.

4.4.2 Fitting the form of spatial correlations

Now to further confirm if it is the stretched exponential decay of correlations of the KPZ scaling phase that is being seen at $f_p = 0.0327$, I fit those results for $g_s^{(1)}(\boldsymbol{r})$ to various functional forms. In this section, I will focus on the correlations perpendicular to the pump momentum $g_s^{(1)}(x = 0, y)$, which it turns out fit well to the stretched exponential decay. The comparatively strange behaviour of $g_s^{(1)}(x, y = 0)$ will be later discussed in section 4.4.3.

I fit the correlations to three different functional forms: algebraic decay

$$g_s^{(1)}(x = 0, y) = \left(\frac{y}{y_{0,\mathrm{alg}}} \right)^{-\alpha_y}, \tag{4.11}$$

with fitting parameters $y_{0,\mathrm{alg}}$ and α_y, exponential decay

$$g_s^{(1)}(x = 0, y) = A \exp\left[-\frac{y}{y_{0,\mathrm{exp}}} \right], \tag{4.12}$$

with fitting parameters A and $y_{0,\mathrm{exp}}$, and stretched exponential decay

$$g_s^{(1)}(x=0,y) = B\exp\left[-\left(\frac{y}{y_{0,\mathrm{strexp}}}\right)^{2\chi}\right], \tag{4.13}$$

with fitting parameters B and $y_{0,\mathrm{strexp}}$, and χ fixed at the expected value $\chi = 0.39$ for 2D KPZ. In principle, a fit could also be performed with free χ, but it is helpful for comparisons that all the fitting models have the same number of free parameters. The quality of these fits are compared using the coefficient of determination R^2. Fits are performed for points in the range $30 < y < 120$, for reasons that will be justified below.

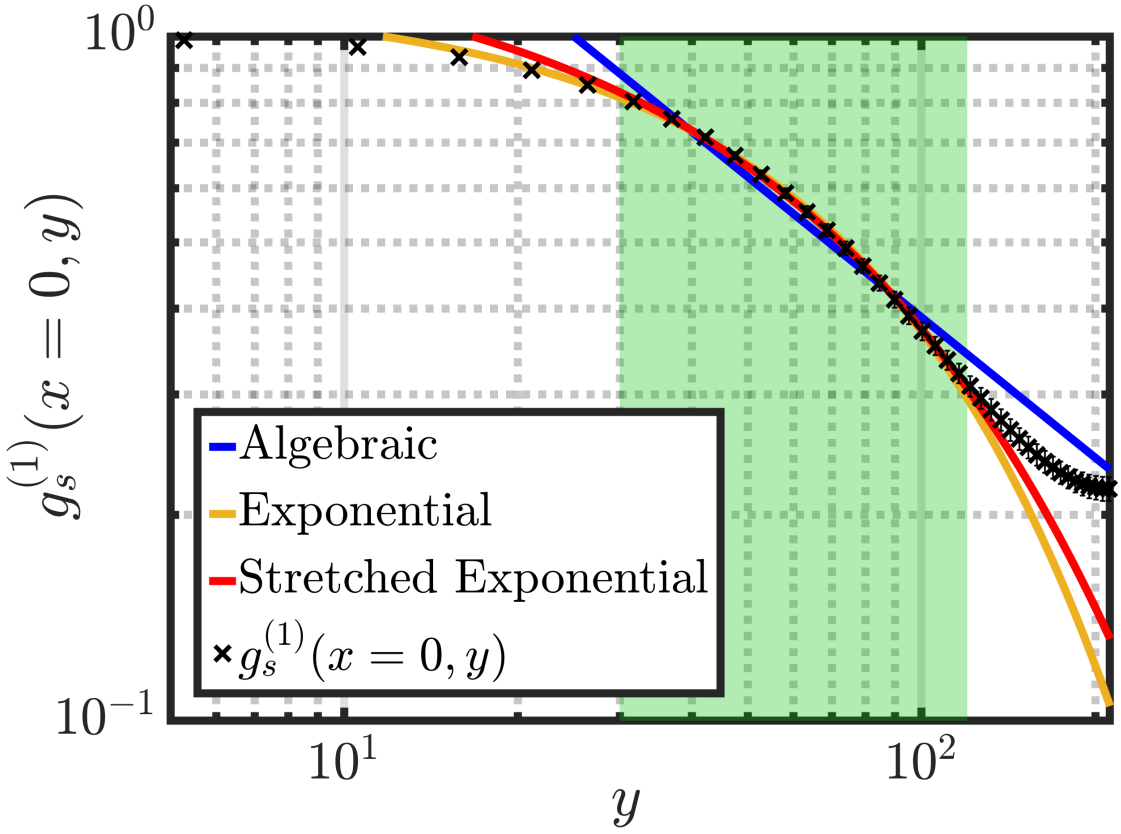

Figure 4.4: $g_s^{(1)}(x=0,y)$ with fits to algebraic (blue), exponential (yellow), and stretched exponential (red) decay. The green shaded region indicates the points included in the fit.

A comparison of the fits in this range for these three models is shown in Fig. 4.4. The respective values of R^2 are $R^2 = 0.9995$ for stretched exponential decay, $R^2 = 0.9986$ for the pure exponential decay, and $R^2 = 0.9784$ for algebraic decay. Stretched exponential decay provides the best fit, although it can be difficult to distinguish it from the pure

exponential decay due to their very similar functional forms, hence the similar values of R^2. To distinguish between the stretched exponential and pure exponential decay, I instead look at the vortices in the signal mode. Physically, the stretched exponential decay of correlations is associated with the KPZ scaling phase without vortices, while the pure exponential decay would be caused instead by the vortex dominated phase. In these simulations, I start from initial conditions without vortices and do not see any vortices appear in the signal mode at any point during the evolution. This suggests that the form of the correlations I observe cannot be an exponential decay due to vortices, and is consequently consistent with a stretched exponential decay resulting from the appearance of the KPZ scaling phase.

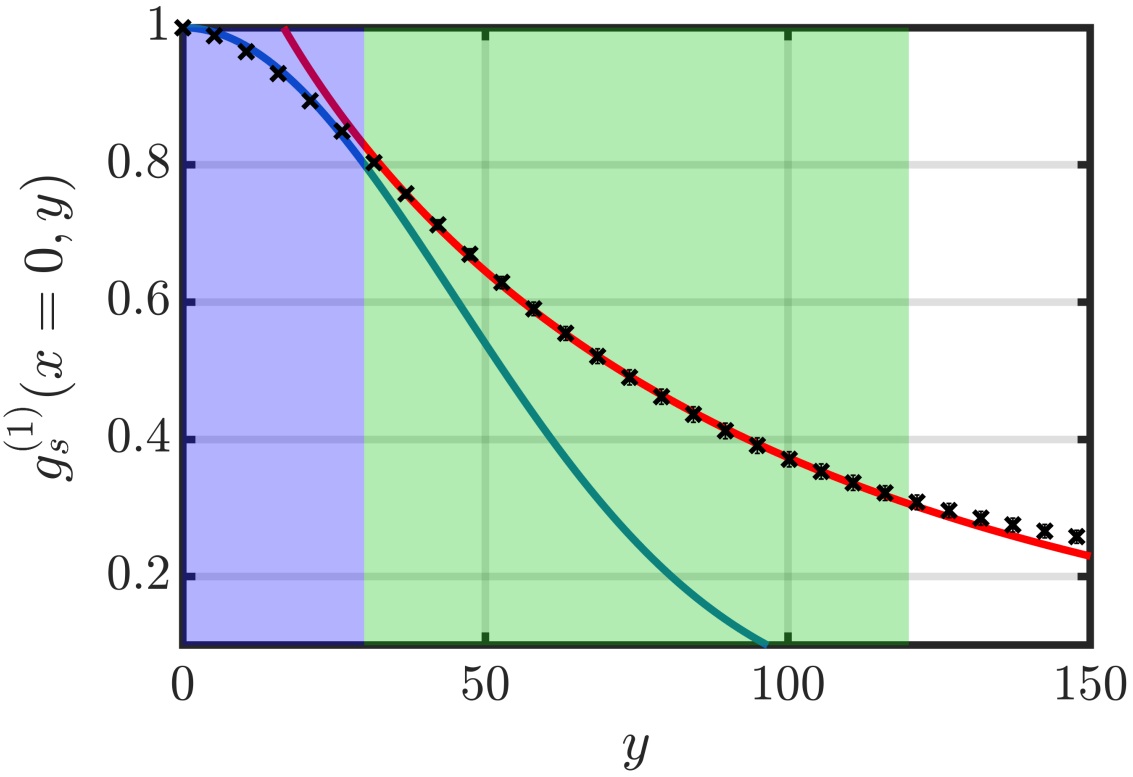

Figure 4.5: $g_s^{(1)}(x=0,y)$ showing fits to Gaussian form (blue line) of short range correlations at $y<30$ (blue shaded region) and the fit to stretched exponential decay with $\chi=0.39$ (red line) in the (green shaded) region $30<y<120$.

In order to perform these fits, certain portions of the correlation function at the smallest and largest distances need to be excluded, as indicated by the green region in Fig. 4.4. For small distances, this is due to short range form of correlations being expectedly dif-

ferent to the behaviours I am looking for, which are predicted in the "long range limit". I determine an appropriate lower fitting bound by performing a Gaussian fit to the short range form of correlations, as shown in Fig. 4.5. Points at large distances need to instead be excluded due to the finite size of the system; specifically, the periodic boundary conditions enhance the value of $g_s^{(1)}(\boldsymbol{r})$ near the edges. It is more difficult to choose rigorously the value for the upper fitting bound, however, I show in Fig. 4.6 that the value of R^2 for the stretched exponential decay does not depend strongly on it until around $y = 140$, beyond which it starts to rapidly decline. This seemingly means that any value of the upper fitting bound less than $y = 140$ is sufficient to remove most of the boundary effects, and can be chosen without strongly affecting the results; as such, I choose an upper fitting bound of $y = 120$, which maximises R^2 of the stretched exponential decay.

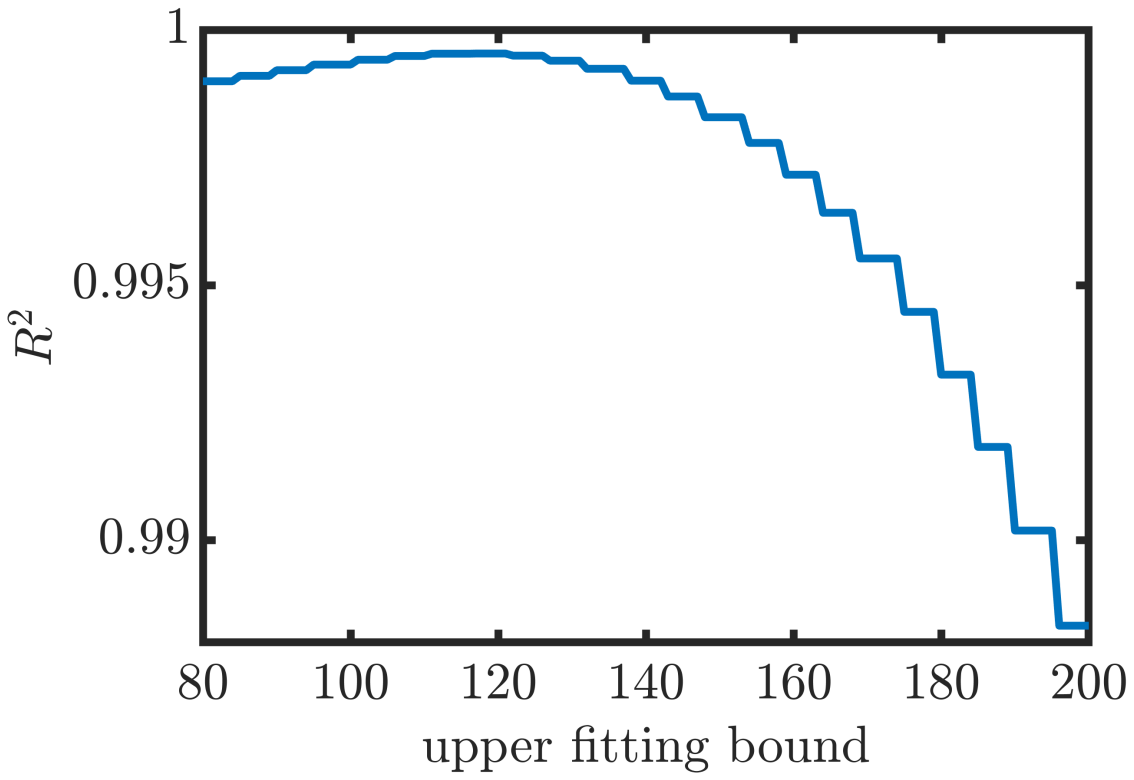

Figure 4.6: Coefficient of determination R^2 for stretched exponential fit as a function of the chosen upper fitting bound. The lower fitting bound is fixed as $y > 30$.

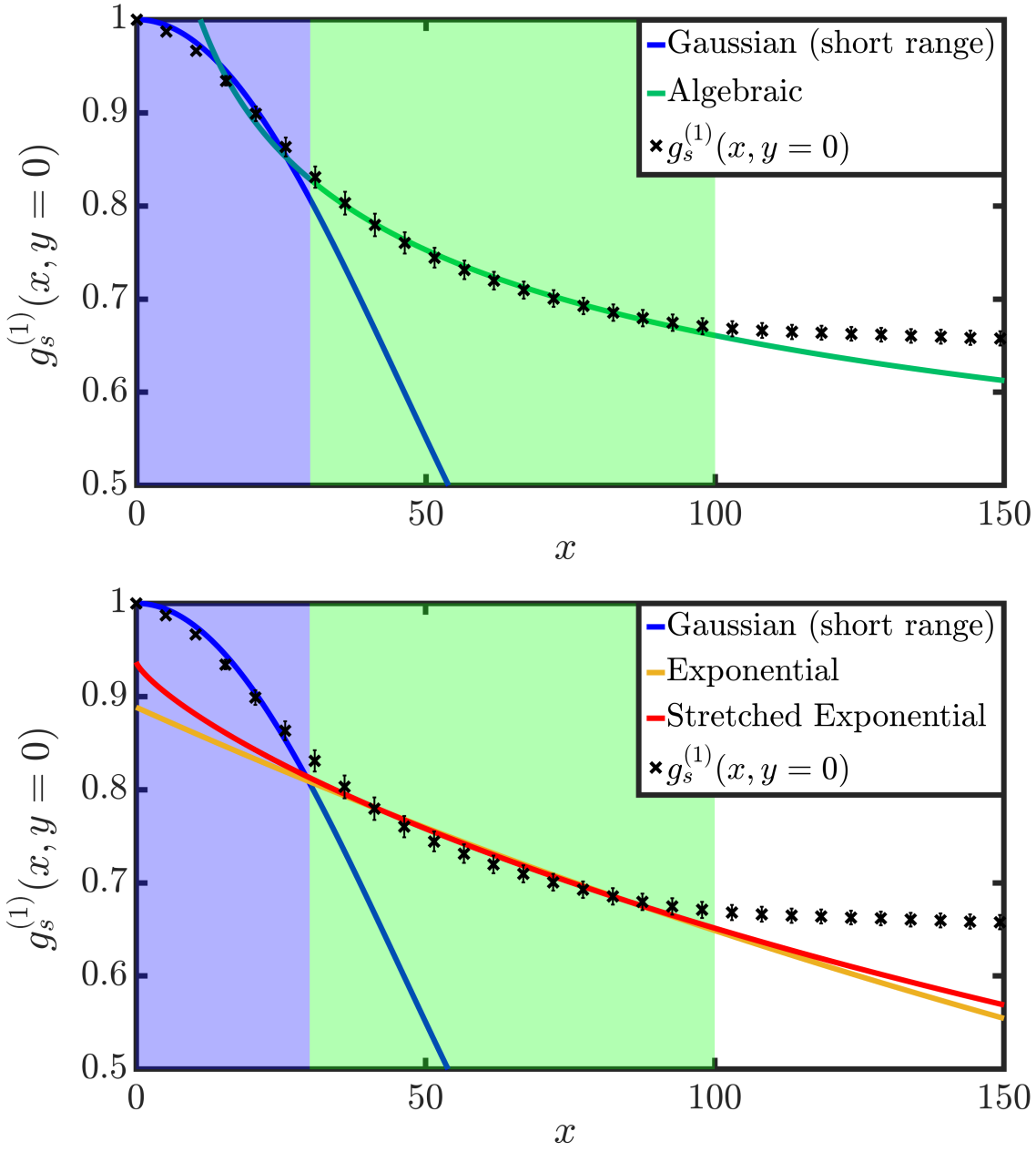

Figure 4.7: $g_s^{(1)}(x, y = 0)$ with fits to algebraic (green line, top panel), exponential (yellow, bottom panel), and stretched exponential (red, bottom panel) decay. The green shaded region indicates the points included in the fit. The blue line shows a Gaussian fit to short range correlations within the blue region, used to determine the lower fitting bound, as in Fig. 4.5.

4.4.3 Anisotropy of correlations

While the correlations in the y direction fit very well to the stretched exponential form predicted by the KPZ equation, this is not the case for $g_s^{(1)}(x, y = 0)$. I show the fits of

$g_s^{(1)}(x, y = 0)$ to each of the three fitting models in Fig. 4.7. Due to the faster saturation of $g_s^{(1)}(x, y = 0)$ at large x, I use a shorter fitting range $30 < x < 100$. The best fit of the points in this range is the algebraic decay with $R^2 = 0.9938$; exponential and stretched exponential fits give $R^2 = 0.9448$ and $R^2 = 0.9592$ respectively. In all cases, these are notably weaker than the fit of stretched exponential decay in the y direction.

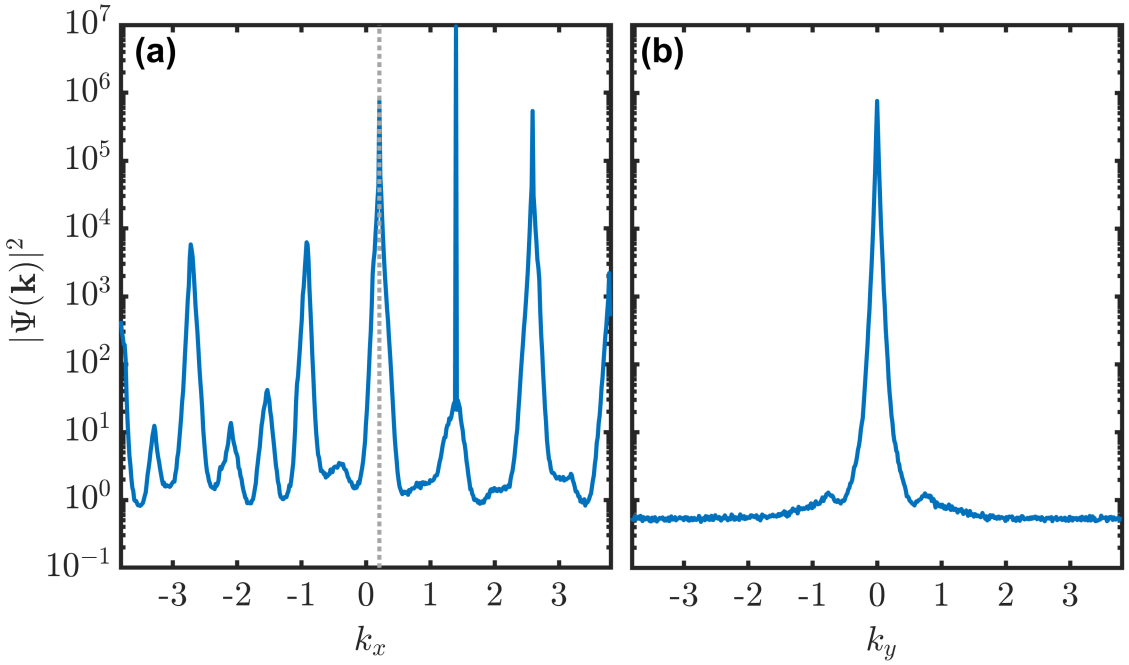

Figure 4.8: Steady state momentum distribution of OPO $|\Psi(\boldsymbol{k})|^2$ (log scale) at $f_p = 0.0327$. (a) Distribution in k_x along $k_y = 0$. Vertical dotted line shows signal momentum $k_x = k_s = 0.2084$. (b) Distribution in k_y at $k_x = k_s = 0.2084$.

Presuming that the strong stretched exponential fit of correlations in the y direction does result from the connection between polariton OPO and the KPZ universality, what then could be the cause of this distinct anisotropy and deviation from that behaviour seen in the x direction? The coefficients of the KPZ equation given for $f_p = 0.0327$ in Table 4.1, do not show strong enough anisotropy to account for this behaviour, so the reason must lie outside of the mapping of the polariton OPO to the KPZ equation. I propose as a possible explanation, that it is the presence of additional satellite modes distributed along k_x, beyond the three-mode description of OPO that leads to the KPZ equation, that alter the correlations along the x direction, while leaving the KPZ scaling behaviour in the y direction intact. To demonstrate this reasoning, Fig. 4.8 shows the cross-sections through

the signal peak of the momentum distribution at $f_p = 0.0327$. It can be seen that along k_x, although they are at least an order of magnitude smaller than the main signal peak, there are still a number of fairly strong satellite states. Meanwhile, there is no additional structure around the signal mode in the k_y direction. Even though the peaks of satellite states are excluded by the momentum filter I use to isolate the signal mode, it is possible that their presence still has an effect on the phase of the signal mode.

4.5 Checks for convergence of numerical results

In this section, I will describe the ways I check to determine that my numerical results represent the true steady state behaviour of the polariton OPO system. In particular, I will explore how my main result $g_s^{(1)}(x = 0, y)$ converges in time, to a steady state, and with the number of stochastic realisations used in its calculation, as well as to what extent it is independent of the size of the system considered.

4.5.1 Convergence to steady state

As I outlined in section 4.4, the numerical simulations are run using a mean field steady state as the initial condition until relevant observables reach their true steady state values, up to small fluctuations from the noise. As noted for similar simulations used in [39], the steady state should be independent of the initial conditions, but different physical observables can take different amounts of time to converge to a steady state, with the first order correlations $g_s^{(1)}(\boldsymbol{r})$ being the slowest relevant to this problem.

In Fig. 4.9, I show the convergence with time of $g_s^{(1)}(x = 0, y)$ calculated using 400 realisations, and without any time averaging, at separate times samples between $t = 0$ and $t = 160000$. The initial condition is completely coherent so produces a value of $g_s^{(1)}(\boldsymbol{r}) = 1$ for all $\boldsymbol{r}$. After $t = 0$, the values of $g_s^{(1)}(x = 0, y)$ quickly drift towards their actual steady state behaviour, initially overshooting it in terms of the speed of the decay of $g_s^{(1)}(x = 0, y)$ before relaxing back slightly. At times between $t = 120000$ and $t = 160000$, the shape of $g_s^{(1)}(x = 0, y)$ still fluctuates slightly but no longer seems to drift overall in time. As such, I determine that an average over the time samples between $t = 120000$ and $t = 160000$ is representative of the steady state behaviour, and use this time averaging over the steady state in all other results of this chapter.

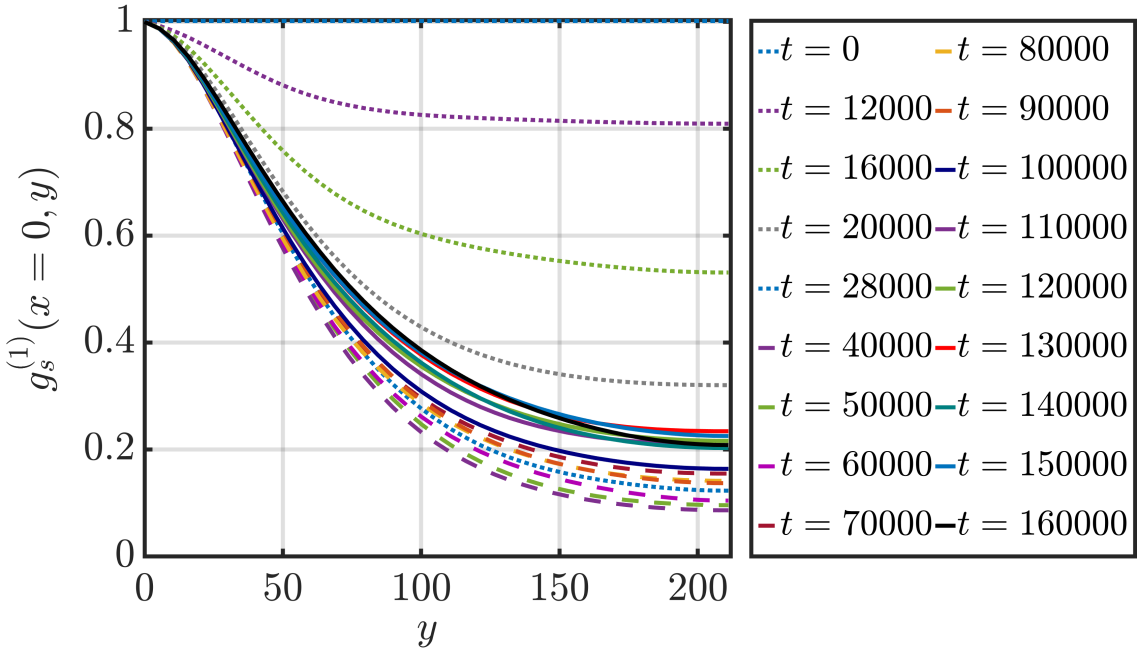

Figure 4.9: Calculated $g_s^{(1)}(x=0,y)$ at different times from $t=0$ to $t=160000$.

4.5.2 Convergence with number of stochastic realisations

For any stochastic method, it is important that the number of stochastic trajectories used is sufficient to sample the underlying probability distribution. Again, not all quantities are equally dependent on the noise; the momentum distributions of chapter 3, for example, often did not vary noticeably between individual realisations, while correlations are inherently noise dependent and so require averaging over many realisations to calculate correctly. Fig. 4.10 shows how $g_s^{(1)}(x=0,y)$ is affected by the number of realisations S used to calculate it. There are slight changes in $g_s^{(1)}(x=0,y)$ between $S=100$ and $S=400$, but beyond $S=200$ realisations the differences are truly negligible, suggesting that the total of 400 realisations used for my main results are more than sufficient. In the left panel and inset, I show how the errors $\Delta g_s^{(1)}(x=0,y)$ scale with S. The maximum of $\Delta g_s^{(1)}(x=0,y)$ for each S scales roughly as $1/\sqrt{S}$, with the maximum error for $S=400$ being approximately half of that for $S=100$.

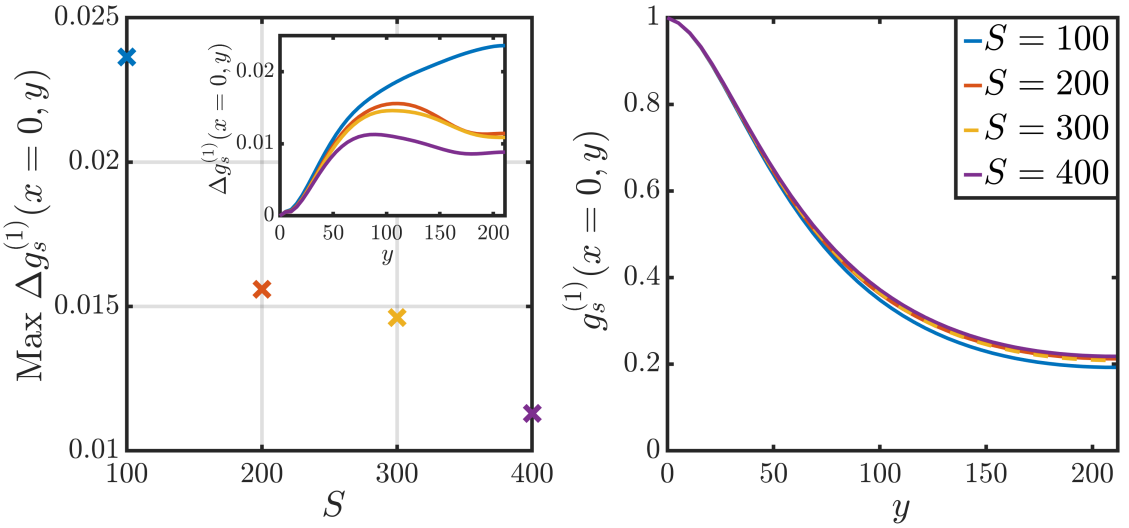

Figure 4.10: Calculated $g_s^{(1)}(x=0,y)$ and errors for different numbers of realisations used S between 100 and 400. Each case is also time averaged over the steady state. Left: maximum error $\Delta g_s^{(1)}(x=0,y)$ as a function of S. Inset: variation in error $\Delta g_s^{(1)}(x=0,y)$ with y. Right: $g_s^{(1)}(x=0,y)$ for different numbers of realisations S.

4.5.3 Convergence with system size

The final check is to make sure the results do not depend on the choice of system size considered. In practical terms, this can turn out to be quite difficult for OPO, as the many different momentum modes involved can make the system somewhat sensitive to geometry, especially when the discretisation of momentum space for numerical simulations is taken into account. The primary concern is that for the comparison to be valid, the signal momentum k_s must remain the same between the different system sizes, as the calculations shown in Fig. 4.2, which determine the f_p where KPZ scaling behaviour should appear, depend on its value. A minimum requirement for this is that the value $k_s = 0.2084$ lies on the momentum grid of the new system size. The simplest way to do this while maintaining the value of dV would be to double or half both N and L, but the doubled system $N = 1024$ is simply too large to simulate in a reasonable amount of time, while the $N = 256$ system did not produce exactly the same signal momentum as the larger system for $f_p = 0.0327$, giving $k_s = 0.1191$ instead.

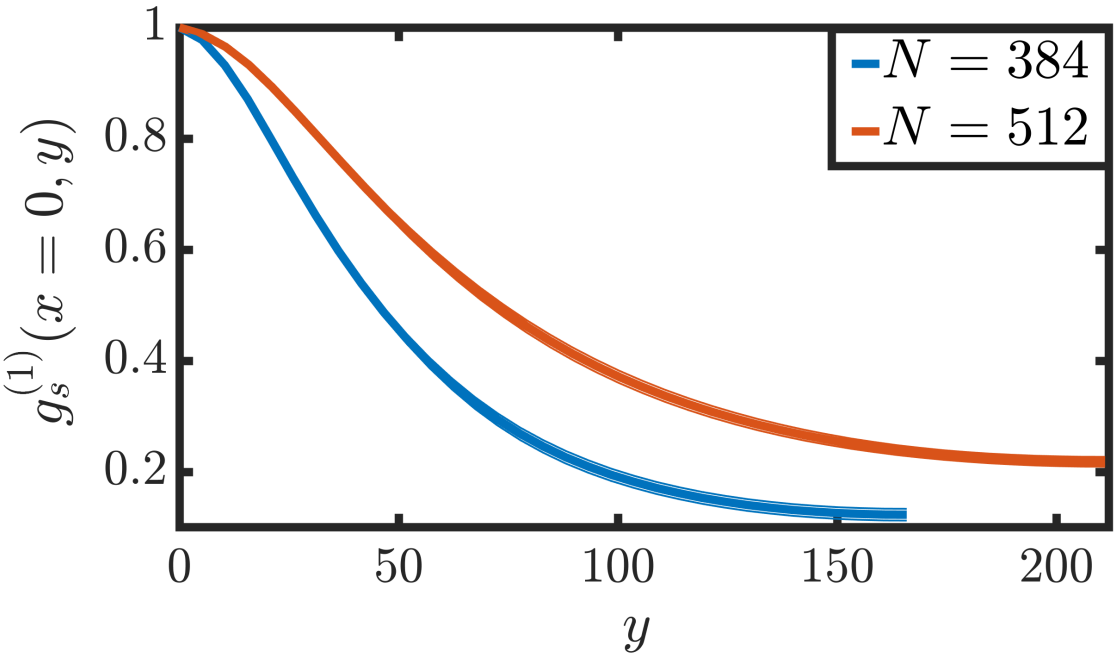

Figure 4.11: Calculated $g_s^{(1)}(x = 0, y)$ for different system sizes $N = 512$ ($L = 422.17544$, blue line) and $N = 386$ ($L = 331.70928$, red line). Each case is also time averaged over the steady state.

As an alternative, I choose an intermediate system size $N = 386$, $L = 331.70928$, which both allows and achieves $k_s = 0.2084$, while changing the cell area dV of the grid as little as possible. A comparison of $g_s^{(1)}(x = 0, y)$ for this system size with my main result is given in Fig. 4.11. While the behaviour is qualitatively similar, the two system sizes do not match exactly in $g_s^{(1)}(x = 0, y)$, even far from the edges.

However, although the exact form of $g_s^{(1)}(x = 0, y)$ is not completely independent of the system size for these values, it still shows a good fit to the stretched exponential decay with $\chi = 0.39$. This is shown by the fits of $g_s^{(1)}(x = 0, y)$ for the smaller system size $N = 386$ in Fig. 4.12. The correlations are fitted to the algebraic, exponential, and stretched exponential models, over a region $30 < y < 95$, and show very similar behaviour with regards to the relative strength of these fits as the analogous result for the original $N = 512$ given in Fig. 4.4. Ultimately, this demonstrates that while the exact form of OPO may not be completely independent of the geometry for the system sizes I have investigated, this should not detract from the ability to observe the KPZ scaling behaviour.

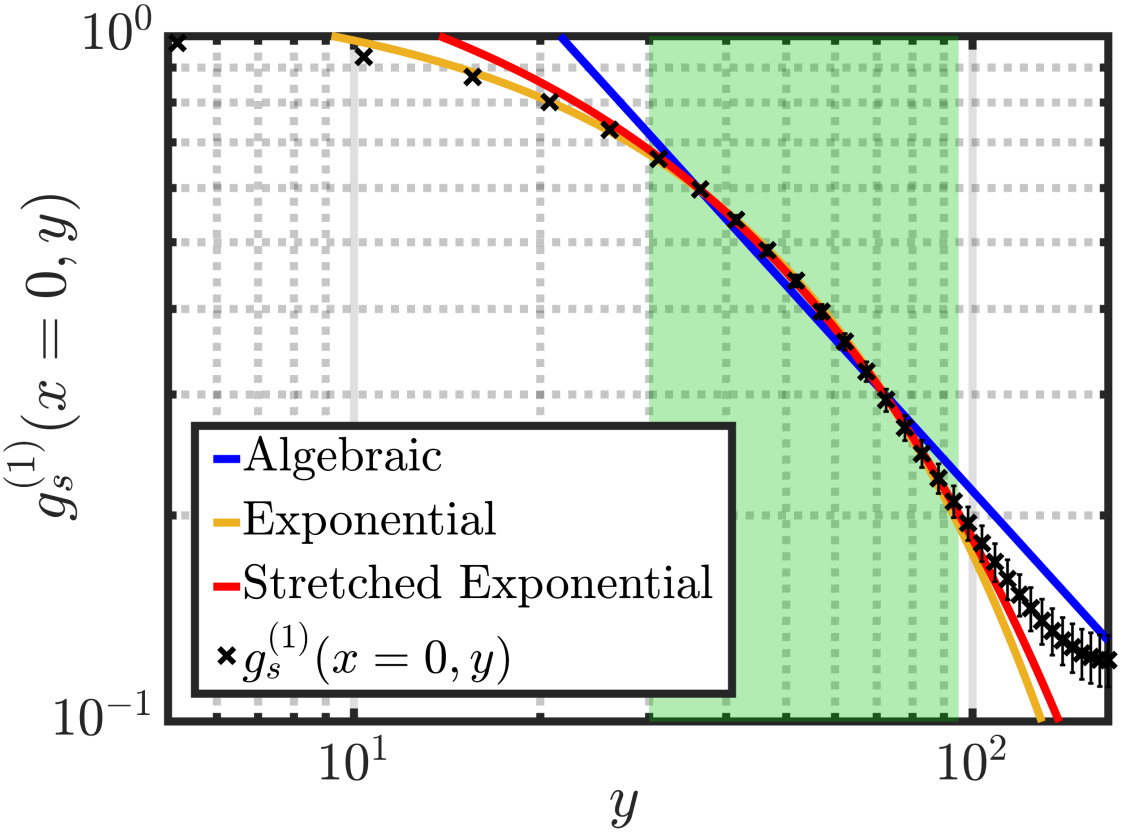

Figure 4.12: $g_s^{(1)}(x=0,y)$ with fits to algebraic (blue line), exponential (yellow line), and stretched exponential (red line) decay, for smaller system size ($N=384$). The green shaded region indicates the points included in the fit.

4.6 The fate of the vortex dominated phase

At this stage, there remains one open question with regards to observing a KPZ phase in polariton OPO. While so far, the results I have presented, starting with coherent initial conditions without vortices, show only evidence of the vortex free KPZ scaling behaviour, the analytical works which have motivated this study also describe a second possibility: a vortex dominated phase resulting from vortex-antivortex interactions under the influence of the KPZ equation switching from being attractive to repulsive beyond a certain range [78, 79]. Within the analytical predictions, which phase should win out in finite size systems depends on the relative sizes of the length scales associated with each phase appearing. The approximate length scales that were calculated for the isotropic case of $\lambda_x = \lambda_y = \lambda$ and $D_x = D_y = D$ are as follows: without vortices, the KPZ scaling phase

appears beyond a length scale

$$L_* = a_* e^{\frac{8\pi}{g_{KPZ}}}, \tag{4.14}$$

while vortices unbind at a length scale of

$$L_v = a_v e^{\left|\frac{2D}{\lambda}\right|}, \tag{4.15}$$

where a_* and a_v are some microscopic length scale in each case [43, 44, 78]. If we substitute λ_x and D_x for the respective isotropic coefficients λ and D, taking the parameters in table 4.1 for $f_p = 0.0327$ gives $L_v \sim a_v$ in this case, while $L_* \sim 10^3 a_*$, which suggests that, unless $a_* \ll a_v$, the vortex dominated phase should win out; but my results presented so far only show signs of the KPZ scaling phase without vortices. There are two possible explanations for this: either the KPZ scaling steady state I observe is actually just a very long lived metastable state that is reached first due my use of coherent initial conditions, or that effects which cannot be calculated in the mapping of the three-mode model of OPO to the KPZ equation, via the relative magnitudes of the microscopic length scales a_v, a_* or otherwise, conspire to cause the KPZ scaling phase to win out in real polariton OPO, at least up to the system sizes I consider if not also more generally.

To test which of these is the case, I look at the behaviour of the average number of vortices and antivortices, defined in section 4.2.3 as n_{v+av}, over 10 realisations, when starting from highly disordered initial conditons with $f_p = 0.0327$. I plot this in Fig. 4.13. At early times, n_{v+av} decays quickly from its large initial value before moving to a much slower rate of decay from when $n_{v+av} \sim 10$. Although the decay of vortices is extremely slow at late times, it shows no signs of saturating to a non-zero value. I demonstrate this by fitting the tail in Fig. 4.13 to an algebraic decay

$$n_{v+av}(t) = \left(\frac{t}{t_0}\right)^{-\alpha_t}, \tag{4.16}$$

for times beyond $t = 320000$. The fit gives $\alpha_t = 0.55$, with similar values $0.5 \leq \alpha_t < 0.7$ occurring if the initial time of the fit is varied. Eventually, a value of $n_{v+av} < 2$ is reached, indicating that at least one of the realisations has reached a state with zero vortices. While

this suggests that, at least for a finite size system, the number of vortices will eventually decay to zero, and the vortex dominated steady state is not reached, the exponent of the algebraic decay of n_{v+av} is also slower than the equilibrium value of $\alpha_t = 1$ (with logarithmic correction) seen in previous numerical studies of phase ordering in polariton OPO [41], which may be a result of the altered vortex interactions due to the KPZ.

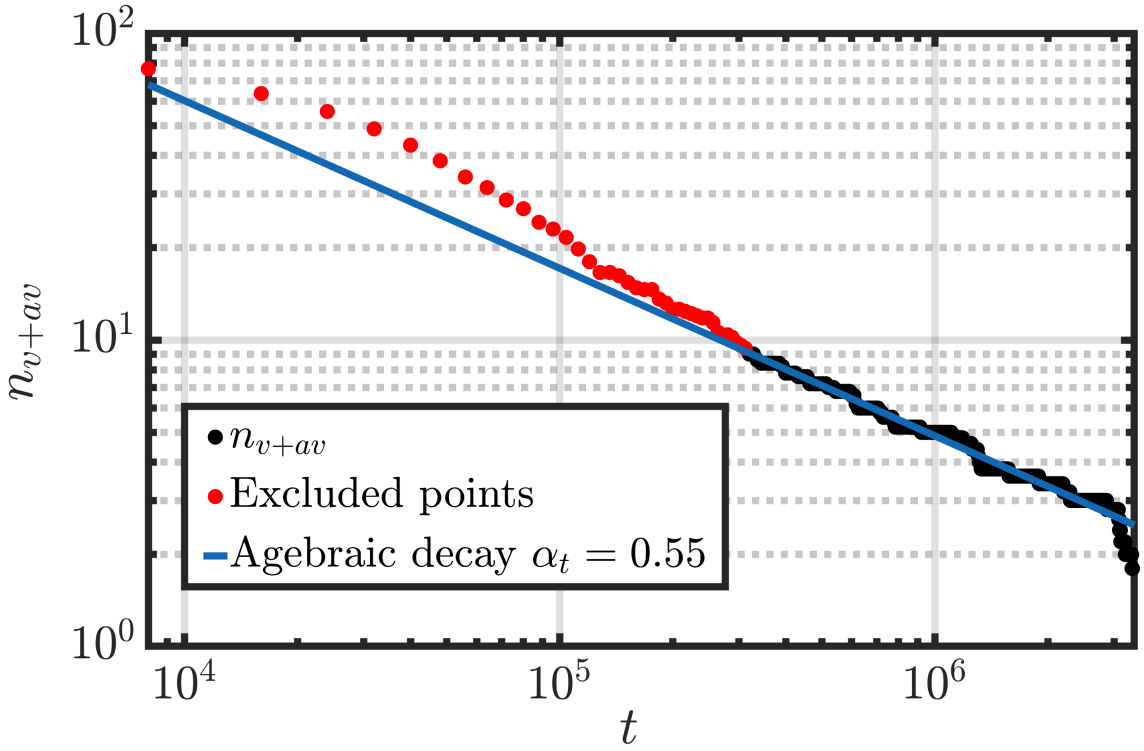

Figure 4.13: Average number of vortices and antivortices n_{v+av} with time, when starting from highly disordered initial conditions with $f_p = 0.0327$. The blue line shows fit to algebraic decay of n_{v+av} with time at late times $t \geq 320000$, with exponent $\alpha_t = 0.55$.

Some examples of spatial phase profiles from single realisations of the signal mode at $t = 320000$ are shown in Fig. 4.14, with the positions of vortices and antivortices indicated. The signal mode is isolated using the same signal filter around $k_s = 0.2084$ as the main result. Around some of the vortices can be seen a characteristic spiral wave pattern in the phase, which is associated with the behaviour of vortices under the compact KPZ equation [117].

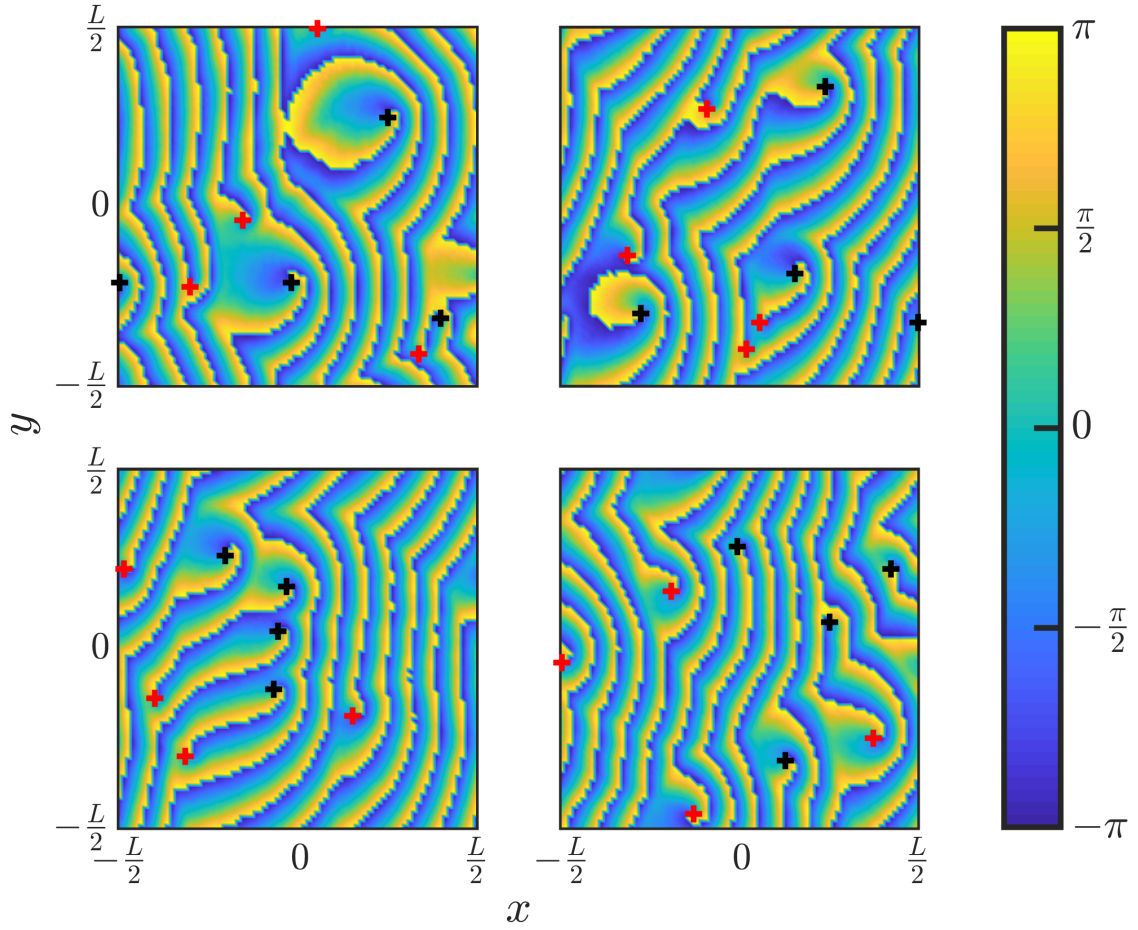

Figure 4.14: Four examples of the spatial variation in the phase of the filtered signal mode, using $k_s = 0.2084$, for single realisations at $t = 320000$ after highly disordered initial conditions. Locations of vortices and antivortices are marked with black and red crosses respectively.

4.7 Summary and Outlook

To conclude, my results here demonstrate behaviour primarily consistent with the appearance of a KPZ scaling regime in the polariton OPO system, albeit with some alterations that may be a consequence of the more complicated form of real polariton OPO compared to the three-mode model for which the mapping to the KPZ equation was derived. Specifically, for one value of the pump strength in the window where the length scales for observing KPZ shrink below the system size, I show that first order spatial correlations decay much more rapidly than for pump strengths far from the window, and fit well, in the direction perpendicular to the pump momentum, to the characteristic stretched exponential decay with $\chi = 0.39$ associated with the KPZ scaling phase. While these results

are largely in agreement with the analytical predictions of [44], which motivated this work, there are a number of complications or additional observations that the three-mode analytical model of OPO, and resulting mapping to the KPZ equation, could not take into account, such as the alteration of the form of correlations in the direction parallel to the pump momentum and the absence of the vortex dominated KPZ phase. These features ultimately justify the necessity of this sort of full numerical study beyond the work of [44]. Finally, I believe the work I have presented in this chapter gives a good indication that such evidence of the KPZ scaling phase could be observed in a similar way in polariton OPO experiments.

Chapter 5

Positive-P simulations of driven-dissipative Bose-Hubbard Lieb lattices

This chapter concerns results of positive-P simulations of the driven-dissipative Bose-Hubbard (DDBH) model produced by numerically integrating equations (2.32). In [3], simulations by Piotr Deuar were used to establish the regimes of applicability of the positive-P method in the parameter space of the single site case. Here, in my contributions to [3] and follow-up work, I go beyond that to study many site DDBH lattices. I concentrate on Lieb lattices (see Fig. 5.1) and related geometries, which can display a range of interesting physics due to frustation and interference effects, and have been widely studied in polariton micropillar lattices [54, 56, 58, 59], which I focus on as the primary physical context for the investigations performed in this chapter. The results of section 5.1.2, specifically, are published in [3]. Compared to the more general form of the DDBH model given by (2.22) with (2.23), in this chapter, except where otherwise stated, I consider lattices with uniform local parameters $\Delta_j = \Delta$, $U_j = U$, $\gamma_j = \gamma$, and hopping $J_{j,j'} = J$ only if sites j and j' are nearest neighbours, with $J_{j,j'} = 0$ for all other pairings of more distantly separated sites. For all numerical results presented in this chapter, simulations were performed using XMDS2 [85], with scripts written by myself, and the output processed using MATLAB.

5.1 Benchmarking with bunching results

I begin my investigations into DDBH Lieb lattices by reproducing the results of [4]. In that work, they explored strong bunching in the second order correlations on the dark sites that occurs when the coherent drive is applied to only a particular site in each unit cell. Reproducing these results serves as an interesting problem with which to benchmark my implementation of the positive-P method for this system, before going on to perform further explorations of my own design.

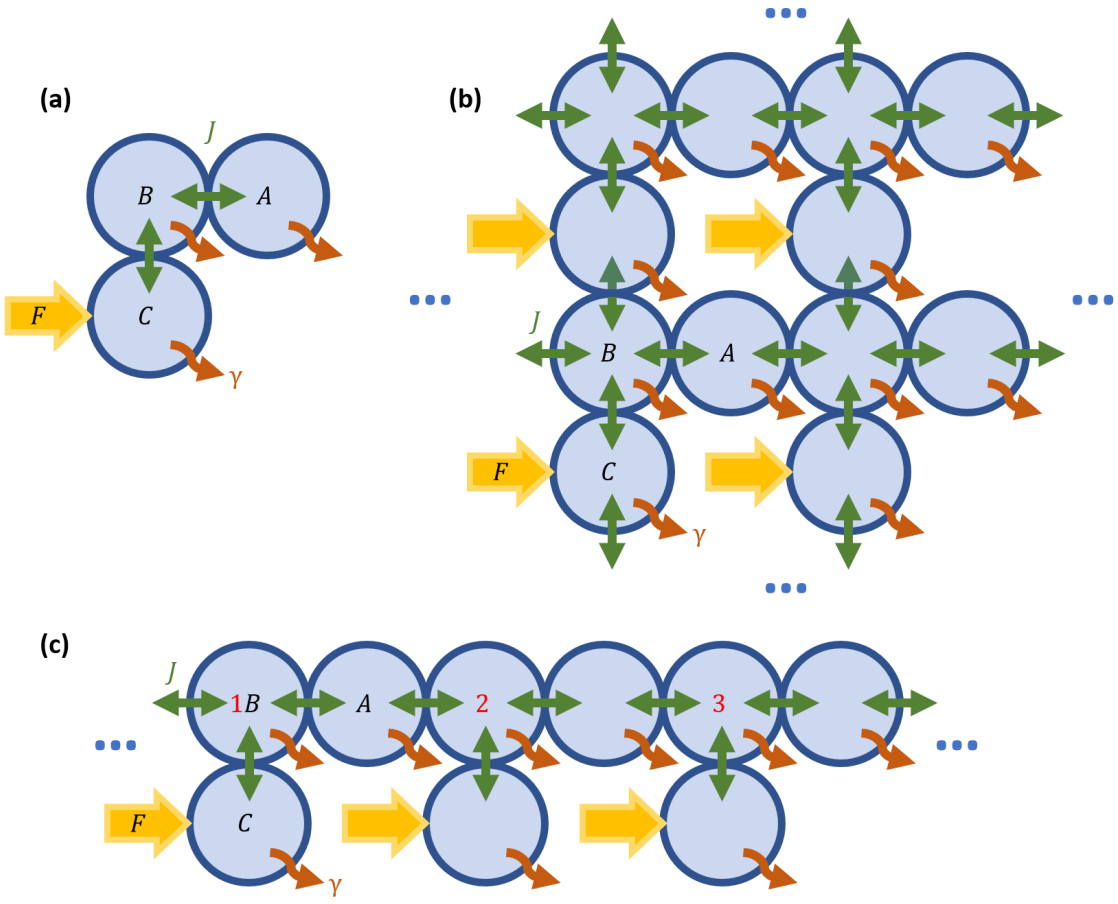

Figure 5.1: Diagram of the structures of Lieb lattices. (a) Single unit cell, equivalent to 3 site 1D chain with open boundaries. (b) 2D Lieb lattice. (c) Quasi-1D Lieb lattice, connected along line of A and B sites. In all cases, local dissipation γ occurs equally at all sites, and coherent drive F is applied only to the C sites, with hopping J between neighbouring sites allowing occupation to then spread to other sites in the lattice.

5.1.1 Choice of method and results for a single unit cell

As in [4], I will begin by considering the behaviour of a system of only one unit cell of the Lieb lattice. This system is completely equivalent to a one dimensional chain of 3 sites with nearest neighbour hopping, but I will introduce here the notation that will continue to be used for extended quasi-1D and 2D Lieb lattices. I label the three sites of the unit cell A, B, C, as shown in Fig. 5.1 (a). I consider a situation where the coherent drive F is applied only to the site labelled C, with Δ at or close to zero ($|\Delta| \leq 2$ at most). For small F, this arrangement primarily occupies a single boson eigenstate of the Bose-Hubbard Hamiltonian [(2.23) with $F \to 0$] for this geometry with energy $\Delta = 0$,

$$\frac{|001\rangle - |100\rangle}{\sqrt{2}}, \tag{5.1}$$

where $|n_A n_B n_C\rangle$ represents a Fock state with n_j bosons on site $j \in \{A, B, C\}$. This state has no amplitude for occupation of the B site due to the destructive interference between the hopping contributions, with equal but opposite amplitudes, from the A and C sites. Thus, for this three site DDBH model, and similarly for extended Lieb lattices, the described driving scheme results in a low occupation, or "dark site", occurring on the B site.

Before further investigations, I use a single example to determine which phase space method is best to proceed with. As an alternative to positive-P simulations, it could, in principle, be possible to use the truncated Wigner method to study this system. We can achieve this by applying a similar derivation to section 2.1, but to the model (2.22)-(2.23). For the specific case of the single Lieb unit cell, or 3 site chain, considered here, this produces the following stochastic differential equations for trajectories in the truncated Wigner representation,

$$\frac{\partial \alpha_A^{(TW)}}{\partial t} = \left(i\Delta - iU\left(|\alpha_A^{(TW)}|^2 - 1\right) - \frac{\gamma}{2}\right)\alpha_A^{(TW)} + iJ\alpha_B^{(TW)} + \sqrt{\frac{\gamma}{2}}\eta_A, \tag{5.2a}$$

$$\frac{\partial \alpha_B^{(TW)}}{\partial t} = \left(i\Delta - iU\left(|\alpha_B^{(TW)}|^2 - 1\right) - \frac{\gamma}{2}\right)\alpha_B^{(TW)} + iJ\alpha_A^{(TW)} + iJ\alpha_C^{(TW)} + \sqrt{\frac{\gamma}{2}}\eta_B, \tag{5.2b}$$

$$\frac{\partial \alpha_C^{(TW)}}{\partial t} = \left(i\Delta - iU\left(|\alpha_C^{(TW)}|^2 - 1\right) - \frac{\gamma}{2}\right)\alpha_C^{(TW)} + iJ\alpha_B^{(TW)} - iF + \sqrt{\frac{\gamma}{2}}\eta_C, \tag{5.2c}$$

where η_j, for $j \in \{A,B,C\}$, are complex gaussian noises with $\langle \eta_j(t) \rangle = 0$ and $\langle \eta_j(t)\eta_{j'}(t') \rangle = \delta_{j,j'}\delta(t-t')$. Important observables of interest are the occupation

$$n_j = \langle \hat{a}_j^\dagger \hat{a}_j \rangle , \tag{5.3}$$

and the local second order correlation function

$$g_j^{(2)}(0) = \frac{\langle \hat{a}_j^\dagger \hat{a}_j^\dagger \hat{a}_j \hat{a}_j \rangle}{n_j^2} , \tag{5.4}$$

which in the Wigner representation are calculated as

$$n_j = \langle |\alpha_j^{(TW)}|^2 \rangle_{TW} - \frac{1}{2} , \tag{5.5a}$$

$$g_j^{(2)}(0) = \frac{\langle |\alpha_j^{(TW)}|^4 \rangle_{TW} - 2\langle |\alpha_j^{(TW)}|^2 \rangle_{TW} + \frac{1}{2}}{n_j^2} , \tag{5.5b}$$

where $\langle ... \rangle_{TW}$ refers to, in practice, averages over many trajectories produced by solving equations (5.2) numerically for different realisations of the noises η_j.

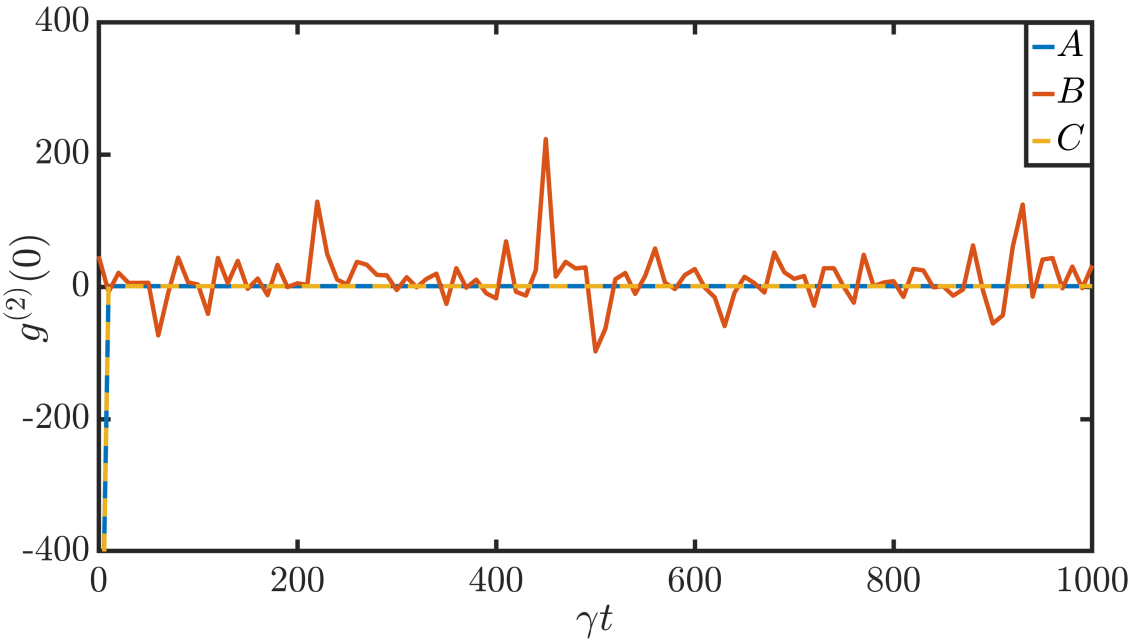

Figure 5.2: Local $g^{(2)}(0)$ of sites in Lieb unit cell calculated from truncated Wigner simulations. Parameters $U = 0.1\gamma$, $F = \gamma$, $J = 5\gamma$, $\Delta = 0$. The truncated Wigner result fails to converge properly for the dark site B.

For the positive-P method, these normally ordered observables are calculated in a straight forward way from numerical solutions of the appropriate arrangement of (2.32),

$$n_j = \langle \alpha_j \beta_j \rangle_{PP}\,, \tag{5.6a}$$

$$g_j^{(2)}(0) = \frac{\langle \alpha_j^2 \beta_j^2 \rangle_{PP}}{n_j^2}\,, \tag{5.6b}$$

with the notation $\langle ... \rangle_{PP}$ similarly referring to averages over trajectories of the positive-P simulations.

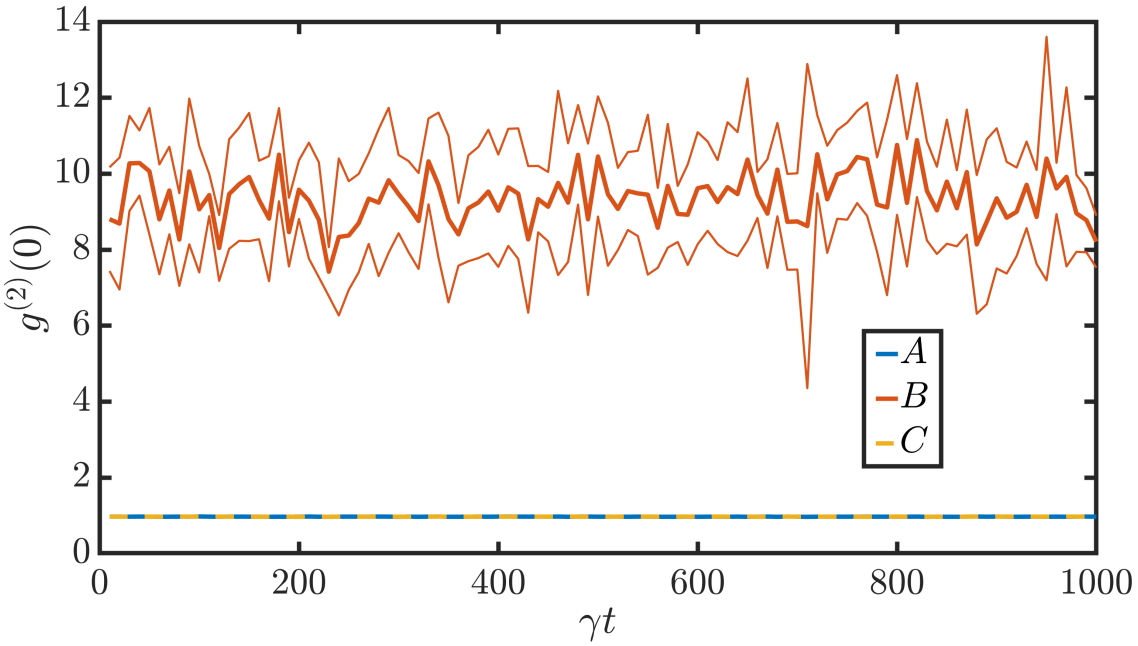

Figure 5.3: Local $g^{(2)}(0)$ of sites in Lieb unit cell calculated from Positive-P simulations. Parameters $U = 0.1\gamma$, $F = \gamma$, $J = 5\gamma$, $\Delta = 0$. Thin outer lines, only distinguishable for site B, show the errors.

To determine which method to use for this project going forward, I compare the truncated Wigner and positive-P results for a single example, using the parameters $U = 0.1\gamma$, $F = \gamma$, $J = 5\gamma$, $\Delta = 0$. For both methods, I average over a total of 10000 trajectories for this example. While the truncated Wigner method works fine for obtaining the occupations n_j, I show in Fig. 5.2 that, due to the small occupation of the dark B site, where quantum fluctuations are proportionally more significant, it fails to give useful results for $g_B^{(2)}(0)$. On the other hand, Fig. 5.3 shows fairly well converged values for $g^{(2)}(0)$ on all sites, showing that positive P is the more useful method for this particular problem.

A more in depth analysis and comparison of the regimes of usefulness of the truncated Wigner and positive-P methods for simulating the DDBH model, performed by some of my collaborators, can be found published in our work [3].

Now using the positive-P method, I explore the variation of the occupation and local $g^{(2)}$ of the B site in a single unit cell with the pump detuning Δ, as shown in figures 2 (b) and 3 (a) in [4] respectively. Results for these given in Fig. 5.4 and Fig. 5.5 show a good match to the results of exact diagonalisation of the master equation using a truncated number state basis, like those given in [4], which were provided to me by Conor McKeever. The variation of $g_B^{(2)}(0)$ with Δ shows a peak of strong bunching (i.e. $g_B^{(2)}(0) > 1$ [65]) centered around $\Delta = -0.25\gamma$, with an associated peak in n_B slightly offset from it at $\Delta = -0.1\gamma$. The strong bunching results from resonance with two boson eigenstates of the Bose-Hubbard Hamiltonian in the presence of interactions $U \neq 0$, which exhibit a probability for a pair of bosons to occupy the B site; since the most likely single boson state (5.1) gives no population on site B, the contribution to the population of this site comes almost entirely from these doubly occupied states, giving a large value of $g_B^{(2)}(0)$ [4].

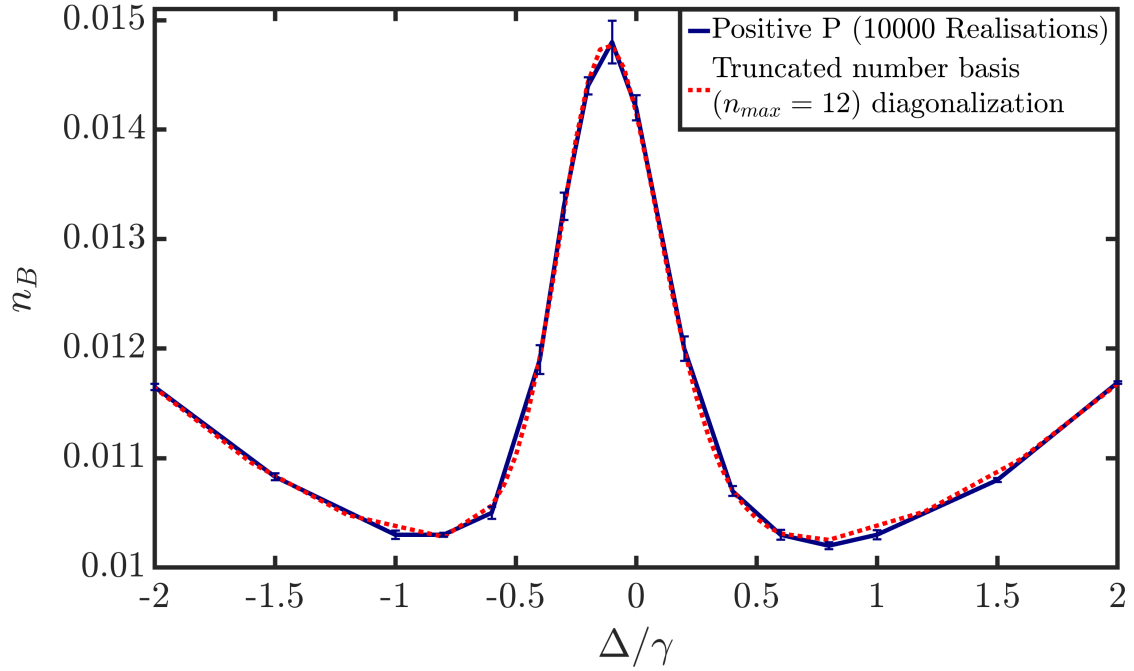

Figure 5.4: Occupation of B site versus pump detuning Δ for $U = 0.1\gamma$, $F = \gamma$, $J = 5\gamma$. My positive-P results (blue) are compared to exact diagonalisation results provided by Conor McKeever (dotted red).

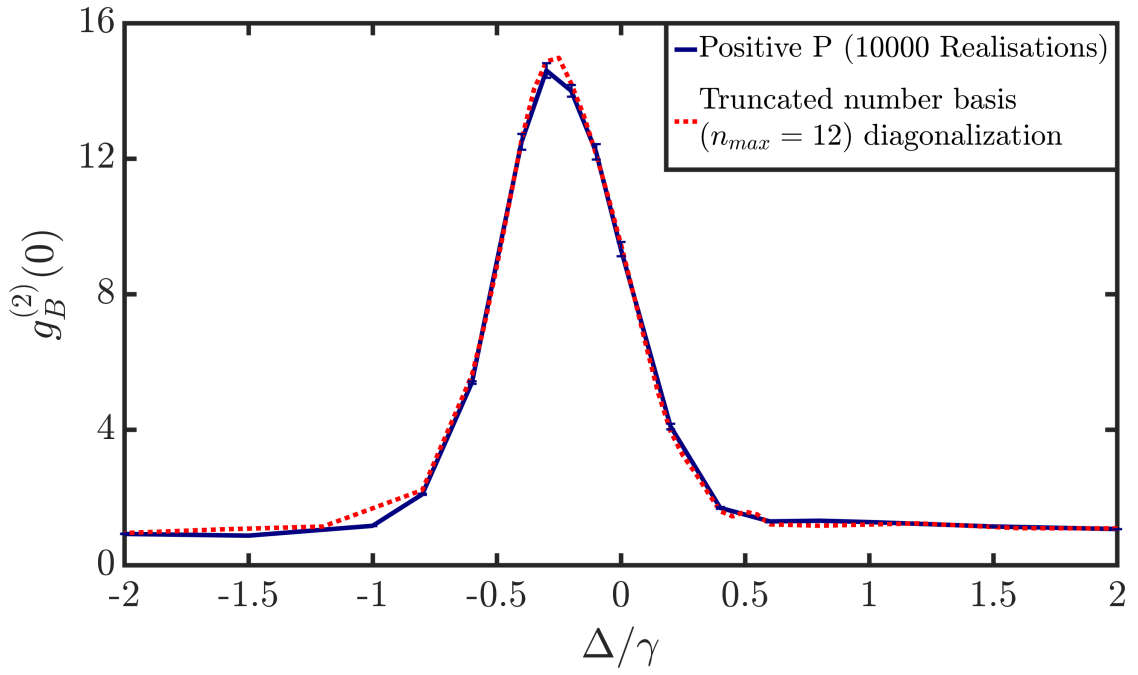

Figure 5.5: Local $g^{(2)}(0)$ of B site versus pump detuning Δ for $U = 0.1\gamma$, $F = \gamma$, $J = 5\gamma$. My positive-P results (blue) are compared to exact diagonalisation results provided by Conor McKeever (dotted red).

5.1.2 1D and 2D Lieb lattices with periodic boundary conditions

Continuing to follow [4], I next implemented positive-P simulations for 1D and 2D Lieb lattices, as indicated by the diagrams in Fig. 5.1 (c) and (b) respectively, with periodic boundary conditions. Parameters were chosen to compare to Table I in [4]. This means that $U = 0.3\gamma$, $F = 0.1\gamma$, and $\Delta = 0$ in all cases. The system sizes were 12 unit cells for 1D lattices and 4×4 unit cells for 2D lattices. Following [4], I calculate three observables in particular: the ratio of occupations between the B and A sites n_B/n_A, the local second order correlation of the B sites $g_B^{(2)}$, and the non-local second order correlation between B sites in adjacent unit cells $g_{B,NN}^{(2)}$, which is averaged over all directions for the 2D case. Since the system with periodic boundary conditions is spatially uniform, i.e. all unit cells are equivalent, during the stochastic averaging procedure used when calculating observables from the positive-P simulation results I also average over all unit cells in the lattice, as well as over time samples from once the steady-state has been reached, following similar logic to the justification of spatial averaging. These additional sources of averaging allow larger system sizes to be converged with a smaller total number of samples, saving

computational time. The local observables n_B/n_A and $g_B^{(2)}$ can be calculated as defined in equations (5.6). The non-local correlation $g_{B,NN}^{(2)}$ is defined as

$$g_{B,NN}^{(2)} = \frac{\langle \hat{a}_{B,j}^{\dagger} \hat{a}_{B,j'}^{\dagger} \hat{a}_{B,j'} \hat{a}_{B,j} \rangle}{n_{B,j} n_{B,j'}}, \tag{5.7}$$

where I now label the sites as S, j with $S \in \{A, B, C\}$ and the index j labels the unit cells, with j and j' here being nearest neighbouring unit cells. This can be calculated in the positive-P representation as

$$g_{B,NN}^{(2)} = \frac{\langle \alpha_{B,j} \alpha_{B,j'} \beta_{B,j'} \beta_{B,j} \rangle_{PP}}{n_{B,j} n_{B,j'}}, \tag{5.8}$$

with the $\langle ... \rangle_{PP}$ now including averaging over unit cells for the periodic lattice. Results for 1D and 2D lattices are summarised in Table 5.1, with comparisons to the corner space renormalization method results of [4].

N_{cells}	J/γ	n_B/n_A	$g_B^{(2)}$	$g_{B,\text{NN}}^{(2)}$	method (samples)
12	2	0.0180(5)	342(8)	19.3(4)	CSR [4]
12	2	0.0176(4)	342(16)	19.0(5)	Positive P (10^4)
12	1	0.0650(3)	23.3(2)	2.35(2)	CSR [4]
12	1	0.065(1)	23(1)	2.30(6)	Positive P (1000)
100	1	0.0648(2)	23.3(2)	2.36(4)	Positive P (1000)
4×4	2	0.0161(1)	66.2(2)	1.42(3)	CSR [4]
4×4	2	0.0161(3)	65(2)	1.2(2)	Positive P (1000)
4×4	1	0.0631(1)	4.41(1)	0.996(2)	CSR [4]
4×4	1	0.0628(3)	4.42(3)	0.99(2)	Positive P (1000)
10×10	1	0.0632(2)	4.68(3)	0.996(5)	Positive P (1000)
100×100	1	0.06309(8)	4.685(2)	0.995(2)	Positive P (100)

Table 5.1: Comparison between positive-P and corner space renormalization (CSR) calculations for the stationary state of 1D (top) and 2D (bottom) Lieb lattices with periodic boundary conditions. For my positive-P results, I also include in parentheses the number of stochastic samples used. Parameters are $U = 0.3\gamma$, $\Delta = 0$, and drive $F = 0.1\gamma$ applied to the C sites, with J between neighbouring sites varied as shown in the table. These results are also presented in [3].

One advantage of the positive-P over the corner space renormalization method of [4] that I am benchmarking it against, is that it is much more easily scalable to larger system sizes. As such, while the system sizes considered in [4] are fixed at 12 unit cells for the quasi-1D lattice and 4×4 unit cells for the 2D lattice, I also include in Table 5.1 results for much larger lattices, of 100 unit cells and even up to 100×100 for the 2D lattice. From this we can see that, while for the 1D case all observables investigated seem to be converged with respect to changing system size, for 2D cases, the local $g_B^{(2)}$ for the 4×4 unit cell lattice does not seem to reach its asymptotic value for large system sizes, which I can obtain successfully using the scalability of the positive-P method. These results were used in [3] to demonstrate the accuracy of the positive-P method in situations with nontrivial quantum correlations (e.g. far from $g^{(2)}(0) = 1$ associated with coherent states), as well as its scalability to very large systems.

5.1.3 Notes on error estimating procedure and averaging

The errors on the positive-P results provided within the tables and figures in this chapter are obtained by splitting the total number of stochastic realisations into a number of separate bins and calculating the observables separately for each bin: the reported value is the mean of the values for each bin and the reported error estimate is their standard deviation. In the limit that both the number of realisations per bin and the number of bins is large enough, the error estimate provided by this method should become independent of the number and size of the bins, depending only on the total number of realisations [84]; while the total number of realisations used here is not quite enough to have simultaneously very large numbers of both bins and realisations per bin, and thereby reach the limit where the error estimate is completely independent of the choice of binning procedure, the error estimates provided by this procedure should nonetheless give a good representation of the precision obtained with the current total numbers of realisations used. I have chosen to report in the tables using the output provided by splitting the realisations into 5 bins, since it is most important that the number of realisations in each bin is enough to get convergence of calculated observables, and this seemed to provide the best compromise between bin size and bin number overall.

5.1.4 1D Lieb lattice with open boundary conditions

I next look at the 5 unit cell open boundary chain, which I replicate the diagram of here in Fig. 5.6, and attempt to reproduce the associated results given in Table II of [4]. The physical parameters of the model for this chain are $U = 0.3\gamma$, $F = 0.1\gamma$, $\Delta = 0$, and $J = 2\gamma$. For each B site in the chain (labelled by j), the occupation normalised to the occupation of the brightest site in the chain $n_{B,j}/n_{max}$, the local second order correlation $g^{(2)}_{B,j}$, and the non-local second order correlation with the first site $g^{(2)}_{B,1;B,j}$, from the positive-P simulations are reported in Table 5.2. The non-local correlation $g^{(2)}_{B,1;B,j}$ is defined and calculated as

$$g^{(2)}_{B,1;B,j} = \frac{\langle \hat{a}^{\dagger}_{B,1}\hat{a}^{\dagger}_{B,j}\hat{a}_{B,j}\hat{a}_{B,1}\rangle}{n_{B,1}n_{B,j}} = \frac{\langle \alpha_{B,1}\alpha_{B,j}\beta_{B,j}\beta_{B,1}\rangle_{PP}}{n_{B,1}n_{B,j}}. \tag{5.9}$$

Since the open boundary chain is no longer spatially uniform, spatial averaging can no longer be included in the process of calculating observables, which reduces the precision per realisation and increases the number of realisations needed for convergence. The total number of realisations used for the results in Table 5.2 is 50000 (binned as 5×10000 realisations). The positive-P results agree well with the corresponding corner space renormalization method results from [4], albeit for the lowest occupation sites only a modest precision is achieved even for the large number of stochastic samples used here.

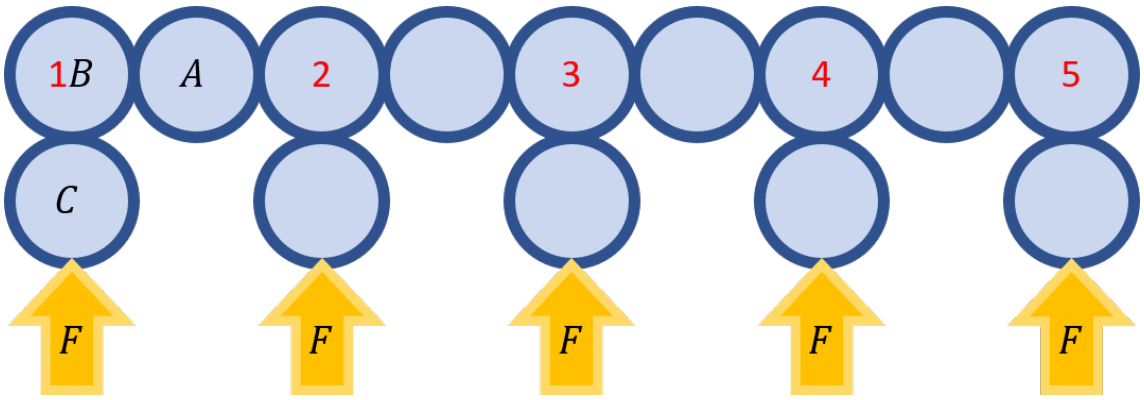

Figure 5.6: Diagram of 5 unit cell quasi-1D Lieb lattice with smooth edges, i.e. there is no A site on the final unit cell, with open boundary conditions. Drive is applied to each C site.

unit cell j	method	$n_{B,j}/n_{max}$	$g^{(2)}_{B,j}$	$g^{(2)}_{B,1;B,j}$
1	Positive P	$1.51(1)\times10^{-2}$	15.4(3)	15.4(3)
	CSR [4]	$1.514(5)\times10^{-2}$	15.42(7)	15.42(7)
2	Positive P	$1.10(9)\times10^{-3}$	$4.0(7)\times10^{3}$	5.0(8)
	CSR [4]	$1.13(3)\times10^{-3}$	$3.9(1)\times10^{3}$	5.11(7)
3	Positive P	$5.70(5)\times10^{-3}$	108(2)	1.3(1)
	CSR [4]	$5.65(3)\times10^{-3}$	111.4(8)	1.45(2)
4	Positive P	$1.13(3)\times10^{-3}$	$3.8(2)\times10^{3}$	2.6(7)
	CSR [4]	$1.12(3)\times10^{-3}$	$4.0(1)\times10^{3}$	2.78(3)
5	Positive P	$1.509(7)\times10^{-2}$	15.37(2)	1.00(4)
	CSR [4]	$1.515(5)\times10^{-2}$	15.42(5)	1.014(1)

Table 5.2: Occupations and second order correlations from positive-P simulations, compared to corner space renormalization (CSR) results from [4], for open boundary 1D Lieb chain with $U=0.3\gamma$, $F=0.1\gamma$, $\Delta=0$, and $J=2\gamma$.

5.1.5 Quadratures and squeezing

Finally, looking beyond the observables considered in [4], I consider the quadratures $\hat{x}=\frac{1}{2}(\hat{a}+\hat{a}^\dagger)$ and $\hat{p}=\frac{1}{2i}(\hat{a}-\hat{a}^\dagger)$, to look for possible squeezing in the state of any of the sites. For this I return to the data from the 1D and 2D lattices with periodic boundary conditions. To determine the direction along which any squeezing might occur, I first look at the quadratures of the positive-P distribution itself, by plotting the unaveraged phase space quadratures $x=\frac{1}{2}\mathrm{Re}\,(\alpha+\beta)$ against $p=\frac{1}{2}\mathrm{Im}\,(\alpha-\beta)$ for each realisation and site in the lattice.

An example of this for the 1D chain with $J=2\gamma$ is shown in Fig. 5.7; equivalent plots for the other cases appear very similar. While the positive-P distributions appear quite elliptical in Fig. 5.7, this does not on its own show that significant squeezing is occurring; the variance in the phase space distribution does not necessarily correspond to the variance of observables. Instead, I use this plot to estimate the angle ϕ along which any actual squeezing might be occurring, and then measure the variances, $\Delta x'=\sqrt{\langle\hat{x}'^2\rangle-\langle\hat{x}'\rangle^2}$, $\Delta p'=\sqrt{\langle\hat{p}'^2\rangle-\langle\hat{p}'\rangle^2}$ of the rotated quadratures, $\hat{x}'=\frac{1}{2}(\hat{a}e^{-i\phi}+\hat{a}^\dagger e^{i\phi})$ and $\hat{p}'=\frac{1}{2i}(\hat{a}e^{-i\phi}-\hat{a}^\dagger e^{i\phi})$. Upon measuring, the actual degree of

squeezing, i.e. the deviation of the variances from $\Delta x' = \Delta p' = 0.5$, turns out to be almost negligible (less than 1%), but this is nonetheless a useful tool to have for future cases where squeezing might be relevant.

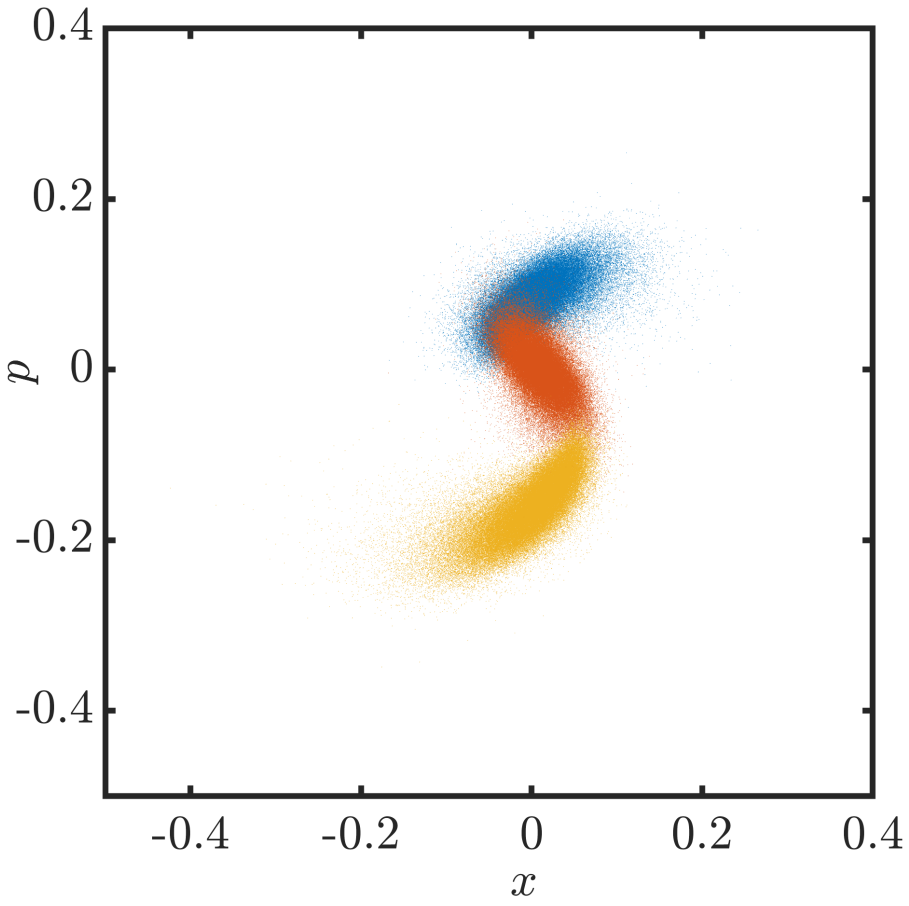

Figure 5.7: Quadratures of Positive-P distribution for 12 unit cell 1D Lieb chain with periodic boundaries at $U = 0.3\gamma$, $F = 0.1\gamma$, $\Delta = 0$, and $J = 2\gamma$. Points are colour coded by the corresponding site within the unit cell: A blue, B red, C yellow.

5.2 Antibunching in locally driven Lieb lattices

The results of [4], and my corresponding results of positive-P simulations presented in section 5.1, focus on bunching in the second order correlations of the dark B sites. In this section, I investigate how the interference effects can be altered to give antibunching on the dark sites. Antibunching (i.e. $g^{(2)}(0) < 1$) is often taken as a sign of quantum correlations, as it cannot occur classically [65]. Normally, to achieve strong antibunching in the DDBH lattices would require strong interactions $U \gg \gamma$, which would cause the

positive-P method to fail [3]. However, applying the drive in a specific localised way can produce strong antibunching on certain sites, even when the interactions are fairly weak, via a mechanism similar to the so-called unconventional photon blockade seen in the two site system [118].

5.2.1 Unconventional photon blockade

First discovered in [118], the unconventional photon blockade (UPB) is a mechanism that results in strong antibunching on the one driven site of a pair of coupled resonators, such as a DDBH dimer. The effect is caused by destructive interference between different paths that eliminates the probability of multiple occupation of the relevant site; for example, in the DDBH dimer the amplitude for a second boson to occupy the driven site by the coherent drive is cancelled, either partially or completely, by the amplitude for a second boson to occupy the driven site by first hopping back to it from the second site [119]. Since the initial proposal, there have been a number of further investigations into different implementations of the UPB and the physics behind it [119–129] and even some successful experimental realisations of it [130, 131], all of which are focused on two site systems, as in the original proposal.

A characteristic feature of the UPB can be seen in the form of the time delayed second order correlations

$$g_j^{(2)}(\tau) = \frac{\langle \hat{a}_j^\dagger(t)\hat{a}_j^\dagger(t+\tau)\hat{a}_j(t+\tau)\hat{a}_j(t)\rangle}{n_j(t)n_j(t+\tau)}. \tag{5.10}$$

In the case of the UPB, these correlations oscillate with the delay τ, with a period inversely proportional to the hopping J [118, 119]. In experiments, photon detectors needed for performing measurements of $g_j^{(2)}(0)$ will typically have some finite resolution in time. To detect the antibunching from the UPB, it is therefore useful for the period of these oscillations to be as long as possible, especially compared to the time resolution of the detectors.

There are some inherent similarities between the physics of the UPB and that of the dark sites in Lieb lattices. In the UPB, interference reduces the probability of two bosons occupying the same site, which decreases $g_j^{(2)}(0)$, while in the Lieb lattice, interference

reduces the probability of one boson occupation of the dark site, but leaves some probability of double occupation, resulting in the strong bunching in $g_j^{(2)}(0)$ that I explore in section 5.1. It is therefore reasonable to wonder if it is possible to tune the interference effects in the Lieb lattice and related structures in order to produce strong antibunching of $g_j^{(2)}(0)$ by a similar mechanism to the UPB. I explore this possibility in this section.

5.2.2 Optimal parameters for antibunching in three site chain

I once again begin by considering the simplest example relevant to Lieb lattices, a single unit cell or three site 1D chain, shown in Fig. 5.1 (a). This system has the advantage of being small enough that it is still possible to make progress with some of the analytical techniques that have been used to study the two site UPB. In particular, I take the method of [119], where the optimal parameters for UPB are found by solving the master equation in the weak driving limit when setting the amplitude for two bosons to occupy relevant site to 0, and apply it to the three site chain, where the amplitude I set to 0 in this case is that for two bosons to occupy the middle (B) site.

This process, which I detail fully in appendix C, leads to a pair of equations which relate the values of physical parameters that produce optimal antibunching of the middle site,

$$4\Delta^3 - U\Delta^2 - 3\gamma^2\Delta - J^2U + \frac{U\gamma}{4} = 0\,, \tag{5.11a}$$

$$6\gamma\Delta^2 - U\gamma\Delta - \frac{\gamma^3}{2} = 0\,. \tag{5.11b}$$

I identify Δ_{opt} and J_{opt} as the values of Δ and J that give optimal antibunching, i.e. that solve the equations (5.11), for a given value of U and γ. Solving the quadratic equation (5.11b) for Δ gives

$$\Delta_{opt} = \frac{U \pm \sqrt{U^2 + 12\gamma^2}}{12}\,, \tag{5.12}$$

which can then be used with the solution of (5.11a), to find the corresponding J_{opt} as

$$J_{opt} = \sqrt{\frac{\gamma^2}{4} - \Delta_{opt}^2 + \frac{4\Delta_{opt}^3}{U} - \frac{3\gamma^2\Delta_{opt}}{U}}\,, \tag{5.13}$$

noting that only the negative solution of (5.12) gives real values of J_{opt}.

The solutions of (5.12) and (5.13) across orders of magnitude in U are shown in Fig. 5.8. The behaviour is qualitatively similar to the equivalent for the UPB on two sites calculated in [119]; however, the limit of J_{opt} as $U \to \infty$ is smaller for the three site chain, $J_{opt} \to \gamma/2$ as opposed to $J_{opt} \to \gamma/\sqrt{2}$, which suggests exploring UPB-like effects in systems larger than just two sites may have advantages for increasing the period of oscillations in $g_j^{(2)}(\tau)$.

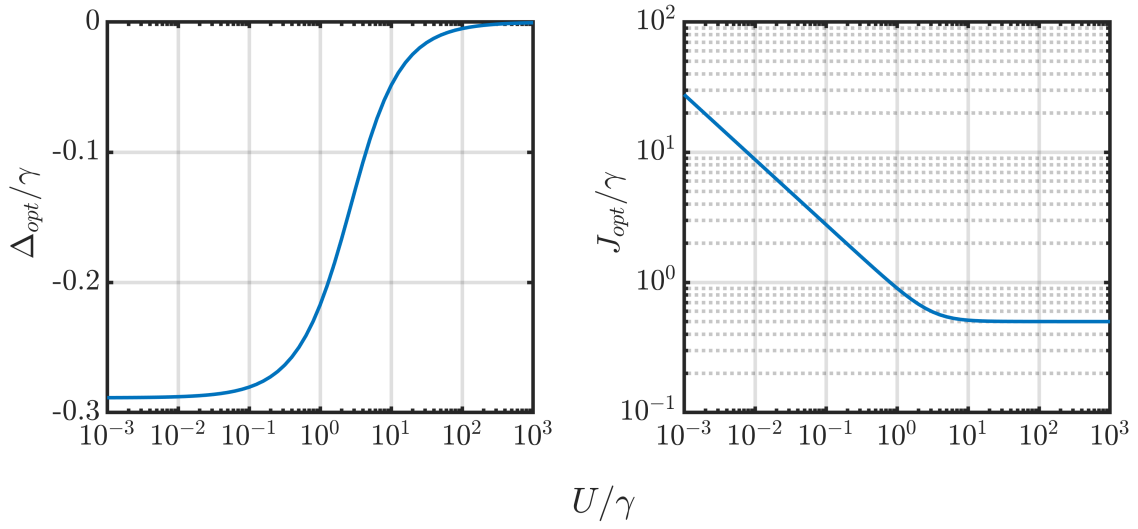

Figure 5.8: Analytical values of optimal parameters for antibunching on central site of three site DDBH chain, calculated in weak driving limit, across orders of magnitude in U. Left panel: optimal detuning Δ_{opt}. Right panel: optimal hopping strength J_{opt}.

For my positive-P simulations dedicated to this problem, I choose $U = 0.1\gamma$ as a value well within the regime of applicability of the positive-P method [3], as well as accessible to the state of the art in polariton micropillar experiments (according to discussions with experimental groups of Alberto Amo and Jacqueline Bloch). For this value of U, the above formulae give $\Delta_{opt} = -0.28\gamma$ and $J_{opt} = 2.775\gamma$. A plot of $g_j^{(2)}(\tau)$ for the optimal parameters at this value of U is given by Fig. 5.9. The correlation $g_j^{(2)}(\tau)$ is calculated from the positive-P results as

$$g_j^{(2)}(\tau) = \frac{\langle \alpha_j(t)\alpha_j(t+\tau)\beta_j(t+\tau)\beta_j(t)\rangle_{PP}}{n_j(t)n_j(t+\tau)}, \tag{5.14}$$

where the averages here are taken over the set of stochastic samples as well as over the time t within the steady state. A total of 2000 samples are used for the results presented in Fig. 5.9, as well as all subsequent numerical results I present in this chapter.

The results in Fig. 5.9 show the characteristic oscillations with τ typically seen with the UPB. Another feature that is apparent here is that a weaker external drive F results in stronger antibunching, i.e. smaller $g_2^{(2)}(0)$; for $F=\gamma$, I get $g_2^{(2)}(0)=0.271(6)$, while $F=0.5\gamma$ results in $g_2^{(2)}(0)=0.10(2)$. There is a tradeoff, however; smaller F also results in reduced occupation of the relevant site, which would make the effect more difficult to observe in experiments.

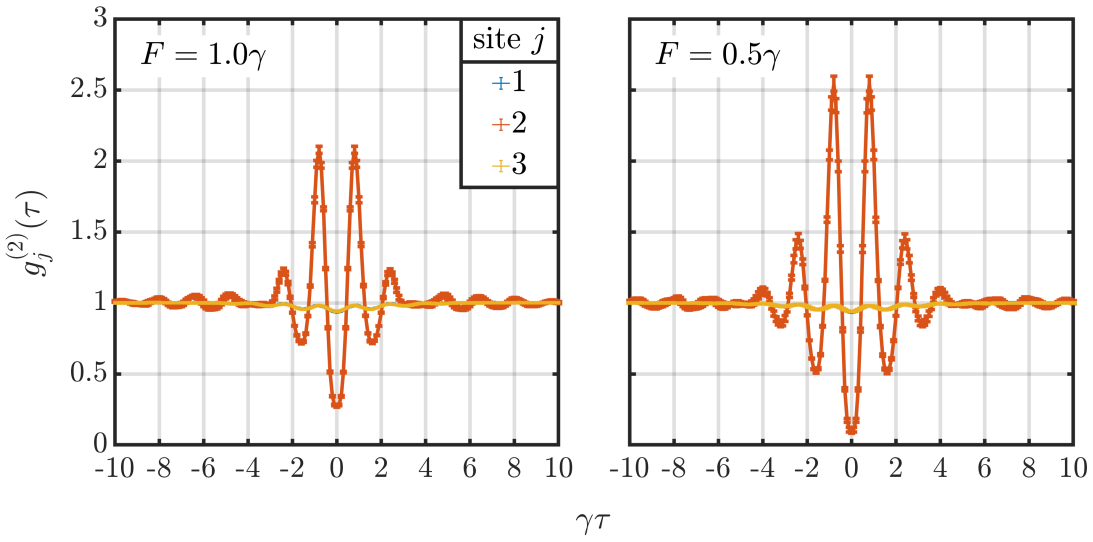

Figure 5.9: Second order correlations $g_j^{(2)}(\tau)$ using optimised parameters $\Delta=-0.28\gamma$, $U=0.1\gamma$, $J=2.775\gamma$, for two different values of the coherent drive F applied to site 1. Note that in both cases, $g_j^{(2)}(\tau)$ for sites 1 and 3 are approximately equal at all τ.

5.2.3 Exploring larger structures

I now go on to explore these effects in larger structures, to investigate if any further advantage can be obtained. The sort of analysis performed in the previous section quickly becomes unwieldy for larger lattices, so any optimisation of the physical parameters must instead be performed using the results of the positive-P simulations. Furthermore, I direct my investigations towards maximising the viability of reproducing the results in polariton micropillar experiments; this means not just finding the smallest value of $g_2^{(2)}(0)$ achiev-

able, but rather balancing the degree of antibunching against having large enough occupation and a large enough period of oscillations in $g_2^{(2)}(\tau)$ to make it possible to observe experimentally.

One possible simple example beyond the single Lieb unit cell, is the 5 site chain shown in Fig. 5.10. I label the sites in this structure as if it is a quasi-1D Lieb lattice of 2 unit cells, without the A site of the second unit cell. The choice of parameters used here are not optimised, but a minimum $g_j^{(2)}(0)$ of ≈ 0.55 is achieved on the two B sites, which are adjacent to the driven site. Compared to the results of the three site chain in Fig. 5.9, the maxima of $g_j^{(2)}(\tau)$ on either side of the central mimimum at $\tau = 0$ are much smaller, which could be a possible benefit to using a more complicated system such as this to achieve antibunching by this UPB-like effect.

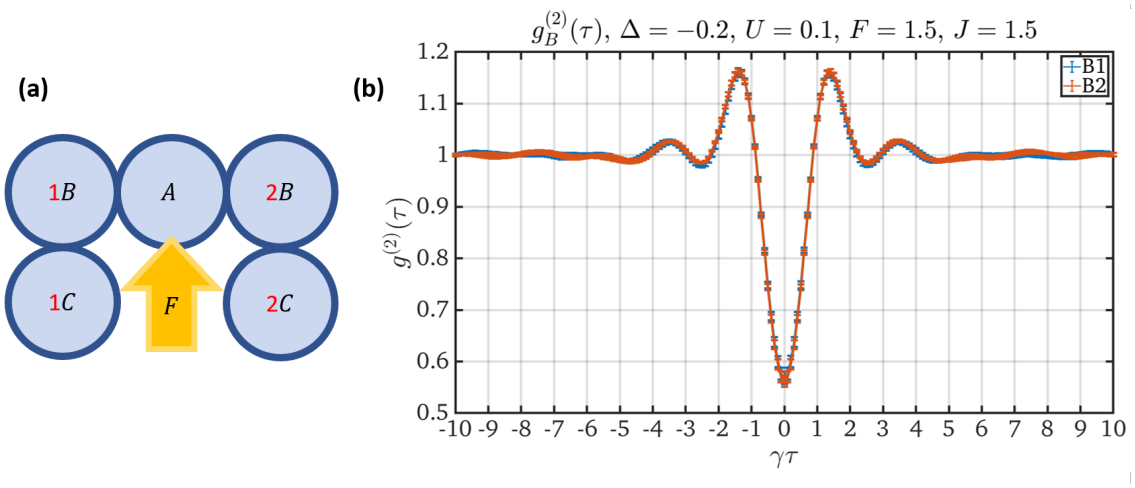

Figure 5.10: 5 site chain driven locally at central site. (a) Diagram of the structure, which I label using the conventions of the Lieb lattice. (b) Second order correlations $g_j^{(2)}(\tau)$ on the two B sites for $\Delta = -0.2\gamma$, $U = 0.1\gamma$, $J = F = 1.5\gamma$; due to the symmetry results are approximately equal on both B sites.

5.2.4 Antibunching in locally driven quasi-1D Lieb lattices

For the remainder of this chapter, I will focus on how this effect manifests in more complete Lieb lattices. In this section, I will look at how a locally driven quasi-1D DDBH Lieb lattice can be optimised for the practical observability of antibunching occurring on a particular site. A diagram of the exact structure I consider in these positive-P simulations is given in Fig. 5.11. As shown, a coherent drive is applied only to the central site $3C$ of this 5 unit cell chain.

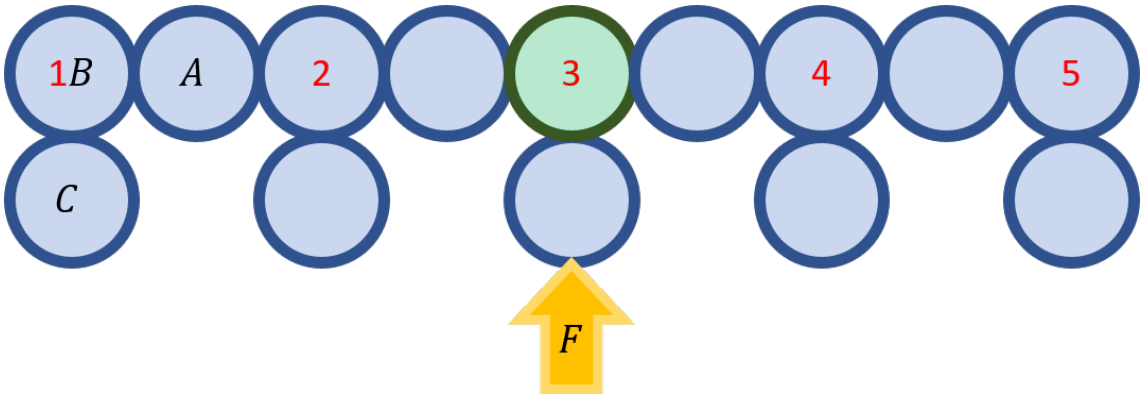

Figure 5.11: Diagram of locally driven quasi-1D Lieb lattice of 5 unit cells with smooth edges, i.e. there is no A site on the final unit cell, with open boundary conditions. Coherent drive is applied only to site $3C$. The site $3B$, highlighted in green, achieves strong antibunching in $g^{(2)}(0)$ due to interference effects.

Figure 5.12 shows the values of n and $g^{(2)}(0)$ across the lattice that result for one example set of parameters, $U = 0.1\gamma$, $\Delta = -0.2\gamma$, $F = J = 3.0\gamma$. The occupation n on each of the sublattices A, B, C appears to decay roughly exponentially with distance from the driven site. Much like in section 5.1, the B sites are "dark", with occupations typically around an order of magnitude less than their nearest C sites. The second order correlations show strong antibunching with $g^{(2)}(0) = 0.468$ on the site $3B$, which is immediately adjacent the driven site, while B sites further out display bunching, more like what is seen in section 5.1. In comparison, A and C sites merely show a very slight antibunching, ranging from almost completely coherent $g^{(2)}(0) \approx 1$ on the driven site to $g^{(2)}(0) \approx 0.8$ on the less occupied sites near the edges.

As such, in what follows I focus on the values of n and $g^{(2)}$ in the site $3B$ adjacent to the driven site $3C$. I explore how these values are affected by varying the physical parameters of the DDBH model, Δ, F, J, and U; γ is taken as the energy scale. I optimise this system by the following priorities: firstly, the aim is to minimise the value of $g^{(2)}(0)$ on site $3B$, however, the occupation of site $3B$ must also not be so small as to make it unrealistic to actually perform $g^{(2)}$ measurements of that site; I take $n > 0.1$ as a lower bound. A third possible consideration is to make the period of oscillations in $g^{(2)}(\tau)$ as large as possible, which would be achieved by making J as small as possible, without too heavily sacrificing the degree of antibunching achieved. I will show how the parameters used in Fig. 5.12 are chosen as a good compromise between all these factors.

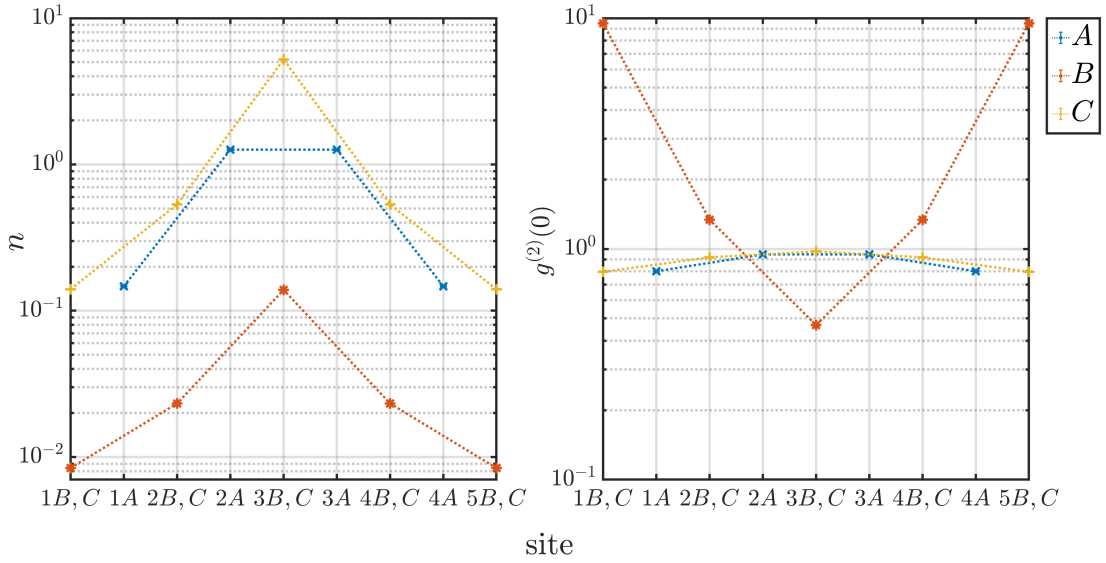

Figure 5.12: Occupation n (left panel) and second order correlation $g^{(2)}(0)$ (right panel) across quasi-1D DDBH Lieb lattice driven on site $3C$. Parameters are $U = 0.1\gamma$, $\Delta = -0.2\gamma$, $F = J = 3.0\gamma$. Values for the A sites of each unit cell are horizontally offset from those for the B and C sites, so as to reflect the spatial structure of the lattice.

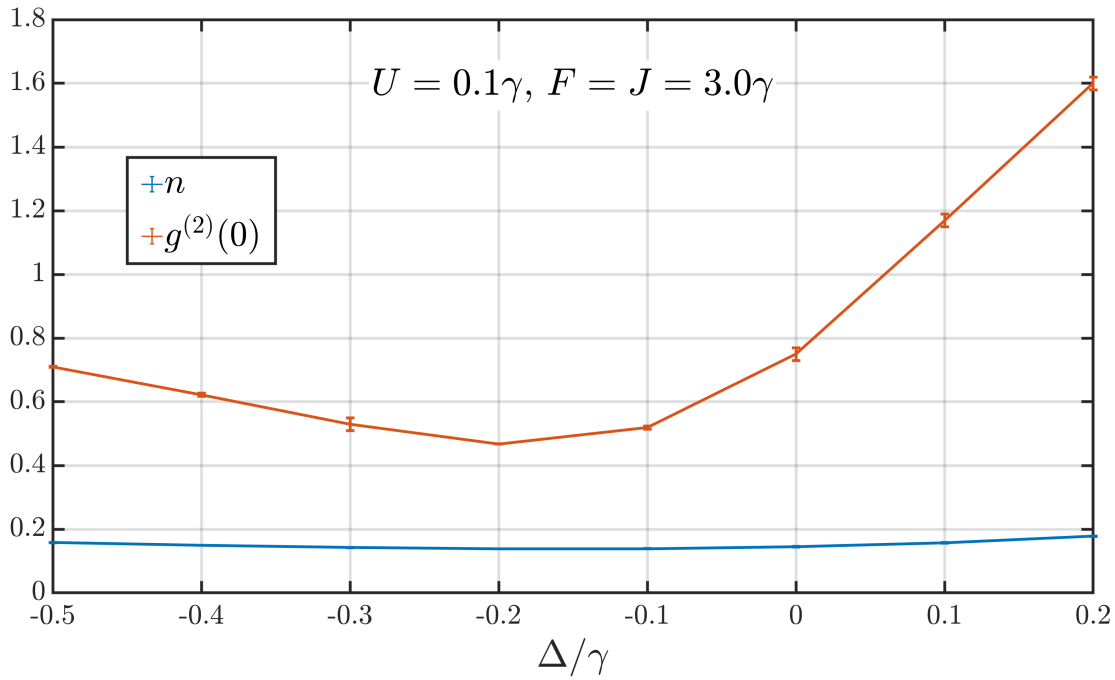

Figure 5.13: Variation in n and $g^{(2)}(0)$ of site $3B$ with Δ. Other parameters are fixed as $U = 0.1\gamma$, $F = J = 3.0\gamma$.

The first consideration is the dependence on the local energy detuning Δ, which is given in Fig. 5.13. It can be seen that for this setup, n does not depend strongly on Δ.

On the other hand, a clear minima for $g^{(2)}(0)$ is seen at around $\Delta = -0.2\gamma$. Furthermore, positive values of Δ destroy the desired effect completely by eventually switching $g^{(2)}(0)$ from antibunched $g^{(2)}(0) < 1$ to bunched $g^{(2)}(0) > 1$.

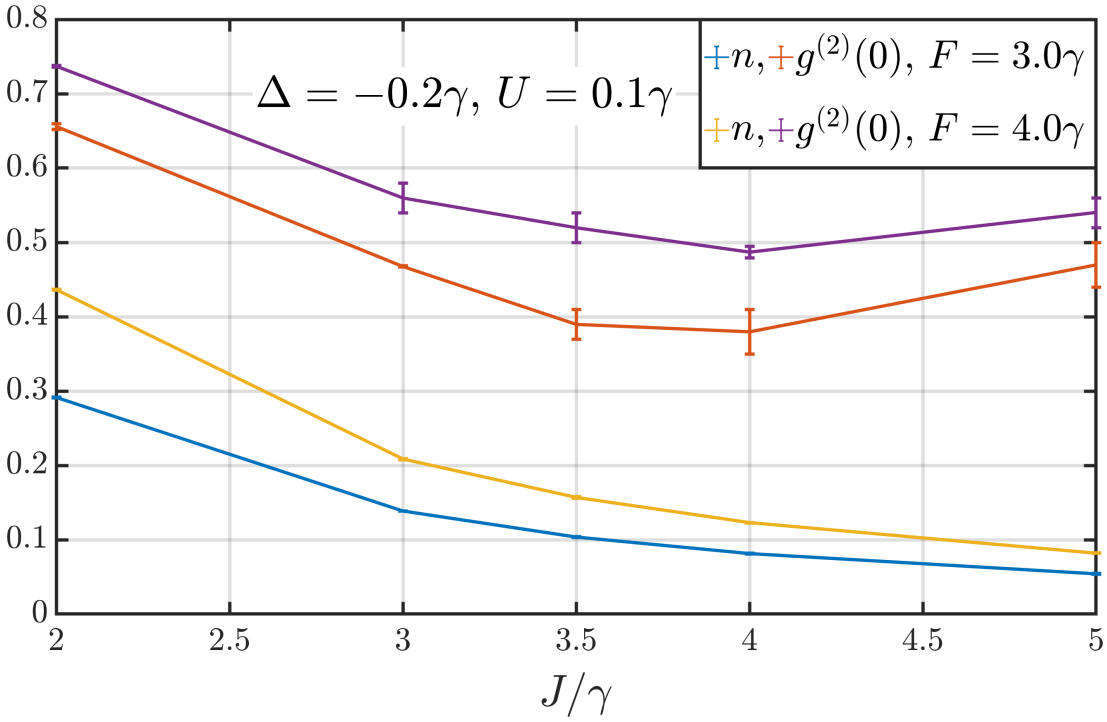

Figure 5.14: Variation in n and $g^{(2)}(0)$ of site $3B$ with J at fixed $F = 3.0\gamma$ and $F = 4.0\gamma$. Other parameters are fixed as $U = 0.1\gamma$, $\Delta = -0.2\gamma$.

Fixing to $\Delta = -0.2\gamma$, the variation with J is shown in Fig. 5.14 for both $F = 3.0\gamma$ and $F = 4.0\gamma$. $g^{(2)}(0)$ reaches a minimum at around $J = 4.0\gamma$ in both cases, although n also decreases with increasing J. Using a slightly smaller value such as $J = 3.0\gamma$ can have practical benefits of both increasing n on the relevant site as well as increasing the period of oscillations in $g^{(2)}(\tau)$.

Similar to as was demonstrated for the single unit cell in Fig. 5.9, increasing the coherent drive F while fixing the other parameters has the effect of linearly increasing both n and $g^{(2)}(0)$ of the relevant site, as shown in the left panel of Fig. 5.15. As such, F should be made as small as possible while maintaining sufficiently large n. Perhaps a more useful comparison is then given by the right panel of Fig. 5.15, where instead of only varying F, F and J are varied together keeping $F = J$ and all other parameters constant. This choice effects the value of $g^{(2)}(0)$ without significantly altering n. Here,

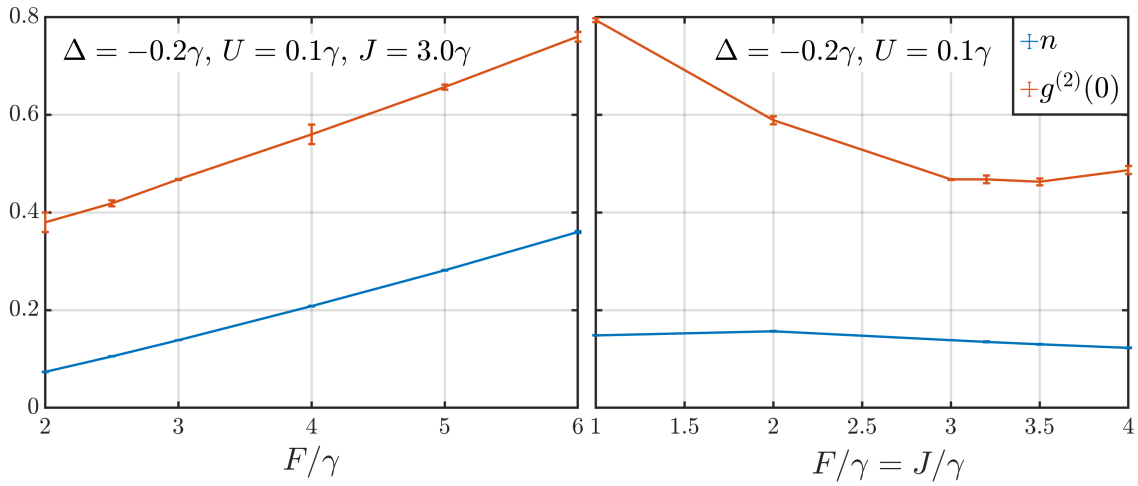

Figure 5.15: Variation in n and $g^{(2)}(0)$ of site $3B$ with drive strength F at fixed $J = 3.0\gamma$ (left panel) and when maintaining relation $F = J$ (right panel). Other parameters are fixed as $U = 0.1\gamma$, $\Delta = -0.2\gamma$.

a minimum value of $g^{(2)}(0)$ is achieved between $F = J = 3.0\gamma$ and $F = J = 3.5\gamma$, again with the smallest value of J within this range being ideal due to maximising the period of $g^{(2)}(\tau)$. Finally, in Fig. 5.16, I show that neither n nor $g^{(2)}(0)$ on site $3B$ are strongly affected by variation in the interaction strength U in this setup. This is helpful for the possibility of reproducing these results in polariton micropillar experiments, as it means there is no need to exactly match the value of $U = 0.1\gamma$ that I use here.

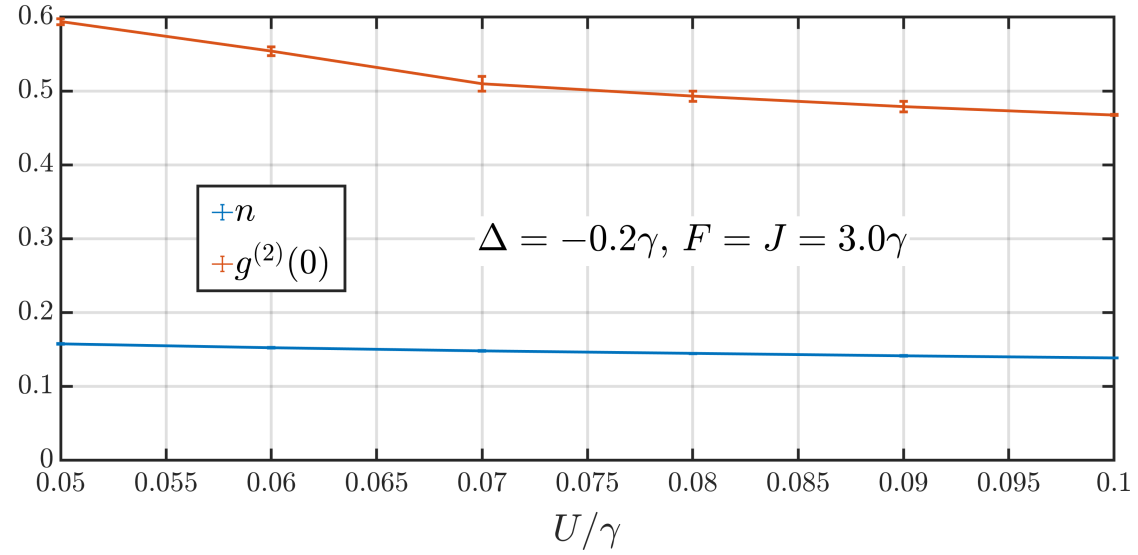

Figure 5.16: Variation in n and $g^{(2)}(0)$ of site $3B$ with U. Other parameters are fixed as $\Delta = -0.2\gamma$, $F = J = 3.0\gamma$.

As stated, from the above analysis I choose the parameters $\Delta = -0.2\gamma$, $U = 0.1\gamma$, $F = J = 3.0\gamma$, as a primary example that provides a good compromise between minimising $g^{(2)}(0)$ on site $3B$, while attempting to maintain enough occupation and a large enough period of $g^{(2)}(\tau)$ to make its observation realistic. The full form of $g^{(2)}(\tau)$ on site $3B$ with these parameters is shown in Fig. 5.17. The characteristic oscillations associated with the UPB can once again be seen, although the exact form is significantly more complicated due to the large number of sites involved. A possible advantage to this setup is that the maxima of $g^{(2)}(\tau)$ are much smaller than the traditional two site UPB, or the single unit cell example in Fig. 5.9. However, the period of the oscillations, which I measure as the gap in τ between the two maxima either side of $\tau = 0$, is still only about as long as the polariton lifetime $1/\gamma$. A useful direction of further investigation is therefore to see if there is a way to increase this period without compromising the degree of antibunching in $g^{(2)}(0)$ achieved.

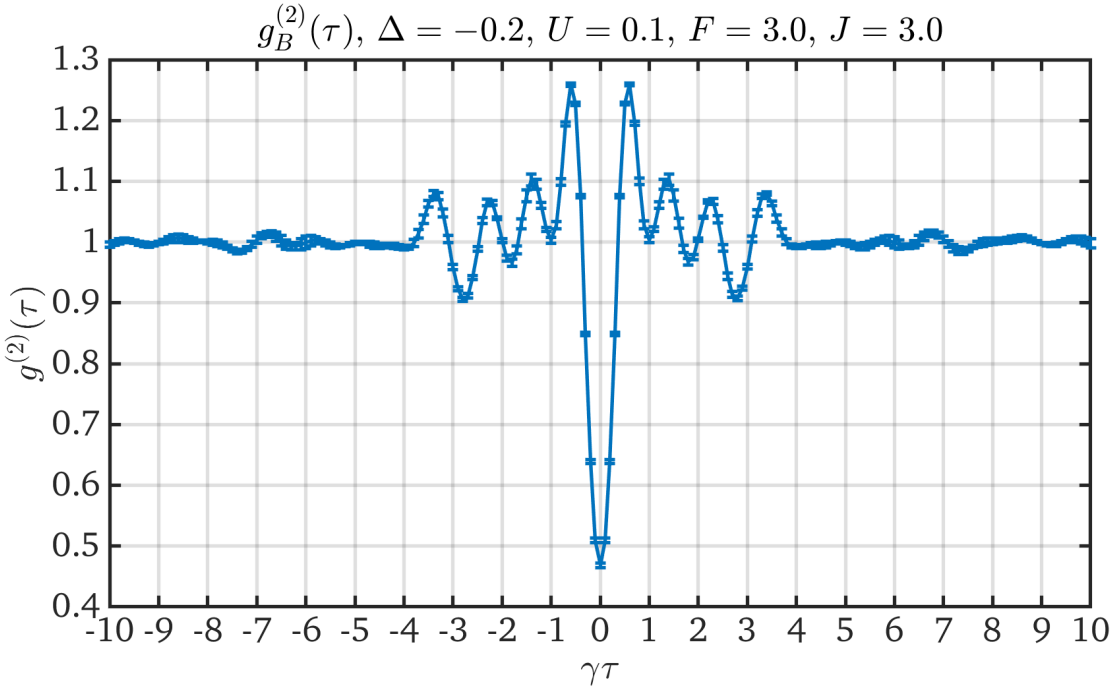

Figure 5.17: Second order temporal correlations $g^{(2)}(\tau)$ on site $3B$ of 5 unit cell quasi-1D DDBH Lieb lattice driven on site $3C$. Parameters are $U = 0.1\gamma$, $\Delta = -0.2\gamma$, $F = J = 3.0\gamma$.

5.2.5 Engineering interference with additional driving

In the two site UPB, applying a separate coherent drive to the second site, with an appropriate amplitude and phase relative to the drive on the first site, can modify the interference to allow optimal antibunching to be achieved for arbitrary values of the other parameters of the system [122, 129]. Here, I investigate how a similar principle can be applied to the quasi-1D Lieb lattice. To achieve this, I alter the scheme shown in Fig. 5.11 to include an additional coherent drive, which I refer to as the "background drive", at strength F_{bg} on all the C sites other than $3C$, which is still driven with strength F, as is shown in the diagram Fig. 5.18.

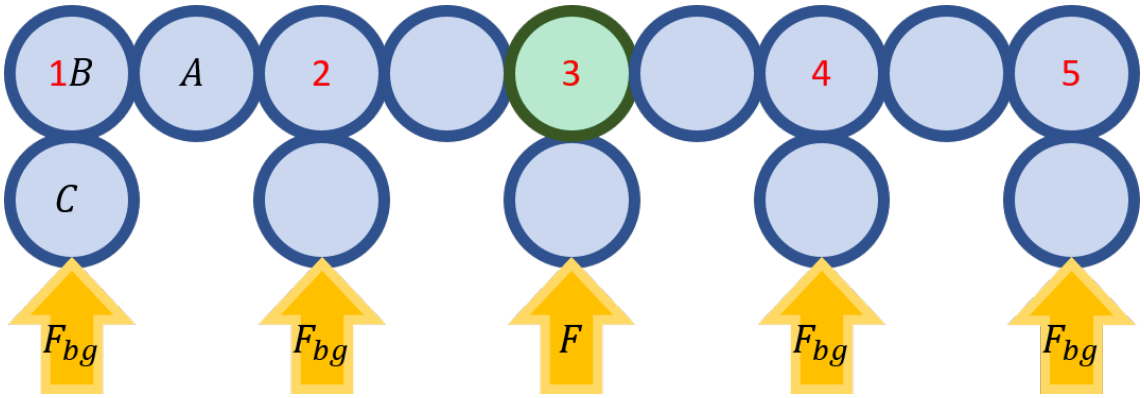

Figure 5.18: Diagram of locally driven quasi-1D lieb lattice of 5 unit cells with smooth edges, i.e. there is no A site on the final unit cell, with open boundary conditions. Coherent drive with strength F is applied only to site $3C$, while other C sites receive a coherent drive with strength F_{bg}. I once again focus on the resulting behaviour of site $3B$, highlighted in green.

The addition of this "background drive" F_{bg} allows the degree of antibunching on $3B$ to be greatly improved for parameters that were previously suboptimal. I focus on parameter values $\Delta = -0.2\gamma$, $U = 0.1\gamma$, $F = J = 1.5\gamma$, for which the variation in n and $g^{(2)}(0)$ of site $3B$ with the background drive strength F_{bg} is shown in Fig. 5.19. It can be seen that a minimum value of $g^{(2)}(0) = 0.45$, comparable to that achieved in the ideal case chosen in section 5.2.4, is reached for values of F_{bg} between 0.8γ and 0.95γ. While increasing F_{bg} does also have the effect of slowly decreasing the occupation n of $3B$, the occupation for $F_{bg} = 0.8\gamma$ is still similar to that for the example of section 5.2.4. As such, the addition of the background drive allows equivalent results for n and $g^{(2)}(0)$ to be achieved at half the value of J. I show in Fig. 5.20 that this decrease in J leads to a proportional doubling

of the period of oscillations in $g^{(2)}(\tau)$, as expected. This has the potential to be helpful for allowing this effect to be measured in experiments, as discussed earlier. In principle, even more complicated driving schemes with more independent values of the drive strength on each C site or even driving on other sites could be used to further manipulate the interference effects in the lattice.

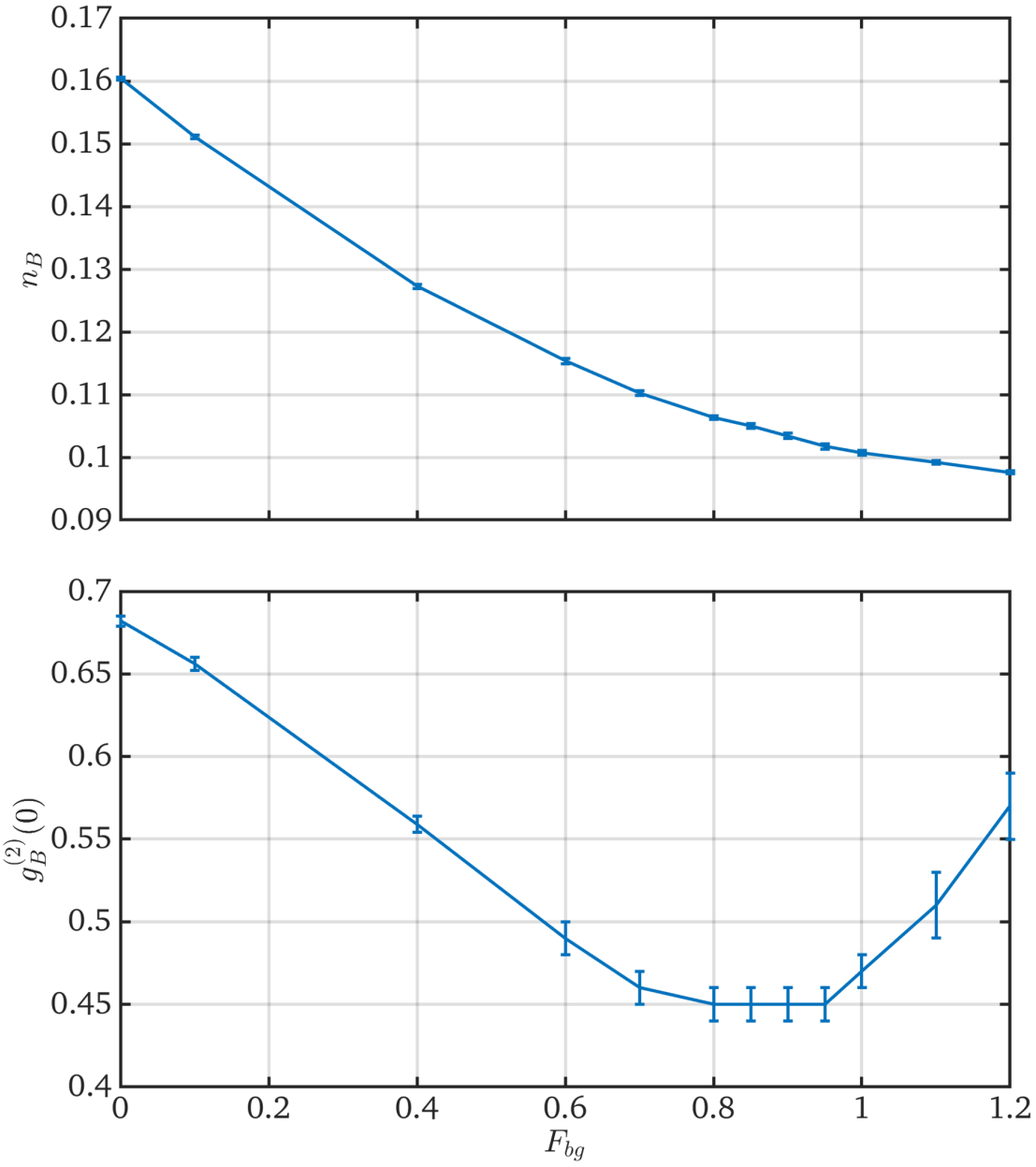

Figure 5.19: Variation in n (top) and $g^{(2)}(0)$ (bottom) of site $3B$ with the background drive strength F_{bg}. Other parameters are fixed as $\Delta = -0.2\gamma$, $U = 0.1\gamma$, $F = J = 1.5\gamma$.

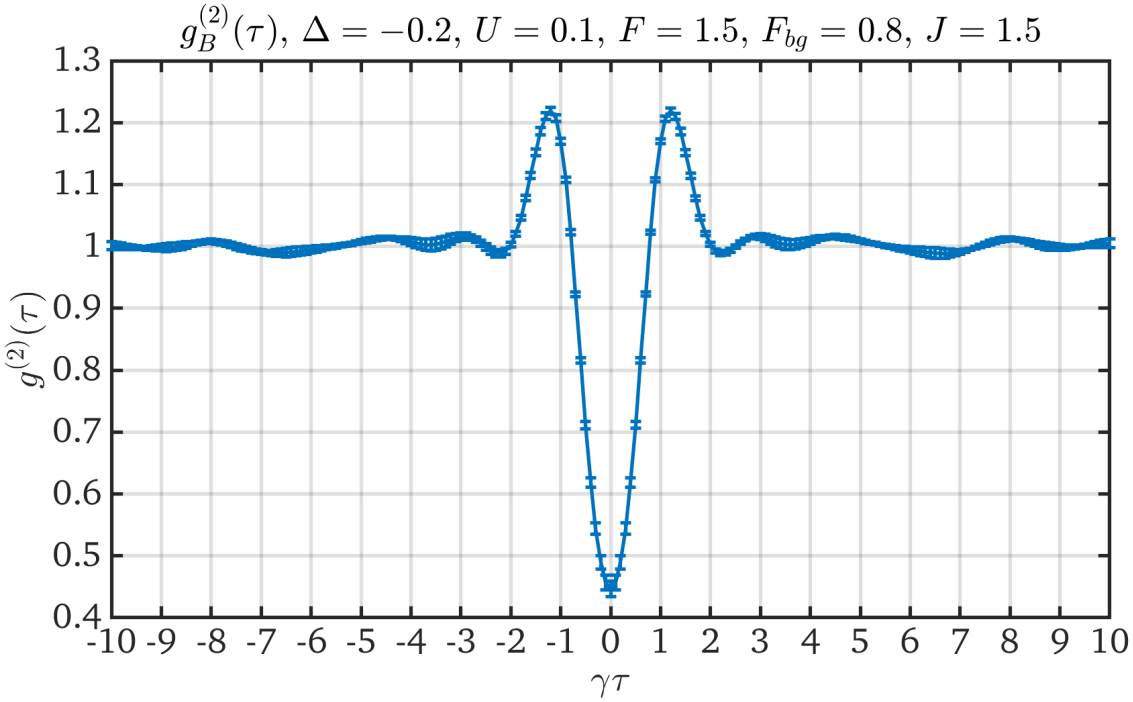

Figure 5.20: Second order temporal correlations $g^{(2)}(\tau)$ on site $3B$ of 5 unit cell quasi-1D DDBH Lieb lattice driven as shown in Fig. 5.18. Parameters are $U = 0.1\gamma$, $\Delta = -0.2\gamma$, $F = J = 1.5\gamma$, $F_{bg} = 0.8\gamma$.

5.2.6 Relation to flat band physics

An interesting further direction of investigation is to explore the relation between this UPB-like effect and the flat band physics in Lieb lattices. The single particle spectrum of the Lieb lattice has three bands, the middle of which has a flat dispersion [132, 133]. The situations considered in this chapter, where the B sites are dark compared to the A and C sites, correspond to the occupation of the flat band [4, 54, 56, 58, 59].

To see what role the flat band physics plays in this enhanced antibunching, I look at the occupation spectrum in my positive-P simulations. This is achieved by taking the discrete Fourier transform of the stochastic complex number fields $\alpha_{S,j}, \beta_{S,j}$ in space and time by

$$\tilde{\alpha}(k,\omega) = \frac{1}{NN_t}\sum_{j=1}^{N}\sum_{t=t_0}^{t_0+(N_t-1)\delta t} e^{i\omega t}\left[\left(\alpha_{C,j}+\alpha_{B,j}\right)e^{ik(j-\frac{1}{2})d}+\alpha_{A,j}e^{ikjd}\right], \tag{5.15a}$$

$$\tilde{\beta}(k,\omega) = \frac{1}{NN_t}\sum_{j=1}^{N}\sum_{t=t_0}^{t_0+(N_t-1)\delta t} e^{-i\omega t}\left[\left(\beta_{C,j}+\beta_{B,j}\right)e^{-ik(j-\frac{1}{2})d}+\beta_{A,j}e^{-ikjd}\right], \tag{5.15b}$$

where N is the number of unit cells, d is the distance between equivalent lattice sites in adjacent unit cells, i.e. twice the spacing between neighbouring sites, and $\alpha_{S,j}, \beta_{S,j}$ is sampled in time at N_t times evenly spaced by an interval δt begining at a time t_0 within the steady state. The occupation spectrum $\tilde{n}(k,\omega)$ is then calculated by averaging over stochastic realisations

$$\tilde{n}(k,\omega) = \langle \tilde{\alpha}(k,\omega)\tilde{\beta}(k,\omega)\rangle_{PP}\,. \tag{5.16}$$

To improve the resolution in k space, I consider a modification of the setup of Fig. 5.11 to include more unit cells. Instead of 5 unit cells, I instead use a chain of $N = 20$ unit cells, driven on site $11C$. Since the coherent drive is entirely localised, increasing the system size beyond a certain point should no longer noticeably affect the physics, and merely improve the k resolution. With this arrangement, I consider both the occupation spectrum $\tilde{n}(k,\omega)$ and the value of $g^{(2)}(0)$ on site $11B$.

I probe the relation between the flat band and the enhanced antibunching by looking at how altering the system so that it no longer has a flat band affects the value of $g^{(2)}(0)$ on site $11B$. One simple way to do this is to is to make the local energy detuning of the C sites Δ_C different to the local energies of the other sites in the lattice $\Delta_A = \Delta_B = \Delta$. I show in Fig. 5.21 the occupation spectra, overlayed with the calculated single particle spectra, produced in this system with $U = 0.1\gamma$, $\Delta = -0.2\gamma$, $F = J = 3.0\gamma$, for both the case with $\Delta_C = \Delta$ which exhibits a flat band, and a case with $\Delta_C = -5.0\gamma$ which transforms the flat band into a dispersive band. For $\Delta_C = \Delta$, the site $11B$ has $g^{(2)}(0) = 0.449(9)$, while $\Delta_C = -5.0\gamma$ only has $g^{(2)}(0) = 0.948(3)$.

It can therefore be seen that destroying the flat band of the Lieb lattice also has the effect of destroying the enhanced antibunching. It is probably not correct, however, to state that the enhanced antibunching in the locally driven Lieb lattice is a signature of flat band physics, since, as shown in 5.2.2, it can occur similarly in the case of a single unit cell, where it no longer makes sense to consider the system to have the band structure of a full Lieb lattice. Rather, the connection is that both the flat band and the enhanced antibunching share a common physical origin: destructive interference on the B sites of the Lieb lattice. The flat band is produced by destructive interference eliminating the occupation on the B sites, which in turn prevents bosons from moving through the lattice,

giving a flat dispersion; on the other hand, the enhanced antibunching, as in the UPB, is produced by destructive interference eliminating the probability of multiple occupation of the relevant B site.

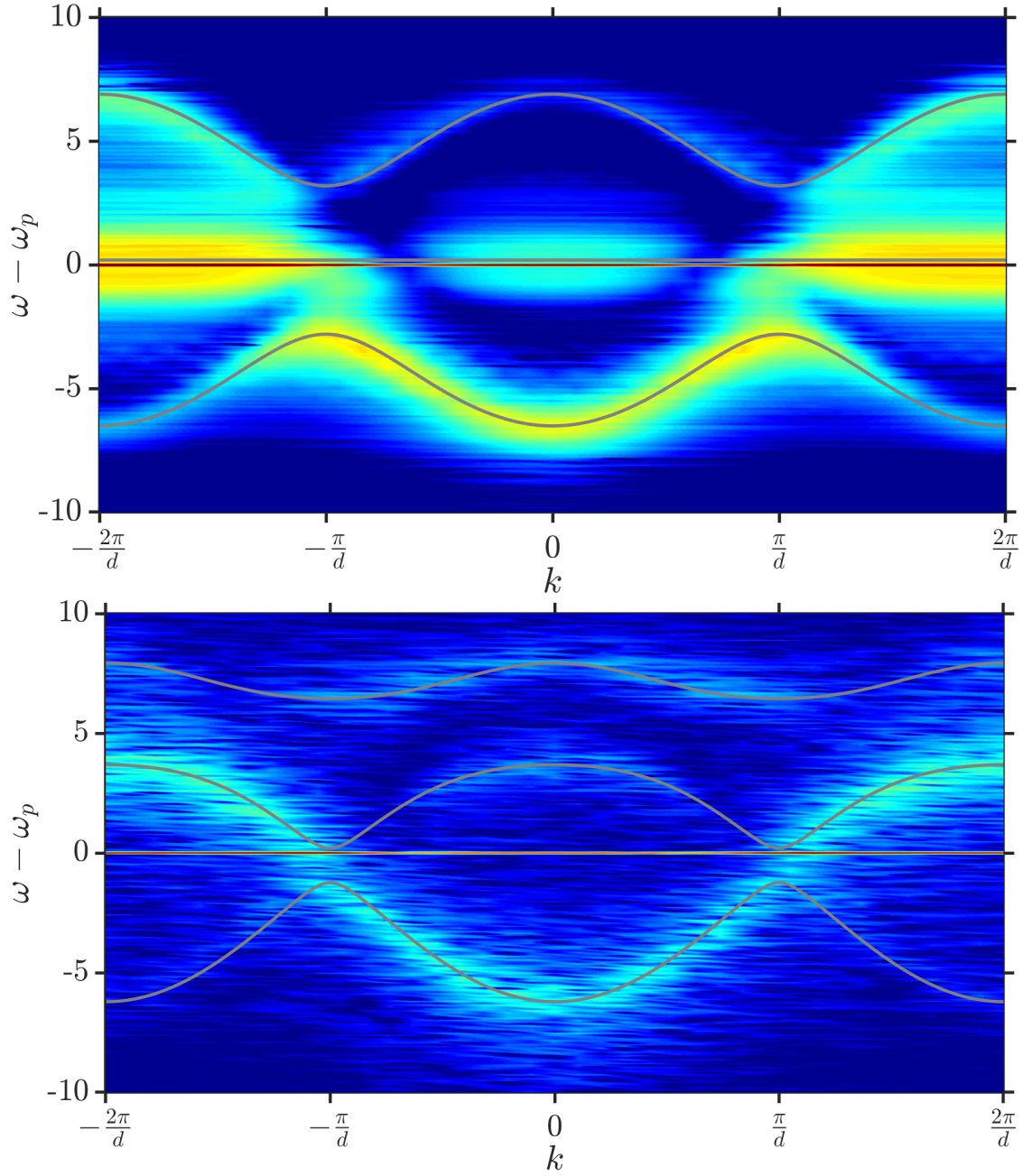

Figure 5.21: Occupation spectrum $\tilde{n}(k,\omega)$ (colour scale, arbitrary units) of 20 unit cell quasi-1D driven locally on site $11C$ for parameters $U = 0.1\gamma$, $\Delta = \Delta_A = \Delta_B = -0.2\gamma$, $F = J = 3.0\gamma$ for $\Delta_C = \Delta$ (top) and $\Delta_C = -5.0\gamma$ (bottom). Single particle spectra in both cases are shown as grey lines.

5.2.7 Enhanced antibunching in a 2D Lieb lattice

Finally, I explore if this effect of enhanced antibunching can also be implemented in 2D Lieb lattices. There is no clear practical advantage to this over the quasi-1D Lieb lattice, but I include one example here as a proof of concept. A diagram of the arrangement of the 2D Lieb lattice I model here is shown in Fig. 5.22. The system considered is a 5×5 unit cell Lieb lattice with flat edges on all sides: the right most unit cells have no A sites, while the bottom unit cells have no C sites. I focus on producing enhanced antibunching in the central most B site, in unit cell $(3,3)$ when labelling the unit cells by their location (x,y). I drive the system in a symmetrical way via the two closest C sites, i.e. $(3,3)C$ and $(3,4)C$, with a coherent drive of strength F. The values of n and $g^{(2)}(0)$ across the lattice for the parameters $U = 0.1\gamma$, $\Delta = -0.2\gamma$, $F = J = 3.0\gamma$ are shown in Fig. 5.23. With these parameters, the central B site achieves $g^{(2)}(0) = 0.65$ with an occupation of $n = 0.23$.

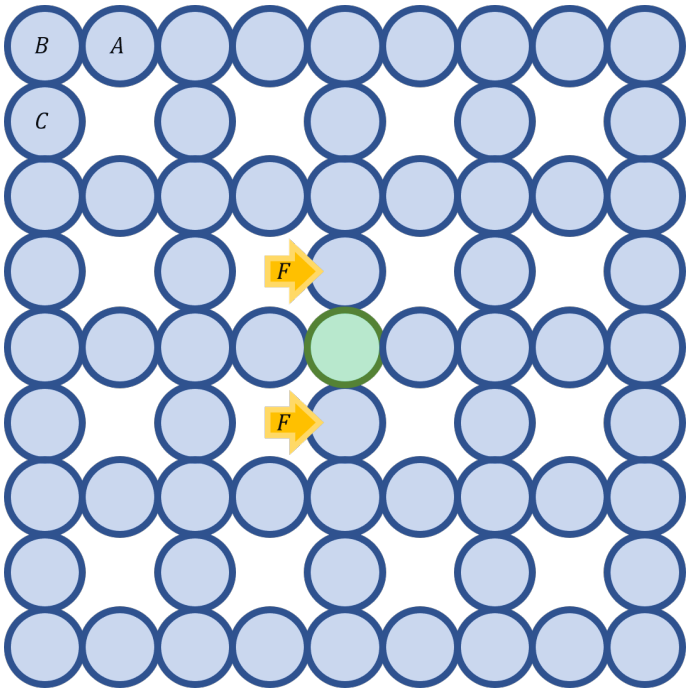

Figure 5.22: Diagram of locally driven 2D Lieb lattice of 5×5 unit cells with smooth edges and open boundary conditions. Coherent drive is applied to the two C sites nearest to the centre of the lattice, $(3,3)C$ and $(3,4)C$. The central site $(3,3)B$, highlighted in green, achieves strong antibunching in $g^{(2)}(0)$ due to interference effects.

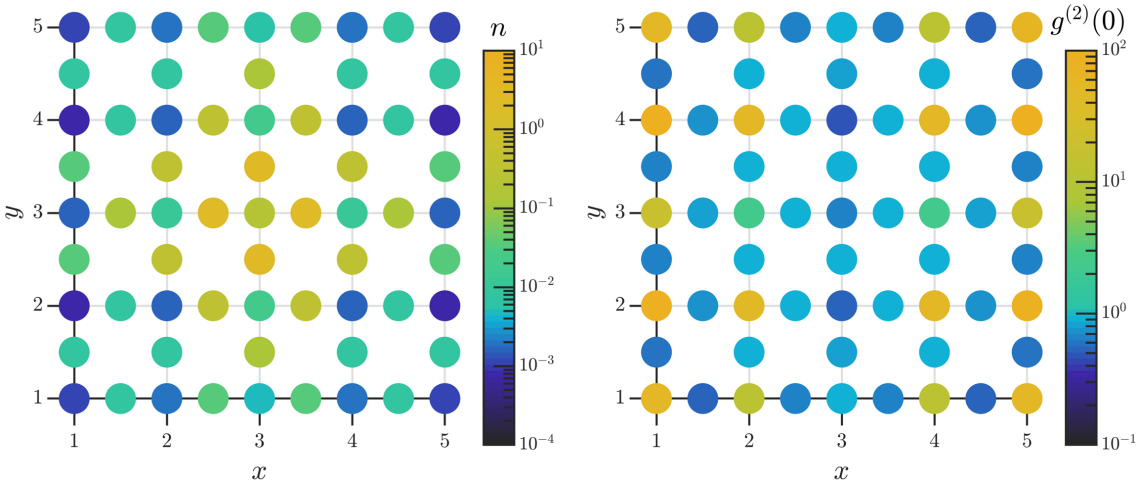

Figure 5.23: Occupation n (left panel) and second order correlation $g^{(2)}(0)$ (right panel) across 5×5 unit cell 2D DDBH Lieb lattice driven on sites $(3,3)C$ and $(3,4)C$. Parameters are $U = 0.1\gamma$, $\Delta = -0.2\gamma$, $F = J = 3.0\gamma$.

5.3 Summary and Outlook

In this chapter, I have used the positive-P method to explore various situations in which interesting correlations, as measured primarily by the local second order correlation function $g^{(2)}(0)$, can occur in DDBH Lieb lattices due to interference effects that arise under particular driving schemes. The positive-P method works well for situations with low occupations and slightly stronger interactions, where the semiclassical approximations behind the truncated Wigner method used in previous chapters break down. The two main sections of this chapter focus on opposite situations, bunching and antibunching of $g^{(2)}(0)$, that result from similar mechanisms.

In section 5.1, I used the positive-P method to reproduce the results of [4]. When driving the C sites near resonance with the on-site energy (i.e. $\Delta \approx 0$), interference of the hopping from the A and C sites eliminates the amplitude for a single boson to occupy the dark B sites, while leaving some chance for them to be occupied by multiple bosons simultaneously, producing strong bunching ($g^{(2)}(0) > 1$) on the B sites. Additionally, the positive-P method not only successfully reproduced the results of the corner space renormalization (CSR) method used in [4], but was also able to extend those results to much larger system sizes, beyond the reach of the CSR method.

Section 5.2 went on to explore how antibunching ($g^{(2)}(0) < 1$) can be produced

on one of the B sites using a localised drive on the adjacent C site. In analogy to the previously discovered unconventional photon blockade, and also similar to the mechanism of bunching in section 5.1, significant antibunching on the relevant B site results when the parameters are tuned such that interference of the hopping terms from adjacent sites eliminates the amplitude for two bosons to occupy that site, while maintaining the possibility of single boson occupation. I optimised the parameters of the model to maximise the ability to observe this effect in polariton micropillar lattices; applying additional driving terms on other sites in the lattice can also be used to modify the interference with the aim of making the optimal parameters even more ideal for this purpose. Overall, the positive-P method is found to be suitable for simulating the DDBH model in parameter regimes currently accessible to polariton micropillar experiments, and may continue to be useful for exploring a variety of situations in the context of such systems, beyond the examples covered here.

Chapter 6

Developing positive-P-like methods for coupled spin-boson systems

In this final content chapter, I will outline my efforts to extend the positive-P method from purely bosonic systems to systems with coupled spins and bosons. While this work is in its early stages, I will outline here its derivation and some simple benchmarking examples for the case of the driven-dissipative Jaynes-Cummings-Hubbard (DDJCH) model. Application of this method to more complex physical problems is beyond the scope of this thesis.

6.1 Background of positive-P for spins

As described in chapter 2, phase space methods such as positive P, in their typical formulation, rely on the mapping of quantum mechanics onto a phase space of bosonic coherent states. The extension of the positive-P method to spin systems, particularly spin-$\frac{1}{2}$ systems, therefore requires some additional effort. In previous work, adapting positive-P-like methods for spin systems typically proceeded in one of two ways.

One way is to define something similar to a coherent state for the spin variables, and use this to map onto a complex number phase space in a similar way to the bosonic positive-P kernel in (2.17), as was successfully implemented for spin chains in [134]. However, these "SU(2) coherent states" suffer from a problem inherent to the mapping from the Bloch sphere, of spin states, onto the complex plane of the phase space, in that one of the poles of the Bloch sphere must be represented by infinite values of the phase

space variables. In [134], this problem was circumvented by using a spin dependent change of variables, to always map the closest pole of the Bloch sphere to 0 as the spins evolve. However, my preliminary investigations into using this approach for spin-boson models revealed that the mapping used there does not continue to solve the problem when interactions between the spins and bosons are included. Even in one partially successful application of this approach to spin-boson systems [135], this problem was only avoided by using an unphysical regularisation, which instead introduces systematic errors.

An alternative approach is to convert the spins to additional bosonic modes, using what is known as the Schwinger boson formalism, used to apply the positive-P method to spin chains in [136]. Converting the spins into bosons in this way then allows all the modes to be treated using the usual bosonic positive-P kernels. The Schwinger boson formalism was also recently used to develop phase space methods based on truncated Wigner for spin-boson models with large spins [137]. Seemingly, the only potential issue with use the Schwinger boson formalism to handle the spins, is that it can be more complicated to represent physical initial conditions for the spins in terms of coherent states of the Schwinger bosons [136]. However, this is unlikely to be a major issue for driven dissipative problems, where initial conditions rarely play an important role. It is for this reason that I use the Schwinger boson approach in my efforts to develop a positive-P method for the DDJCH model in this chapter.

6.2 Derivations of positive-P equations for the DDJCH model

This section will outline the DDJCH model and the process by which stochastic differential equations for simulating its behaviour can be produced. Much like in chapter 2, this will proceed via the mapping of the GKSL master equation to a Fokker-Planck equation for the probability distribution over the coherent state phase space, with the additional step of the Schwinger boson mapping that allows spin terms to be treated using the usual bosonic positive-P kernels.

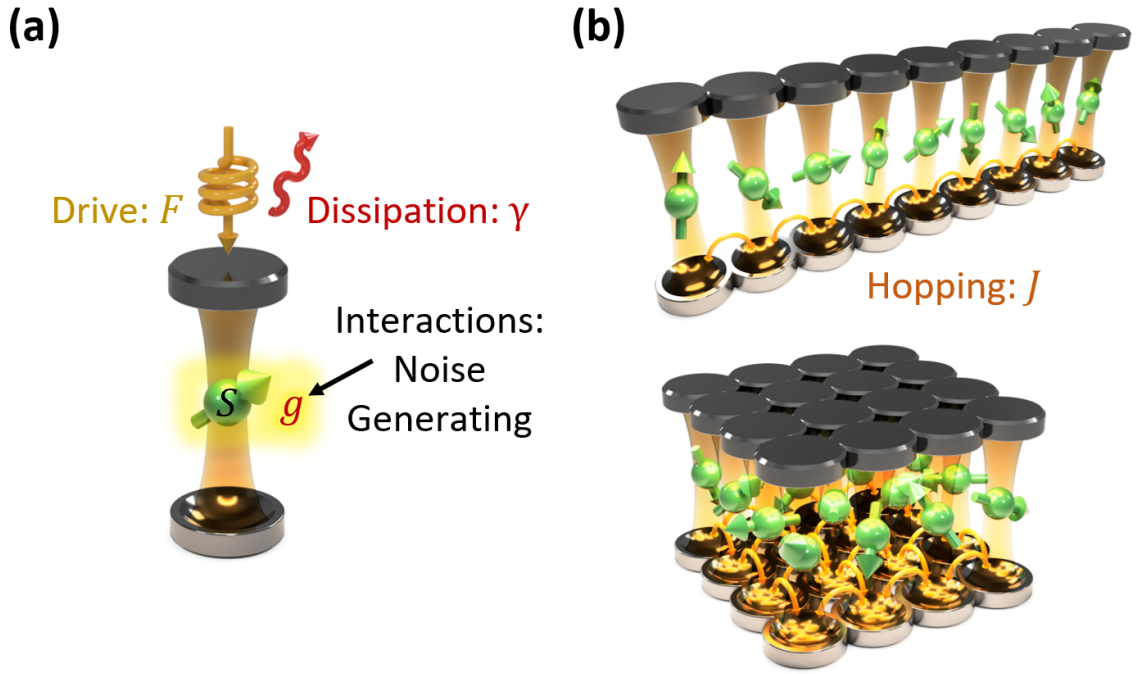

Figure 6.1: Diagrams of the DDJCH model. (a) A single site driven-dissipative Jaynes-Cummings oscillator, represented as a spin coupled with strength g to cavity photons with drive F and dissipation γ. (b) 1D and 2D DDJCH lattices, with sites connected by hopping J of the bosonic mode. 3D art courtesy of Conor McKeever.

6.2.1 The driven-dissipative Jaynes-Cummings-Hubbard model

Much like the driven-dissipative Bose-Hubbard model I have outlined in section 2.2.2 and studied in chapter 5, the driven-dissipative Jaynes-Cummings-Hubbard model can be used to describe arrays of open coupled nonlinear bosonic resonators [132, 138–143]. Here, instead of a local self-interaction of the bosons on each site, the nonlinearity is provided by the coupling of each bosonic mode to a local two-level (i.e. spin-$\frac{1}{2}$) system. A diagram of this model is given in Fig. 6.1. One natural implementation of this is with superconducting qubits in circuit QED lattices [132, 138, 141, 142].

To set up the problem, I will first define the spin operators. Any state of a single spin-$\frac{1}{2}$ can be written as a two component vector

$$\begin{pmatrix} u \\ v \end{pmatrix} \equiv u|\uparrow\rangle + v|\downarrow\rangle\,, \tag{6.1}$$

where the complex amplitudes u and v are normalised as $|u|^2 + |v|^2 = 1$, and $|\uparrow\rangle, |\downarrow\rangle$

represent the spin up and down states, respectively. Spin operators can then be defined in this notation in terms of the Pauli matrices

$$\hat{S}^X = \frac{1}{2}\sigma^X = \frac{1}{2}\begin{pmatrix} 0 & 1 \\ 1 & 0 \end{pmatrix}, \quad \hat{S}^Y = \frac{1}{2}\sigma^Y = \frac{1}{2}\begin{pmatrix} 0 & -i \\ i & 0 \end{pmatrix}, \quad \hat{S}^Z = \frac{1}{2}\sigma^Z = \frac{1}{2}\begin{pmatrix} 1 & 0 \\ 0 & -1 \end{pmatrix}. \tag{6.2}$$

Also relevant will be the spin raising and lowering operators, given respectively by

$$\hat{S}^+ = \hat{S}^X + i\hat{S}^Y = \begin{pmatrix} 0 & 1 \\ 0 & 0 \end{pmatrix}, \quad \hat{S}^- = \hat{S}^X - i\hat{S}^Y = \begin{pmatrix} 0 & 0 \\ 1 & 0 \end{pmatrix}. \tag{6.3}$$

With these definitions in mind, the Hamiltonian for the DDJCH model can be written as

$$\begin{aligned} \frac{1}{\hbar}\hat{H}_{JCH} = &\sum_j \left[-\Delta_{C,j}\hat{c}_j^\dagger \hat{c}_j - \Delta_{Z,j}\hat{S}_j^Z + g_j\left(\hat{c}_j^\dagger \hat{S}_j^- + \hat{c}_j \hat{S}_j^+\right) + F_j\hat{c}_j^\dagger + F_j^*\hat{c}_j \right] \\ &- \sum_{connected\, j,j'} \left(J_{j,j'}\hat{c}_j^\dagger \hat{c}_{j'} + J_{j,j'}^*\hat{c}_{j'}^\dagger \hat{c}_j \right), \end{aligned} \tag{6.4}$$

where $\hat{c}_j^\dagger$,$\hat{c}_j$ are the creation/annihilation operators of the actual bosons (i.e. photons, in most of the physical implementations of this model) on each site j, g_j is the local coupling strength between the spin and bosons, $\Delta_{C,j} = \omega_p - \omega_{C,j}$ is the detuning between the coherent drive energy ω_p and the local energy of the bosons $\omega_{C,j}$, and similarly $\Delta_{Z,j} = \omega_p - \omega_{Z,j}$ for the energy splitting between the spin states $\omega_{Z,j}$; F_j and $J_{j,j'}$ are coherent drive and hopping strengths, equivalently as to how they were defined for the Bose-Hubbard model (2.23). While other channels of dissipation, such as spin dephasing or spontaneous decay, could be included in the most general DDJCH model, here I will simplify to situations with only dissipation of the bosons with local rate γ_j, leading to the GKSL master equation

$$\frac{\partial\hat{\rho}}{\partial t} = -\frac{i}{\hbar}\left[\hat{H}_{JCH}, \hat{\rho}\right] + \sum_j \frac{\gamma_j}{2}\left(2\hat{c}_j\hat{\rho}\hat{c}_j^\dagger - \hat{c}_j^\dagger\hat{c}_j\hat{\rho} - \hat{\rho}\hat{c}_j^\dagger\hat{c}_j\right), \tag{6.5}$$

similar to the DDBH model.

6.2.2 Mapping to Schwinger bosons

Following the lead of [136], to proceed further in implementing the positive-P method for this sort of model, the spin operators can be mapped onto extra bosonic modes using the Schwinger boson formalism. For the spin operators relevant to (6.4), the Schwinger boson formalism maps each spin to a pair of bosonic modes as

$$\hat{S}_j^+ = \hat{a}_j^\dagger \hat{b}_j \,, \tag{6.6a}$$

$$\hat{S}_j^- = \hat{b}_j^\dagger \hat{a}_j \,, \tag{6.6b}$$

$$\hat{S}_j^Z = \frac{1}{2}\left(\hat{a}_j^\dagger \hat{a}_j - \hat{b}_j^\dagger \hat{b}_j\right) , \tag{6.6c}$$

along with the constraint

$$\hat{a}_j^\dagger \hat{a}_j + \hat{b}_j^\dagger \hat{b}_j = 1 \,. \tag{6.7}$$

Applying (6.6) to the spin terms in (6.4) converts it to a new form in terms of the three bosonic modes on each site, one representing the real bosons and two representing the spins,

$$\begin{aligned}\frac{1}{\hbar}\hat{H}_{JCH} = \sum_j \Bigg[&-\Delta_{C,j}\hat{c}_j^\dagger \hat{c}_j - \frac{\Delta_{Z,j}}{2}\left(\hat{a}_j^\dagger \hat{a}_j - \hat{b}_j^\dagger \hat{b}_j\right) + g_j\left(\hat{c}_j^\dagger \hat{b}_j^\dagger \hat{a}_j + \hat{a}_j^\dagger \hat{b}_j \hat{c}_j\right) \\ &+ F_j \hat{c}_j^\dagger + F_j^* \hat{c}_j \Bigg] - \sum_{connected\, j,j'} \left(J_{j,j'}\hat{c}_j^\dagger \hat{c}_{j'} + J_{j,j'}^* \hat{c}_{j'}^\dagger \hat{c}_j\right) ,\end{aligned} \tag{6.8}$$

which allows (6.5) to now be converted to the positive-P representation using only the usual bosonic kernels.

6.2.3 Fokker-Planck equation for the DDJCH model

As in section 2.2, the GKSL master equation will be converted to a Fokker-Planck equation for the positive-P distribution using the expression (2.17) relating the density matrix and the positive-P distribution. To clarify, in this case the kernel $\hat{\Lambda}$ can be written as

$$\hat{\Lambda}(\boldsymbol{\alpha},\boldsymbol{\beta}) = \bigotimes_{s\in\{a,b,c\},j} \hat{\Lambda}_{s,j}(\alpha_{s,j},\beta_{s,j}) \,, \quad \hat{\Lambda}_{s,j}(\alpha_{s,j},\beta_{s,j}) = \frac{|\alpha_{s,j}\rangle\langle\beta_{s,j}^*|}{\langle\beta_{s,j}^*|\alpha_{s,j}\rangle} \,, \tag{6.9}$$

since now each site j has three modes $s \in \{a,b,c\}$. The details of applying this kernel to convert (6.5) to an integral equation in the positive-P representation are given in appendix B.2. As described there, integrating by parts, assuming the boundary terms can be neglected, leads to the following Fokker-Planck equation for the positive-P distribution of the DDJCH model,

$$\begin{aligned}
\frac{\partial P(\boldsymbol{\alpha},\boldsymbol{\beta})}{\partial t} = \sum_j \Bigg\{ & -\frac{\partial}{\partial \alpha_{a,j}}\left[\left(\frac{i\Delta_{Z,j}}{2}\alpha_{a,j} - ig_j\alpha_{b,j}\alpha_{c,j}\right)P(\boldsymbol{\alpha},\boldsymbol{\beta})\right] \\
& -\frac{\partial}{\partial \alpha_{b,j}}\left[\left(-\frac{i\Delta_{Z,j}}{2}\alpha_{b,j} - ig_j\alpha_{a,j}\beta_{c,j}\right)P(\boldsymbol{\alpha},\boldsymbol{\beta})\right] \\
& -\frac{\partial}{\partial \alpha_{c,j}}\left[\left(i\Delta_{C,j}\alpha_{c,j} - ig_j\alpha_{a,j}\beta_{b,j} - iF_j - \frac{\gamma_j}{2}\alpha_{c,j} + i\sum_{j'\neq j} J_{j,j'}\alpha_{c,j'}\right)P(\boldsymbol{\alpha},\boldsymbol{\beta})\right] \\
& -\frac{\partial}{\partial \beta_{a,j}}\left[\left(-\frac{i\Delta_{Z,j}}{2}\beta_{a,j} - ig_j\beta_{b,j}\beta_{c,j}\right)P(\boldsymbol{\alpha},\boldsymbol{\beta})\right] \\
& -\frac{\partial}{\partial \beta_{b,j}}\left[\left(\frac{i\Delta_{Z,j}}{2}\beta_{b,j} - ig_j\beta_{a,j}\alpha_{c,j}\right)P(\boldsymbol{\alpha},\boldsymbol{\beta})\right] \\
& -\frac{\partial}{\partial \beta_{c,j}}\left[\left(-i\Delta_{C,j}\beta_{c,j} + ig_j\alpha_{b,j}\beta_{a,j} - iF_j^* - \frac{\gamma_j}{2}\beta_{c,j} - i\sum_{j'\neq j} J_{j,j'}^*\beta_{c,j'}\right)P(\boldsymbol{\alpha},\boldsymbol{\beta})\right] \\
& +\frac{\partial^2}{\partial \alpha_{b,j}\partial \alpha_{c,j}}\left[-ig_j\alpha_{a,j}P(\boldsymbol{\alpha},\boldsymbol{\beta})\right] + \frac{\partial^2}{\partial \beta_{b,j}\partial \beta_{c,j}}\left[ig_j\beta_{a,j}P(\boldsymbol{\alpha},\boldsymbol{\beta})\right]\Bigg\}. \qquad (6.10)
\end{aligned}$$

To get the stochastic differential equations for trajectories of this distribution, I note that, in the basis $(\alpha_{a,j},\alpha_{b,j},\alpha_{c,j},\beta_{a,j},\beta_{b,j},\beta_{c,j})$, the j components of the diffusion matrix for this Fokker-Planck equation can be written as

$$D_{j,j} = ig_j\begin{pmatrix} 0 & 0 & 0 & 0 & 0 & 0 \\ 0 & 0 & -\alpha_{a,j} & 0 & 0 & 0 \\ 0 & -\alpha_{a,j} & 0 & 0 & 0 & 0 \\ 0 & 0 & 0 & 0 & 0 & 0 \\ 0 & 0 & 0 & 0 & 0 & \beta_{a,j} \\ 0 & 0 & 0 & 0 & \beta_{a,j} & 0 \end{pmatrix}, \qquad (6.11)$$

which can be decomposed as $D = BB^T$ with

$$B_{j,j} = \sqrt{\frac{ig}{2}} \begin{pmatrix} 0 & 0 & 0 & 0 & 0 & 0 \\ 0 & -i\sqrt{-\alpha_{a,j}} & \sqrt{-\alpha_{a,j}} & 0 & 0 & 0 \\ 0 & i\sqrt{-\alpha_{a,j}} & \sqrt{-\alpha_{a,j}} & 0 & 0 & 0 \\ 0 & 0 & 0 & 0 & 0 & 0 \\ 0 & 0 & 0 & 0 & -i\sqrt{\beta_{a,j}} & \sqrt{\beta_{a,j}} \\ 0 & 0 & 0 & 0 & i\sqrt{\beta_{a,j}} & \sqrt{\beta_{a,j}} \end{pmatrix}. \tag{6.12}$$

The resulting noise terms then take the form

$$B_{j,j} \begin{pmatrix} \xi_{a,j}^{(\alpha)} \\ \xi_{b,j}^{(\alpha)} \\ \xi_{c,j}^{(\alpha)} \\ \xi_{a,j}^{(\beta)} \\ \xi_{b,j}^{(\beta)} \\ \xi_{c,j}^{(\beta)} \end{pmatrix} = \sqrt{\frac{ig}{2}} \begin{pmatrix} 0 \\ \sqrt{-\alpha_{a,j}} \left(\xi_{c,j}^{(\alpha)} - i\xi_{b,j}^{(\alpha)} \right) \\ \sqrt{-\alpha_{a,j}} \left(\xi_{c,j}^{(\alpha)} + i\xi_{b,j}^{(\alpha)} \right) \\ 0 \\ \sqrt{\beta_{a,j}} \left(\xi_{c,j}^{(\beta)} - i\xi_{b,j}^{(\beta)} \right) \\ \sqrt{\beta_{a,j}} \left(\xi_{c,j}^{(\beta)} + i\xi_{b,j}^{(\beta)} \right) \end{pmatrix}, \tag{6.13}$$

for independent real Gaussian noises with $\langle \xi_{s,j}^{(z)}(t) \xi_{s',j'}^{(z')}(t') \rangle = \delta_{z,z'} \delta_{s,s'} \delta_{j,j'} \delta(t-t')$, $\langle \xi_{s,j}^{(z)}(t) \rangle = 0$, which can then be rewritten in terms of complex Gaussian noises $\eta_j^{(z)}(t) = \frac{\xi_{c,j}^{(z)}(t) - i\xi_{b,j}^{(z)}(t)}{\sqrt{2}}$, that have moments $\langle \eta_j^{(z)}(t) \rangle = \langle \eta_j^{(z)}(t) \eta_{j'}^{(z')}(t') \rangle = 0$, and $\langle \eta_j^{(z)}(t) \eta_{j'}^{(z')*}(t') \rangle = \delta_{z,z'} \delta_{j,j'} \delta(t-t')$. This leads to a set of six coupled stochastic differential equations for each site j,

$$\frac{\partial \alpha_{a,j}}{\partial t} = \frac{i\Delta_{Z,j}}{2} \alpha_{a,j} - ig_j \alpha_{b,j} \alpha_{c,j}, \tag{6.14a}$$

$$\frac{\partial \alpha_{b,j}}{\partial t} = -\frac{i\Delta_{Z,j}}{2} \alpha_{b,j} - ig_j \alpha_{a,j} \beta_{c,j} + \sqrt{-ig\alpha_{a,j}} \eta_j^{(\alpha)}, \tag{6.14b}$$

$$\frac{\partial \alpha_{c,j}}{\partial t} = i\Delta_{C,j} \alpha_{c,j} - ig_j \alpha_{a,j} \beta_{b,j} - iF_j - \frac{\gamma_j}{2} \alpha_{c,j} + i \sum_{j' \neq j} J_{j,j'} \alpha_{c,j'} + \sqrt{-ig\alpha_{a,j}} \eta_j^{(\alpha)*}, \tag{6.14c}$$

$$\frac{\partial \beta_{a,j}}{\partial t} = -\frac{i\Delta_{Z,j}}{2}\beta_{a,j} - ig_j\beta_{b,j}\beta_{c,j}\,, \tag{6.14d}$$

$$\frac{\partial \beta_{b,j}}{\partial t} = \frac{i\Delta_{Z,j}}{2}\beta_{b,j} - ig_j\beta_{a,j}\alpha_{c,j} + \sqrt{ig\beta_{a,j}}\eta_j^{(\beta)}\,, \tag{6.14e}$$

$$\frac{\partial \beta_{c,j}}{\partial t} = -i\Delta_{C,j}\beta_{c,j} + ig_j\alpha_{b,j}\beta_{a,j} - iF_j^* - \frac{\gamma_j}{2}\beta_{c,j} - i\sum_{j'\neq j} J_{j,j'}^*\beta_{c,j'} + \sqrt{ig\beta_{a,j}}\eta_j^{(\beta)*}\,. \tag{6.14f}$$

Since the coefficents of the noises only depend on $\alpha_{a,j}$ or $\beta_{a,j}$, but only appear in the equations for the b and c modes, this guarantees that the Stratonovich correction will be zero, and so the equations (6.14) are exactly those which I solve numerically to perform positive-P simulations for this model.

When running simulations using this method, the constraint (6.7) must be taken into account with the initial conditions. Provided that (6.7) holds at $t = 0$, the Schwinger boson mapping ensures that the drift terms conserve $\langle \hat{a}_j^\dagger \hat{a}_j + \hat{b}_j^\dagger \hat{b}_j \rangle$ exactly, while the noise terms conserve it *on average*. This does consequently mean that a sufficiently large number of stochastic realisations are required not just for precision, but also so that the average $\langle \hat{a}_j^\dagger \hat{a}_j + \hat{b}_j^\dagger \hat{b}_j \rangle$ over the finite number of realisations remains close enough to 1 to maintain the correspondence between the Schwinger bosons and the spin-$\frac{1}{2}$ systems they represent.

6.3 Benchmarking examples

While a thorough characterisation of the regimes of usefulness and numerical stability of this method in the parameter space of the model, such as was performed for the DDBH model in [3], is unfortunately beyond the scope of this thesis, I provide in this section some results of simulations with this method for small systems that can also be solved by exact diagonalization. I investigate both solutions of a single site driven-dissipative Jaynes-Cummings model, and the minimal example with hopping: a homogeneous system of two coupled sites. From this point on I will drop the site arguments j from the parameters of the model Δ_C, Δ_Z, γ, g, J, and F. Once again, the Schwinger boson positive-P simulations were coded by me using XMDS2 [85], with post-processing in MATLAB. Exact diagonalisation results for comparison were provided to me by Cristóbal Lledó.

The observables I will consider are the photon occupation,

$$n(t) = \langle \alpha_{c,j}(t)\beta_{c,j}(t)\rangle_{PP,j}\,, \tag{6.15}$$

and the magnetization of the spin,

$$\langle \hat{S}^Z(t)\rangle = \frac{1}{2}\langle \alpha_{a,j}(t)\beta_{a,j}(t) - \alpha_{b,j}(t)\beta_{b,j}(t)\rangle_{PP,j}\,, \tag{6.16}$$

as a function of time, where averages $\langle ...\rangle_{PP,j}$ are over stochastic realisations and also over the sites j in the many site spatially homogeneous case. Simulations are run from initial conditions $\alpha_{b,j} = \beta_{b,j} = 1$ and $\alpha_{a,j} = \alpha_{c,j} = \beta_{a,j} = \beta_{c,j} = 0$, representing an empty cavity and approximately spin down qubits, and run up to a time $\gamma t = 100$. All examples use a total of 10000 realisations for averaging.

6.3.1 Results for a single site Jaynes-Cummings model

The results for the single site driven-dissipative Jaynes-Cummings model with $\Delta_C = -0.2\gamma$, $\Delta_Z = -0.4\gamma$, $g = 0.1\gamma$, $F = 1.5\gamma$ are shown in Fig. 6.2. At early times, there is an extremely strong agreement between the Schwinger boson positive-P and exact solutions in both the observables considered. However, for these parameters the Schwinger boson positive-P is not completely stabilised against the noise amplification catastrophe, by which the positive-P method can eventually fail at later times for systems without sufficient dissipation; this is first evidenced by spiking around $\gamma t = 60$ and has completely overwhelmed any observable results by $\gamma t = 80$.

Decreasing the drive strength to $F = 0.5\gamma$ leads to a slight increase in the useful simulation time, as is shown in Fig. 6.3. For much weaker values of the spin boson coupling, $g = 0.01\gamma$, with $F = 1.5\gamma$ once again, shown in Fig. 6.4, the simulations almost stabilise completely, with no noise amplification catastrophe being seen before $\gamma t = 100$. It should be noted, however, that the errors in $\langle \hat{S}^Z\rangle$ can still be seen to grow with time, suggesting that this simulation would not be stable indefinitely.

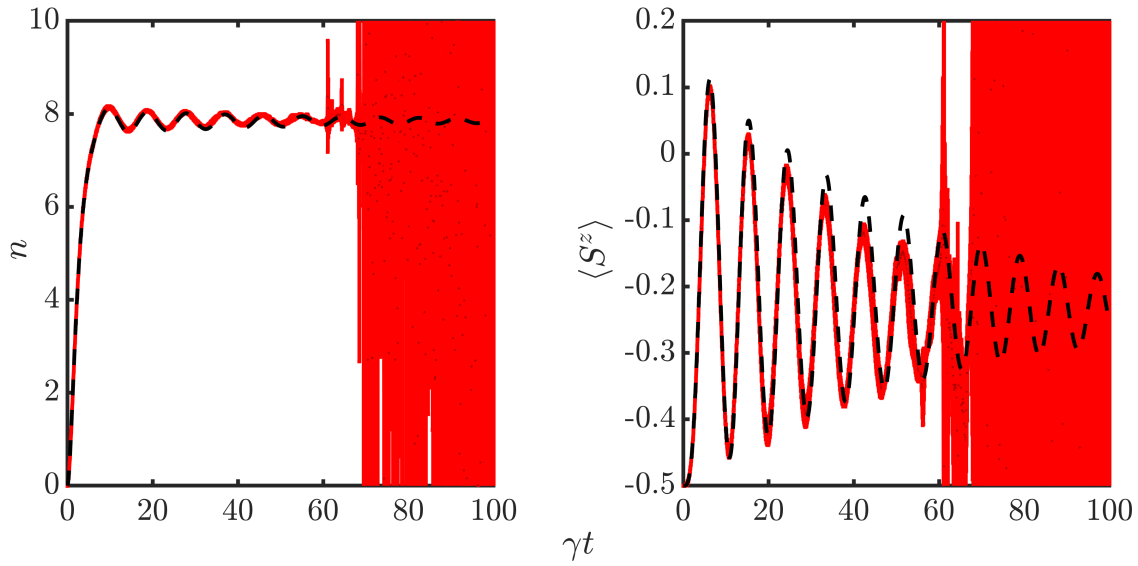

Figure 6.2: Comparison of my Schwinger boson positive-P (red) with exact results provided by Cristóbal Lledó (dashed black), for boson occupation n (left) and spin magnetization $\langle \hat{S}^Z \rangle$ in the driven-dissipative Jaynes-Cummings model. Parameters are $\Delta_C = -0.2\gamma$, $\Delta_Z = -0.4\gamma$, $g = 0.1\gamma$, and $F = 1.5\gamma$. Width of red region represents error bars.

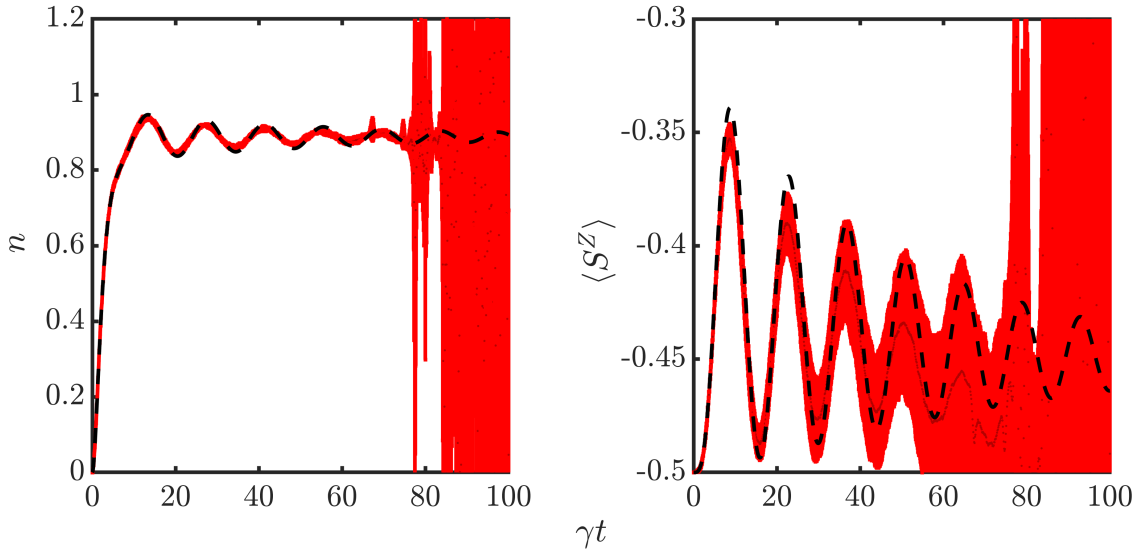

Figure 6.3: Comparison of my Schwinger boson positive-P (red) with exact results provided by Cristóbal Lledó (dashed black), for boson occupation n (left) and spin magnetization $\langle \hat{S}^Z \rangle$ in the driven-dissipative Jaynes-Cummings model. Parameters are $\Delta_C = -0.2\gamma$, $\Delta_Z = -0.4\gamma$, $g = 0.1\gamma$, and $F = 0.5\gamma$. Width of red region represents error bars.

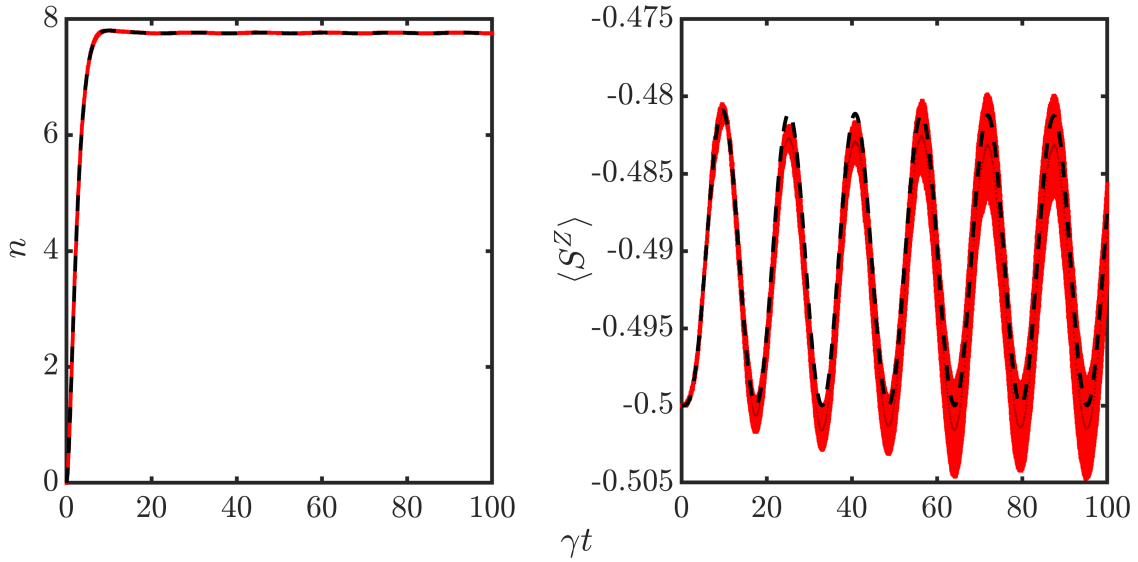

Figure 6.4: Comparison of my Schwinger boson positive-P (red) with exact results provided by Cristóbal Lledó (dashed black), for boson occupation n (left) and spin magnetization $\langle \hat{S}^Z \rangle$ in the driven-dissipative Jaynes-Cummings model. Parameters are $\Delta_C = -0.2\gamma$, $\Delta_Z = -0.4\gamma$, $g = 0.01\gamma$, and $F = 1.5\gamma$. Width of red region represents error bars.

6.3.2 DDJCH dimers

I now investigate the smallest possible example of a multi-site DDJCH model: the case of two coupled sites, also known as a dimer. I will use the same three sets of parameters as for the single site driven-dissipative Jaynes-Cummings model, with the addition of the hopping strength $J = 1.5\gamma$ in all cases.

Fig. 6.5 shows the results for parameters $\Delta_C = -0.2\gamma$, $\Delta_Z = -0.4\gamma$, $g = 0.1\gamma$, and $F = J = 1.5\gamma$. In contrast to their 1 site counterpart in Fig. 6.2, the simulations here remain stable for the entire duration to $\gamma t = 100$. This may in part be due the smaller values of n and $\langle \hat{S}^Z \rangle$, but it is also more stable than the 1 site result for $F = 0.5\gamma$ in Fig. 6.3, which has comparable values of those observables. Indeed, all three cases of the two site model, $g = 0.1\gamma$, $F = 1.5\gamma$ in Fig. 6.5, $g = 0.1\gamma$, $F = 0.5\gamma$ in Fig. 6.6, and $g = 0.01\gamma$, $F = 1.5\gamma$ in Fig. 6.7, show excellent agreement to the exact result for n. The magnetization $\langle \hat{S}^Z \rangle$ is also also stable for the simulation duration, and matches quite well to the exact value, especially at short times, but the growth in its error with time is very noticable. It is likely that the spin observables, such as $\langle \hat{S}^Z \rangle$, in the system are less numerically stable than observables of only the real bosons, such as n, since the Schwinger boson modes are not

dissipated directly, only via their coupling to the real bosonic modes.

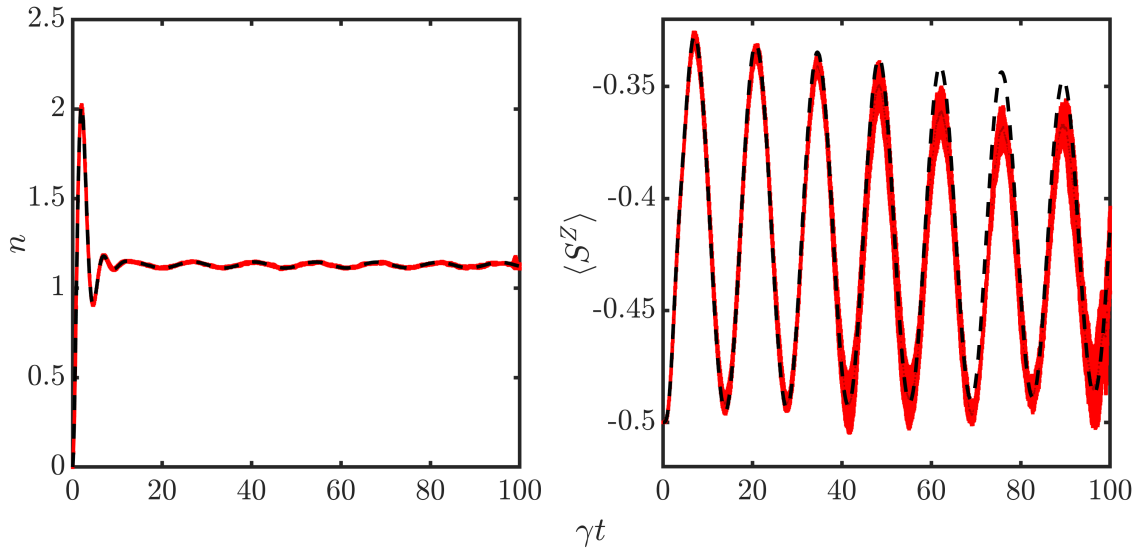

Figure 6.5: Comparison of my Schwinger boson positive-P (red) with exact results provided by Cristóbal Lledó (dashed black), for boson occupation n (left) and spin magnetization $\langle \hat{S}^Z \rangle$, averaged over both sites, in a driven-dissipative Jaynes-Cummings-Hubbard dimer. Parameters are $\Delta_C = -0.2\gamma$, $\Delta_Z = -0.4\gamma$, $g = 0.1\gamma$, and $F = J = 1.5\gamma$. Width of red region represents error bars.

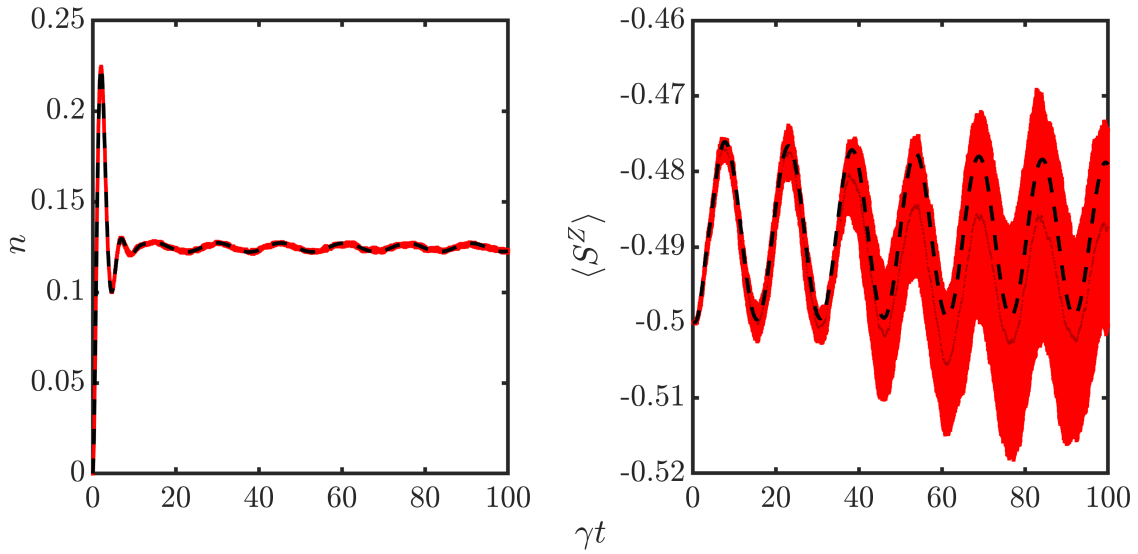

Figure 6.6: Comparison of my Schwinger boson positive-P (red) with exact results provided by Cristóbal Lledó (dashed black), for boson occupation n (left) and spin magnetization $\langle \hat{S}^Z \rangle$, averaged over both sites, in a driven-dissipative Jaynes-Cummings-Hubbard dimer. Parameters are $\Delta_C = -0.2\gamma$, $\Delta_Z = -0.4\gamma$, $g = 0.1\gamma$, $F = 0.5\gamma$, and $J = 1.5\gamma$. Width of red region represents error bars.

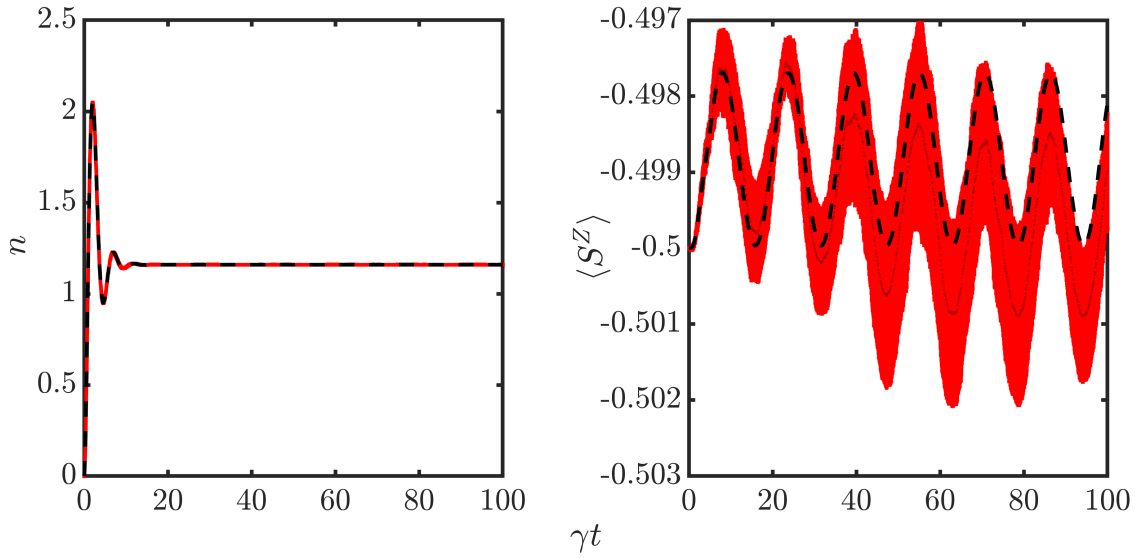

Figure 6.7: Comparison of my Schwinger boson positive-P (red) with exact results provided by Cristóbal Lledó (dashed black), for boson occupation n (left) and spin magnetization $\langle \hat{S}^Z \rangle$, averaged over both sites, in a driven-dissipative Jaynes-Cummings-Hubbard dimer. Parameters are $\Delta_C = -0.2\gamma$, $\Delta_Z = -0.4\gamma$, $g = 0.01\gamma$, and $F = J = 1.5\gamma$. Width of red region represents error bars.

6.4 Summary

Overall, the method seems to broadly work as expected, providing a good match to exact diagonalization of the master equation, at least for short times, as is to be expected from any method based on the positive-P representation. One potential issue is that the combination of noise growth in the Schwinger boson modes and the weak enforcement of the constraint (6.7) on the level of single trajectories means that, for finite numbers of stochastic realisations used, spin observables can gradually drift outside of their physically allowed values. For future work with this method, it will be important to characterise in detail if and when the simulations are able to stabilise fully. Like any phase space method, it will also be easily scalable to much larger systems than have been considered in these benchmarking examples.

Chapter 7

General Conclusions and Outlook

Through a number of separate but related projects in this thesis, I have demonstrated the power of stochastic phase space methods for simulating the behaviour of driven-dissipative many-body quantum systems, especially in the context of exciton-polaritons in semiconductor microcavities. Here, I will discuss the general conclusions of each of these projects, and their implications for future work within this field, grouped by the method used: the truncated Wigner method for semiclassical studies of polariton OPO, the positive-P method for the DDBH model, and the extension of positive-P to DDJCH models.

7.1 Truncated Wigner studies of the polariton OPO regime

The work in chapter 3 carefully characterised the various kinds of momentum distributions that appear at different strengths of the external drive between the lower and upper thresholds of the OPO regime. A particular focus was the applicability of the approximate three-mode analytical description of polariton OPO, and the relationship between the stability of analytical solutions and the actual behaviour observed in my multimode stochastic simulations. The momenta of fluctuations which maximise the instability of the pump-only solution was shown to give a good indication of how OPO forms near the thresholds: near the upper theshold where this has a single value, the momentum of the signal mode matches nearly perfectly to that value, and the three-mode description is a very good approximation for the actual behaviour; on the other hand, near the lower

threshold this maximal instability has a whole ring of equivalent values in momentum space, and consequently the signal and idler modes form as rings in momentum, which eventually collapse to a series of peaks at specific momenta as the drive strength is increased. For intermediate drive strengths, far from either threshold, OPO with significant satellite states can be seen. This behaviour breaks into two more classes, which seem to match roughly with whether or not stable solutions of the three-mode ansatz exist at that drive strength. When the three-mode ansatz has stable solutions, the satellite modes tend to be at least an order of magnitude smaller than the signal mode, and the signal momentum tends roughly, although not perfectly, towards the values that stabilise the three-mode solution. When no stable three-mode solutions exist, the satellite modes become comparable in magnitude to the signal and the three-mode description breaks down completely.

This work has important implications for any future research that relies on the three-mode analytical model of polariton OPO, as it shows it is very rarely a perfect description, outlines the conditions under which it breaks down completely, and provides a guide for what the correct choice of signal momentum is in cases where it is a good approximation. Not least of these is the following work in chapter 4, which aimed to numerically test an important prediction of the three-mode analytical model and its mapping to an anisotropic compact KPZ equation.

The work of chapter 4 was motivated as a numerical follow-up to the analytical predictions of [44], where it was shown that the mapping from the three-mode model of OPO to the KPZ equation is such that signatures of KPZ, for example the stretched exponential decay of first order spatial correlations, which are normally masked by requiring astronomically large length scales to be observable, should become visible in realistically sized microcavities for specific values of the drive strength. The results of my truncated Wigner simulations here broadly confirm the predictions of [44], via direct observation of the stretched exponential decay of first order spatial correlations which characterises the KPZ scaling phase. However, my results also highlight some of the complications that arise due to the imperfection of the three-mode analytical description of OPO, such as an alteration to the form of correlations in the direction parallel to the pump momentum and the absence of a KPZ vortex dominated phase that is thought to possibly preempt the

existence of the KPZ scaling phase.

My numerical confirmation of the observability of this signature of the KPZ universality in polariton OPO enables and encourages its reproduction by real microcavity polariton experiments in two ways. Ideally, experimentalists can simply tune the external drive to the value I use (in practice measured relative to the lower OPO threshold), and observe the same results. However, in the event that experiments should use different physical parameters to those I study here, or effects not included in my model should shift the window in drive strength slightly, my work here also offers a *prescription* of how to observe KPZ in polariton OPO:

1. Tune the drive to a value expected to be within the window for observing KPZ.

2. Observe the form of OPO that occurs and check if the resulting signal momentum analytically gives a window containing the chosen drive strength.

3. Using the previously calculated KPZ window, iterate steps 1 and 2 until a drive strength in the KPZ window for the signal momentum it produces is found.

4. Measure first order spatial correlations, and fit to identify stretched exponetial decay.

Experimental confirmation of this result in semiconductor microcavities can then in turn lead to the use of appropriately tuned polariton OPOs to study a range of effects in the 2D KPZ universality, such as the dynamics of vortices.

7.2 Positive-P simulations of polariton lattices

In [3], we both demonstrated and evaluated, as a function of the parameters of the model, the ability of the positive-P method to provide fully quantum and scalable numerical simulations of the driven-dissipative Bose-Hubbard model. While the full characterisation of the regimes of usefulness of the positive-P method across the parameter space of the 1 site model there was performed by my collaborators, the contributing and follow-up work I present in chapter 5 also provides a good demonstration of the accuracy and scalability of the positive-P method for many-site cases that possess nontrivial quantum correlations,

i.e. strong bunching or especially antibunching in the second order correlations, despite strong dissipation $\gamma > U$. The work in section 5.2, in particular, was designed specifically to maximise the ability to observe its results in actual polariton micropillar experiments.

In fact, in cannot be overstated just how ideal the positive-P method is for the parameter regimes that can be implemented currently with polariton micropillars. In this sense, the examples I chose to explore in chapter 5 are just one possible path, and the positive-P method can easily be adapted to any number of the geometries and driving schemes that have been explored by previous experiments. One interesting direction for future work, and possible experimental collaboration, would be to study the interplay between the local interactions and topological states in honeycomb lattice structures. In the long term, it would not be unexpected if the positive-P method became as ubiquitous for the study of polariton micropillar lattices, in these regimes, as the truncated Wigner method currently is for studying the semiclassical physics of polaritons in semiconductor microcavities.

7.3 Outlook for the Schwinger boson positive-P method

The work in chapter 6 represents only a first step in the process of adapting the positive-P method for models with coupled spins and bosons. While I have provided some illustrative benchmarking examples, extensive work still remains to be done in order to fully characterise how the stability of numerical simulations using this method depends on the parameters of the DDJCH model. Further work can also attempt to better optimise the method, for example alternative decompositions of the diffusion matrix may provide a different formulation of the noise terms that reduces the growth of errors in the Schwinger boson modes [144]. Should this method ultimately prove useful, it has the potential to be further adapted to include different sources of drive and/or dissipation in the DDJCH model, or even to different spin-boson models such as the Dicke model, and has the potential to be applied, in appropriate parameter regimes, to problems with qubits in coupled cavities and circuit QED. One interesting direction may be to study the effect of coupling qubits to hyperbolic lattices recently implemented in circuit QED [145], allowing for the study of the physics of open many-body quantum systems in curved space.

Appendix A

Application of Wigner operator correspondences to the lower polariton model

This appendix details the conversion of the terms in the GKSL master equation for the lower polariton model (2.8) to differential operators of the phase space variables acting on the Wigner distribution. I will outline this process separately for each of the four components of (2.8) (i.e. the three terms which make up $\hat{H}$ plus the dissipator). Firstly, for the interaction terms from $\hat{H}_{int}$, we have

$$-\frac{i}{\hbar}\left[\hat{H}_{int},\hat{\rho}\right] = -\frac{ig}{2}dV\sum_{\boldsymbol{x}}\left(\hat{\Psi}^{\dagger}(\boldsymbol{x})\hat{\Psi}^{\dagger}(\boldsymbol{x})\hat{\Psi}(\boldsymbol{x})\hat{\Psi}(\boldsymbol{x})\hat{\rho} - \hat{\rho}\hat{\Psi}^{\dagger}(\boldsymbol{x})\hat{\Psi}^{\dagger}(\boldsymbol{x})\hat{\Psi}(\boldsymbol{x})\hat{\Psi}(\boldsymbol{x})\right)$$

$$\updownarrow$$

$$-\frac{ig}{2}dV\sum_{\boldsymbol{x}}\left[\left(\Psi^{*}(\boldsymbol{x},t)-\frac{1}{2dV}\frac{\partial}{\partial\Psi(\boldsymbol{x},t)}\right)^{2}\left(\Psi(\boldsymbol{x},t)+\frac{1}{2dV}\frac{\partial}{\partial\Psi^{*}(\boldsymbol{x},t)}\right)^{2}\right.$$
$$\left.-\left(\Psi(\boldsymbol{x},t)-\frac{1}{2dV}\frac{\partial}{\partial\Psi^{*}(\boldsymbol{x},t)}\right)^{2}\left(\Psi^{*}(\boldsymbol{x},t)+\frac{1}{2dV}\frac{\partial}{\partial\Psi(\boldsymbol{x},t)}\right)^{2}\right]W$$

$$
\begin{aligned}
=&-\frac{ig}{2}dV\sum_{\boldsymbol{x}}\Bigg[-\frac{1}{dV}\frac{\partial}{\partial\Psi(\boldsymbol{x},t)}\left(\Psi^*(\boldsymbol{x},t)\Psi(\boldsymbol{x},t)^2W\right)+\frac{1}{4dV^2}\frac{\partial^2}{\partial\Psi(\boldsymbol{x},t)^2}\left(\Psi(\boldsymbol{x},t)^2W\right)\\
&+\Psi^*(\boldsymbol{x},t)^2\Psi(\boldsymbol{x},t)\frac{1}{dV}\frac{\partial W}{\partial\Psi^*(\boldsymbol{x},t)}-\Psi^*(\boldsymbol{x},t)\frac{1}{dV^2}\frac{\partial^2}{\partial\Psi(\boldsymbol{x},t)\partial\Psi^*(\boldsymbol{x},t)}\left(\Psi(\boldsymbol{x},t)W\right)\\
&+\frac{1}{4dV^3}\frac{\partial^3}{\partial\Psi(\boldsymbol{x},t)^2\partial\Psi^*(\boldsymbol{x},t)}\left(\Psi(\boldsymbol{x},t)W\right)+\Psi^*(\boldsymbol{x},t)^2\frac{1}{4dV^2}\frac{\partial^2W}{\partial\Psi^*(\boldsymbol{x},t)^2}\\
&-\Psi^*(\boldsymbol{x},t)\frac{1}{4dV^3}\frac{\partial^3W}{\partial\Psi(\boldsymbol{x},t)\partial\Psi^*(\boldsymbol{x},t)^2}+\frac{1}{dV}\frac{\partial}{\partial\Psi^*(\boldsymbol{x},t)}\left(\Psi(\boldsymbol{x},t)\Psi^*(\boldsymbol{x},t)^2W\right)\\
&-\frac{1}{4dV^2}\frac{\partial^2}{\partial\Psi^*(\boldsymbol{x},t)^2}\left(\Psi^*(\boldsymbol{x},t)^2W\right)-\frac{1}{4dV^3}\frac{\partial^3}{\partial\Psi^*(\boldsymbol{x},t)^2\partial\Psi(\boldsymbol{x},t)}\left(\Psi^*(\boldsymbol{x},t)W\right)\\
&+\Psi(\boldsymbol{x},t)\frac{1}{dV^2}\frac{\partial^2}{\partial\Psi^*(\boldsymbol{x},t)\partial\Psi(\boldsymbol{x},t)}\left(\Psi^*(\boldsymbol{x},t)W\right)-\Psi(\boldsymbol{x},t)^2\Psi^*(\boldsymbol{x},t)\frac{1}{dV}\frac{\partial W}{\partial\Psi(\boldsymbol{x},t)}\\
&-\Psi(\boldsymbol{x},t)^2\frac{1}{4dV^2}\frac{\partial^2W}{\partial\Psi(\boldsymbol{x},t)^2}+\Psi(\boldsymbol{x},t)\frac{1}{4dV^3}\frac{\partial^3W}{\partial\Psi^*(\boldsymbol{x},t)\partial\Psi(\boldsymbol{x},t)^2}\Bigg]\,,
\end{aligned}
\tag{A.1}
$$

where, here and below, the symbol $\updownarrow$ indicates the application of the operator correspondences (2.10) or (2.6), for real space and momentum space operators, respectively. We can simplify this further by rearranging the order of derivatives using

$$
\begin{aligned}
\Psi\frac{\partial W}{\partial\Psi}&=\frac{\partial}{\partial\Psi}\left(\Psi W\right)-W\,,\\
\Psi\frac{\partial^2W}{\partial\Psi^2}&=\frac{\partial^2}{\partial\Psi^2}\left(\Psi W\right)-2\frac{\partial W}{\partial\Psi}\,,\\
\Psi^2\frac{\partial W}{\partial\Psi}&=\frac{\partial}{\partial\Psi}\left(\Psi^2W\right)-2\Psi W\,,\\
\Psi^2\frac{\partial^2W}{\partial\Psi^2}&=\frac{\partial^2}{\partial\Psi^2}\left(\Psi^2W\right)-4\frac{\partial}{\partial\Psi}\left(\Psi^2W\right)+2W\,,
\end{aligned}
\tag{A.2}
$$

which when applied to (A.1) reduces it to

$$
\begin{aligned}
\sum_{\boldsymbol{x}}\Bigg[&-\frac{\partial}{\partial\Psi(\boldsymbol{x},t)}\left(-ig\left(|\Psi(\boldsymbol{x},t)|^2-\frac{1}{dV}\right)\Psi(\boldsymbol{x},t)W\right)\\
&-\frac{\partial}{\partial\Psi^*(\boldsymbol{x},t)}\left(ig\left(|\Psi(\boldsymbol{x},t)|^2-\frac{1}{dV}\right)\Psi^*(\boldsymbol{x},t)W\right)\\
&-\frac{ig}{4dV^2}\frac{\partial^2}{\partial\Psi(\boldsymbol{x},t)\partial\Psi^*(\boldsymbol{x},t)}\left(\frac{\partial}{\partial\Psi(\boldsymbol{x},t)}\left[\Psi(\boldsymbol{x},t)W\right]-\frac{\partial}{\partial\Psi^*(\boldsymbol{x},t)}\left[\Psi^*(\boldsymbol{x},t)W\right]\right)\Bigg]\,.
\end{aligned}
\tag{A.3}
$$

For the terms arising from H_{LP}, this process gives

$$
\begin{aligned}
&-\frac{i}{\hbar}\left[\hat{H}_{LP},\hat{\rho}\right] = -i\sum_{\boldsymbol{k}}\omega_{LP}(\boldsymbol{k})\left(\hat{\Psi}^{\dagger}(\boldsymbol{k})\hat{\Psi}(\boldsymbol{k})\hat{\rho}-\hat{\rho}\hat{\Psi}^{\dagger}(\boldsymbol{k})\hat{\Psi}(\boldsymbol{k})\right)\\
&\qquad\qquad\updownarrow\\
&-i\sum_{\boldsymbol{k}}\omega_{LP}(\boldsymbol{k})\left[\left(\Psi^{*}(\boldsymbol{k},t)-\frac{1}{2}\frac{\partial}{\partial\Psi(\boldsymbol{k},t)}\right)\left(\Psi(\boldsymbol{k},t)+\frac{1}{2}\frac{\partial}{\partial\Psi^{*}(\boldsymbol{k},t)}\right)\right.\\
&\left.-\left(\Psi(\boldsymbol{k},t)-\frac{1}{2}\frac{\partial}{\partial\Psi^{*}(\boldsymbol{k},t)}\right)\left(\Psi^{*}(\boldsymbol{k},t)+\frac{1}{2}\frac{\partial}{\partial\Psi(\boldsymbol{k},t)}\right)\right]W\\
&=-i\sum_{\boldsymbol{k}}\omega_{LP}(\boldsymbol{k})\left[-\frac{1}{2}\frac{\partial}{\partial\Psi(\boldsymbol{k},t)}\left(\Psi(\boldsymbol{k},t)W\right)+\frac{1}{2}\Psi^{*}(\boldsymbol{k},t)\frac{\partial W}{\partial\Psi^{*}(\boldsymbol{k},t)}\right.\\
&\left.-\frac{1}{2}\Psi(\boldsymbol{k},t)\frac{\partial W}{\partial\Psi(\boldsymbol{k},t)}+\frac{1}{2}\frac{\partial}{\partial\Psi^{*}(\boldsymbol{k},t)}\left(\Psi^{*}(\boldsymbol{k},t)W\right)\right]\\
&=\sum_{\boldsymbol{k}}\omega_{LP}(\boldsymbol{k})\left[-\frac{1}{2}\frac{\partial}{\partial\Psi(\boldsymbol{k},t)}\left(-i\Psi(\boldsymbol{k},t)W\right)-\frac{1}{2}\frac{\partial}{\partial\Psi^{*}(\boldsymbol{k},t)}\left(i\Psi^{*}(\boldsymbol{k},t)W\right)\right], \qquad \text{(A.4)}
\end{aligned}
$$

which after applying the Fourier transforms (2.9), takes the form

$$
\sum_{\boldsymbol{x}}\left[-\frac{\partial}{\partial\Psi(\boldsymbol{x},t)}\left(-i\omega_{LP}(-i\boldsymbol{\nabla})\Psi(\boldsymbol{x},t)W\right)-\frac{\partial}{\partial\Psi^{*}(\boldsymbol{x},t)}\left(i\omega_{LP}(-i\boldsymbol{\nabla})\Psi^{*}(\boldsymbol{x},t)W\right)\right], \quad \text{(A.5)}
$$

where in this process we have used that, for any function $f(\boldsymbol{k})$, $f(\boldsymbol{k})e^{i\boldsymbol{k}\cdot\boldsymbol{x}} = f(-i\boldsymbol{\nabla})e^{i\boldsymbol{k}\cdot\boldsymbol{x}}$ to convert the lower polariton dispersion $\omega_{LP}(\boldsymbol{k})$ to a differential operator in real space. Following similar steps for the dissipation terms, we have

$$
\begin{aligned}
&\kappa\sum_{\boldsymbol{k}}\left[2\hat{\Psi}(\boldsymbol{k})\hat{\rho}\hat{\Psi}^{\dagger}(\boldsymbol{k})-\hat{\Psi}^{\dagger}(\boldsymbol{k})\hat{\Psi}(\boldsymbol{k})\hat{\rho}-\hat{\rho}\hat{\Psi}^{\dagger}(\boldsymbol{k})\hat{\Psi}(\boldsymbol{k})\right]\\
&\qquad\qquad\updownarrow\\
&\kappa\sum_{\boldsymbol{k}}\left[2\left(\Psi(\boldsymbol{k},t)+\frac{1}{2}\frac{\partial}{\partial\Psi^{*}(\boldsymbol{k},t)}\right)\left(\Psi^{*}(\boldsymbol{k},t)+\frac{1}{2}\frac{\partial}{\partial\Psi(\boldsymbol{k},t)}\right)\right.\\
&\quad-\left(\Psi^{*}(\boldsymbol{k},t)-\frac{1}{2}\frac{\partial}{\partial\Psi(\boldsymbol{k},t)}\right)\left(\Psi(\boldsymbol{k},t)+\frac{1}{2}\frac{\partial}{\partial\Psi^{*}(\boldsymbol{k},t)}\right)\\
&\left.\quad-\left(\Psi(\boldsymbol{k},t)-\frac{1}{2}\frac{\partial}{\partial\Psi^{*}(\boldsymbol{k},t)}\right)\left(\Psi^{*}(\boldsymbol{k},t)+\frac{1}{2}\frac{\partial}{\partial\Psi(\boldsymbol{k},t)}\right)\right]W
\end{aligned}
$$

$$
\begin{aligned}
&= \kappa \sum_{\boldsymbol{k}} \left[\frac{\partial^2 W}{\partial \Psi(\boldsymbol{k},t) \partial \Psi^*(\boldsymbol{k},t)} + \frac{3}{2} \frac{\partial}{\partial \Psi^*(\boldsymbol{k},t)} \left(\Psi^*(\boldsymbol{k},t) W \right) - \frac{1}{2} \Psi^*(\boldsymbol{k},t) \frac{\partial W}{\partial \Psi^*(\boldsymbol{k},t)} \right. \\
&\qquad \left. + \frac{1}{2} \Psi(\boldsymbol{k},t) \frac{\partial W}{\partial \Psi(\boldsymbol{k},t)} + \frac{1}{2} \frac{\partial}{\partial \Psi(\boldsymbol{k},t)} \left(\Psi(\boldsymbol{k},t) W \right) \right] \\
&= \sum_{\boldsymbol{k}} \left[\kappa \frac{\partial^2 W}{\partial \Psi(\boldsymbol{k},t) \partial \Psi^*(\boldsymbol{k},t)} - \frac{\partial}{\partial \Psi(\boldsymbol{k},t)} \left(-\kappa \Psi(\boldsymbol{k},t) W \right) - \frac{\partial}{\partial \Psi^*(\boldsymbol{k},t)} \left(-\kappa \Psi^*(\boldsymbol{k},t) W \right) \right] \\
&= \sum_{\boldsymbol{x}} \left[\frac{\kappa}{dV} \frac{\partial^2 W}{\partial \Psi(\boldsymbol{x},t) \partial \Psi^*(\boldsymbol{x},t)} - \frac{\partial}{\partial \Psi(\boldsymbol{x},t)} \left(-\kappa \Psi(\boldsymbol{x},t) W \right) - \frac{\partial}{\partial \Psi^*(\boldsymbol{x},t)} \left(-\kappa \Psi^*(\boldsymbol{x},t) W \right) \right] .
\end{aligned}
\tag{A.6}
$$

Finally, for the terms which arise from $\hat{H}_{pump}$, we get

$$
\begin{aligned}
&-\frac{i}{\hbar} \left[\hat{H}_{pump}, \hat{\rho} \right] = \\
&-idV \sum_{\boldsymbol{x}} \left(F_p(\boldsymbol{x},t) \hat{\Psi}^\dagger(\boldsymbol{x}) \hat{\rho} + F_p^*(\boldsymbol{x},t) \hat{\Psi}(\boldsymbol{x}) \hat{\rho} - F_p(\boldsymbol{x},t) \hat{\rho} \hat{\Psi}^\dagger(\boldsymbol{x}) - F_p^*(\boldsymbol{x},t) \hat{\rho} \hat{\Psi}(\boldsymbol{x}) \right) \\
&\qquad\qquad \updownarrow \\
&-idV \sum_{\boldsymbol{x}} \left[F_p(\boldsymbol{x},t) \left(\Psi^*(\boldsymbol{x},t) - \frac{1}{2dV} \frac{\partial}{\partial \Psi(\boldsymbol{x},t)} \right) + F_p^*(\boldsymbol{x},t) \left(\Psi(\boldsymbol{x},t) + \frac{1}{2dV} \frac{\partial}{\partial \Psi^*(\boldsymbol{x},t)} \right) \right. \\
&\left. -F_p(\boldsymbol{x},t) \left(\Psi^*(\boldsymbol{x},t) + \frac{1}{2dV} \frac{\partial}{\partial \Psi(\boldsymbol{x},t)} \right) - F_p^*(\boldsymbol{x},t) \left(\Psi(\boldsymbol{x},t) - \frac{1}{2dV} \frac{\partial}{\partial \Psi^*(\boldsymbol{x},t)} \right) \right] W \\
&= \sum_{\boldsymbol{x}} - \frac{\partial}{\partial \Psi(\boldsymbol{x},t)} \left[-iF_p(\boldsymbol{x},t) W \right] - \frac{\partial}{\partial \Psi^*(\boldsymbol{x},t)} \left[iF_p^*(\boldsymbol{x},t) W \right] .
\end{aligned}
\tag{A.7}
$$

Combining all the final expressions of (A.3), (A.5), (A.6), and (A.7) together gives the evolution equation of the Wigner distribution (2.11) in the main text.

Appendix B

Positive-P formulation of driven-dissipative lattice models

This appendix is used to give all the mathematical details of the mapping of the GKSL master equations of the DDBH and DDJCH models into the positive-P representation.

B.1 Terms of the DDBH model

This section will explain the details of how the master equation of the DDBH model (2.22) is converted to the Fokker-Planck equation for the positive-P distribuiton (2.25). In equation (2.24), the master equation of the DDBH model (2.22) is expanded, using the relation (2.17) between the density operator $\hat{\rho}$, the positive-P distribution $P(\boldsymbol{\alpha},\boldsymbol{\beta})$, and the kernel $\hat{\Lambda}$, to an integral equation of quantum mechanical operators acting on $\hat{\Lambda}$. Similar to as I have done in appendix A for the truncated Wigner method, I will once again go through how each of the terms in (2.24), i.e. the dissipation terms and each of the different contributions from the Hamiltonian (2.23), convert from quantum operators to differential operators of the phase space variables, acting on the kernel $\hat{\Lambda}$, under the action of the relations (2.18) and (2.20).

Starting with the Δ_j terms, we have

$$\begin{aligned} i\Delta_j\left[\hat{a}_j^\dagger\hat{a}_j,\hat{\Lambda}\right] &= i\Delta_j\alpha_j\left(\beta_j+\frac{\partial}{\partial\alpha_j}\right)\hat{\Lambda}-i\Delta_j\beta_j\left(\alpha_j+\frac{\partial}{\partial\beta_j}\right)\hat{\Lambda} \\ &= i\Delta_j\alpha_j\frac{\partial\hat{\Lambda}}{\partial\alpha_j}-i\Delta_j\beta_j\frac{\partial\hat{\Lambda}}{\partial\beta_j}; \end{aligned} \tag{B.1}$$

for the local interactions U_j, we have

$$\begin{aligned} -\frac{iU_j}{2}\left[\hat{a}_j^\dagger\hat{a}_j^\dagger\hat{a}_j\hat{a}_j,\hat{\Lambda}\right] &= -\frac{iU_j}{2}\alpha_j^2\left(\beta_j+\frac{\partial}{\partial\alpha_j}\right)^2\hat{\Lambda}+\frac{iU_j}{2}\beta_j^2\left(\alpha_j+\frac{\partial}{\partial\beta_j}\right)^2\hat{\Lambda} \\ &= -iU_j\alpha_j^2\beta_j\frac{\partial\hat{\Lambda}}{\partial\alpha_j}+iU_j\alpha_j\beta_j^2\frac{\partial\hat{\Lambda}}{\partial\beta_j}-\frac{iU_j}{2}\alpha_j^2\frac{\partial^2\hat{\Lambda}}{\partial\alpha_j^2}+\frac{iU_j}{2}\beta_j^2\frac{\partial^2\hat{\Lambda}}{\partial\beta_j^2}; \end{aligned} \tag{B.2}$$

for the coherent driving terms F_j,

$$\begin{aligned} -i\left[F_j\hat{a}_j^\dagger+F_j^*\hat{a}_j,\hat{\Lambda}\right] &= -iF_j\left(\beta_j+\frac{\partial}{\partial\alpha_j}\right)\hat{\Lambda}-iF_j^*\alpha_j\hat{\Lambda}+iF_j\beta_j\hat{\Lambda}+iF_j^*\left(\alpha_j+\frac{\partial}{\partial\beta_j}\right)\hat{\Lambda} \\ &= -iF_j\frac{\partial\hat{\Lambda}}{\partial\alpha_j}+iF_j^*\frac{\partial\hat{\Lambda}}{\partial\beta_j}; \end{aligned} \tag{B.3}$$

for the hopping terms $J_{j,j'}$,

$$\begin{aligned} &i\left[J_{j,j'}\hat{a}_j^\dagger\hat{a}_{j'}+J_{j,j'}^*\hat{a}_{j'}^\dagger\hat{a}_j,\hat{\Lambda}\right] = \\ &iJ_{j,j'}\alpha_{j'}\left(\beta_j+\frac{\partial}{\partial\alpha_j}\right)\hat{\Lambda}+iJ_{j,j'}^*\alpha_j\left(\beta_{j'}+\frac{\partial}{\partial\alpha_{j'}}\right)\hat{\Lambda} \\ &-iJ_{j,j'}\beta_j\left(\alpha_{j'}+\frac{\partial}{\partial\beta_{j'}}\right)\hat{\Lambda}-iJ_{j,j'}^*\beta_{j'}\left(\alpha_j+\frac{\partial}{\partial\beta_j}\right)\hat{\Lambda} \\ =&iJ_{j,j'}\alpha_{j'}\frac{\partial\hat{\Lambda}}{\partial\alpha_j}-iJ_{j,j'}^*\beta_{j'}\frac{\partial\hat{\Lambda}}{\partial\beta_j}+iJ_{j,j'}^*\alpha_j\frac{\partial\hat{\Lambda}}{\partial\alpha_{j'}}-iJ_{j,j'}\beta_j\frac{\partial\hat{\Lambda}}{\partial\beta_{j'}}, \end{aligned} \tag{B.4}$$

and finally for the dissipator,

$$\begin{aligned} \frac{\gamma_j}{2}\left[2\hat{a}_j\hat{\Lambda}\hat{a}_j^\dagger-\hat{a}_j^\dagger\hat{a}_j\hat{\Lambda}-\hat{\Lambda}\hat{a}_j^\dagger\hat{a}_j\right] &= \gamma_j\alpha_j\beta_j\hat{\Lambda}-\frac{\gamma_j}{2}\alpha_j\left(\beta_j+\frac{\partial}{\partial\alpha_j}\right)\hat{\Lambda}-\frac{\gamma_j}{2}\beta_j\left(\alpha_j+\frac{\partial}{\partial\beta_j}\right)\hat{\Lambda} \\ &= -\frac{\gamma_j}{2}\alpha_j\frac{\partial\hat{\Lambda}}{\partial\alpha_j}-\frac{\gamma_j}{2}\beta_j\frac{\partial\hat{\Lambda}}{\partial\beta_j}. \end{aligned} \tag{B.5}$$

Combining these terms (B.1)-(B.5) back into the form given by (2.24) results in the following complete integral equation,

$$\begin{aligned}
&\int d^{2M}\boldsymbol{\alpha}\, d^{2M}\boldsymbol{\beta}\, \frac{\partial P(\boldsymbol{\alpha},\boldsymbol{\beta})}{\partial t}\hat{\Lambda} = \\
&\int d^{2M}\boldsymbol{\alpha}\, d^{2M}\boldsymbol{\beta}\, P(\boldsymbol{\alpha},\boldsymbol{\beta}) \sum_j \Bigg[-\frac{iU_j}{2}\alpha_j^2 \frac{\partial^2\hat{\Lambda}}{\partial\alpha_j^2} + \frac{iU_j}{2}\beta_j^2\frac{\partial^2\hat{\Lambda}}{\partial\beta_j^2} \\
&+ \left(i\Delta_j\alpha_j - iU_j\alpha_j^2\beta_j - iF_j - \frac{\gamma_j}{2}\alpha_j + i\sum_{j'\neq j} J_{j,j'}\alpha_{j'} \right)\frac{\partial\hat{\Lambda}}{\partial\alpha_j} \\
&+ \left(-i\Delta_j\beta_j + iU_j\alpha_j\beta_j^2 - iF_j^* - \frac{\gamma_j}{2}\beta_j - i\sum_{j'\neq j} J^*_{j,j'}\beta_{j'} \right)\frac{\partial\hat{\Lambda}}{\partial\beta_j} \Bigg], \qquad \text{(B.6)}
\end{aligned}$$

where the way the hopping terms are written includes the identity that $J_{j',j} \equiv J^*_{j,j'}$, so that all the terms from the second sum of (2.23) are still included.

To progress further towards an equation purely for the evolution of the probability distribution $P(\boldsymbol{\alpha},\boldsymbol{\beta})$, we must integrate by parts in order to move from differential operators acting on $\hat{\Lambda}$ to those acting on $P(\boldsymbol{\alpha},\boldsymbol{\beta})$. We assume that $P(\boldsymbol{\alpha},\boldsymbol{\beta})$ is well-behaved in the sense that $P(\boldsymbol{\alpha},\boldsymbol{\beta}) \to 0$ sufficiently fast as any $\alpha_j, \beta_j \to \infty$. As long as this assumption should remain valid, any boundary terms that would otherwise appear when performing the partial integration can be safely neglected. Under such conditions, integrating by parts converts the integral equation to the following form,

$$\begin{aligned}
&\int d^{2M}\boldsymbol{\alpha}\, d^{2M}\boldsymbol{\beta}\, \frac{\partial P(\boldsymbol{\alpha},\boldsymbol{\beta})}{\partial t}\hat{\Lambda} = \\
&\int d^{2M}\boldsymbol{\alpha}\, d^{2M}\boldsymbol{\beta}\, \hat{\Lambda} \sum_j \Bigg\{ \frac{\partial^2}{\partial\alpha_j^2}\left[-\frac{iU_j}{2}\alpha_j^2 P(\boldsymbol{\alpha},\boldsymbol{\beta}) \right] + \frac{\partial^2}{\partial\beta_j^2}\left[\frac{iU_j}{2}\beta_j^2 P(\boldsymbol{\alpha},\boldsymbol{\beta}) \right] \\
&- \frac{\partial}{\partial\alpha_j}\left[\left(i\Delta_j\alpha_j - iU_j\alpha_j^2\beta_j - iF_j - \frac{\gamma_j}{2}\alpha_j + i\sum_{j'\neq j} J_{j,j'}\alpha_{j'} \right) P(\boldsymbol{\alpha},\boldsymbol{\beta}) \right] \\
&- \frac{\partial}{\partial\beta_j}\left[\left(-i\Delta_j\beta_j + iU_j\alpha_j\beta_j^2 - iF_j^* - \frac{\gamma_j}{2}\beta_j - i\sum_{j'\neq j} J^*_{j,j'}\beta_{j'} \right) P(\boldsymbol{\alpha},\boldsymbol{\beta}) \right] \Bigg\}. \qquad \text{(B.7)}
\end{aligned}$$

Since the integrand on each side of the equation is now simply the kernel $\hat{\Lambda}$ multiplied by scalar expressions consisting of differential operators acting on $P(\boldsymbol{\alpha},\boldsymbol{\beta})$, we can use that $\mathrm{Tr}\,\hat{\Lambda} = 1$ to eliminate $\hat{\Lambda}$ by taking the trace of both sides. A trivial solution to the remaining integral equation is simply equating the integrands on each side, which gives us the Fokker-Planck equation (2.25).

B.2 Jaynes-Cummings interaction in Schwinger boson form

This section of the appendix handles the similar mapping for the master equation of the DDJCH model (6.5). Conveniently, almost all the kinds of terms that appear in the mapping of (6.5) have already been convered in the similar derivation for the DDBH model above in section B.1. For instance, the $\Delta_{C,j}$ terms, as well as the two similar Schwinger boson terms arising from $\Delta_{Z,j}$, all follow the form given by (B.1), and the coherent drive, dissipation, and hopping terms of the actual bosons are exactly as given in (B.3), (B.5), and (B.4), respectively. The one exception to this is the three operator terms that arise from the spin-boson interaction. The contribution of these to the master equation is given by

$$\begin{aligned}
&-i\left[g_j\left(\hat{c}_j^\dagger\hat{b}_j^\dagger\hat{a}_j+\hat{a}_j^\dagger\hat{b}_j\hat{c}_j\right),\hat{\Lambda}\right]= \\
&-ig_j\left[\alpha_{a,j}\left(\beta_{b,j}+\frac{\partial}{\partial\alpha_{b,j}}\right)\left(\beta_{c,j}+\frac{\partial}{\partial\alpha_{c,j}}\right)+\alpha_{b,j}\alpha_{c,j}\left(\beta_{a,j}+\frac{\partial}{\partial\alpha_{a,j}}\right)\right. \\
&\left.-\beta_{b,j}\beta_{c,j}\left(\alpha_{a,j}+\frac{\partial}{\partial\beta_{a,j}}\right)-\beta_{a,j}\left(\alpha_{b,j}+\frac{\partial}{\partial\beta_{b,j}}\right)\left(\alpha_{c,j}+\frac{\partial}{\partial\beta_{c,j}}\right)\right]\hat{\Lambda} \\
=&-ig_j\left[\alpha_{a,j}\beta_{b,j}\frac{\partial}{\partial\alpha_{c,j}}+\alpha_{a,j}\beta_{c,j}\frac{\partial}{\partial\alpha_{b,j}}+\alpha_{b,j}\alpha_{c,j}\frac{\partial}{\partial\alpha_{a,j}}+\alpha_{a,j}\frac{\partial^2}{\partial\alpha_{b,j}\partial\alpha_{c,j}}\right. \\
&\left.-\beta_{b,j}\beta_{c,j}\frac{\partial}{\partial\beta_{a,j}}-\beta_{a,j}\alpha_{c,j}\frac{\partial}{\partial\beta_{b,j}}-\beta_{a,j}\alpha_{b,j}\frac{\partial}{\partial\beta_{c,j}}-\beta_{a,j}\frac{\partial^2}{\partial\beta_{b,j}\partial\beta_{c,j}}\right]\hat{\Lambda}, \qquad \text{(B.8)}
\end{aligned}$$

which when combined with all the familiar terms gives

$$\int d^{2M}\boldsymbol{\alpha}\, d^{2M}\boldsymbol{\beta}\, \frac{\partial P(\boldsymbol{\alpha},\boldsymbol{\beta})}{\partial t}\hat{\Lambda} = \int d^{2M}\boldsymbol{\alpha}\, d^{2M}\boldsymbol{\beta}\, P(\boldsymbol{\alpha},\boldsymbol{\beta}) \sum_j$$
$$\Bigg[\left(\frac{i\Delta_{Z,j}}{2}\alpha_{a,j} - ig_j\alpha_{b,j}\alpha_{c,j}\right)\frac{\partial\hat{\Lambda}}{\partial\alpha_{a,j}} + \left(-\frac{i\Delta_{Z,j}}{2}\alpha_{b,j} - ig_j\alpha_{a,j}\beta_{c,j}\right)\frac{\partial\hat{\Lambda}}{\partial\alpha_{b,j}}$$
$$+\left(i\Delta_{C,j}\alpha_{c,j} - ig_j\alpha_{a,j}\beta_{b,j} - iF_j - \frac{\gamma_j}{2}\alpha_{c,j} + i\sum_{j'\neq j}J_{j,j'}\alpha_{c,j'}\right)\frac{\partial\hat{\Lambda}}{\partial\alpha_{c,j}}$$
$$+\left(-\frac{i\Delta_{Z,j}}{2}\beta_{a,j} - ig_j\beta_{b,j}\beta_{c,j}\right)\frac{\partial\hat{\Lambda}}{\partial\beta_{a,j}} + \left(\frac{i\Delta_{Z,j}}{2}\beta_{b,j} - ig_j\beta_{a,j}\alpha_{c,j}\right)\frac{\partial\hat{\Lambda}}{\partial\beta_{b,j}}$$
$$+\left(-i\Delta_{C,j}\beta_{c,j} + ig_j\alpha_{b,j}\beta_{a,j} - iF_j^* - \frac{\gamma_j}{2}\beta_{c,j} - i\sum_{j'\neq j}J_{j,j'}^*\beta_{c,j'}\right)\frac{\partial\hat{\Lambda}}{\partial\beta_{c,j}}$$
$$-ig_j\alpha_{a,j}\frac{\partial^2\hat{\Lambda}}{\partial\alpha_{b,j}\partial\alpha_{c,j}} + ig_j\beta_{a,j}\frac{\partial^2\hat{\Lambda}}{\partial\beta_{b,j}\partial\beta_{c,j}}\Bigg]. \tag{B.9}$$

Following the process described above for the DDBH model, that is, integration by parts (neglecting boundary terms), taking the trace to remove the kernel, and then equating the integrands on both sides, leads to the Fokker-Planck equation (6.10).

Appendix C

Analytical optimisation of 3 site unconventional photon blockade

This appendix details the analytical solution of the 3 site DDBH model in the weak driving limit, used to calculate the parameters for optimal antibunching of the central cite in section 5.2.2. The calculation proceeds as follows: first I begin by taking an ansatz for the state of the total system as a superposition of Fock states for up to two bosons distributed throughout the lattice

$$\begin{aligned}|\psi\rangle =& C_{000}|000\rangle + e^{-i\omega_p t}\left(C_{100}|100\rangle + C_{010}|010\rangle + C_{001}|001\rangle\right)\\ &+ e^{-2i\omega_p t}\left(C_{200}|200\rangle + C_{020}|020\rangle + C_{002}|002\rangle\right.\\ &\left.+ C_{110}|110\rangle + C_{101}|101\rangle + C_{011}|011\rangle\right), \end{aligned} \tag{C.1}$$

with the amplitudes obeying a hierarchy

$$C_{000} \gg C_{100}, C_{010}, C_{001} \gg C_{200}, C_{020}, C_{002}, C_{110}, C_{101}, C_{011}, \tag{C.2}$$

due to the weak driving approximation. This will be used to further approximate the density matrix $\hat{\rho}$ of the system, by keeping only up to linear order in the amplitudes other than C_{000}, leading to

$$\hat{\rho} = |\psi\rangle\langle\psi| \approx |C_{000}|^2|000\rangle\langle 000| + C^*_{000}|\psi'\rangle\langle 000| + C_{000}|000\rangle\langle\psi'|, \tag{C.3}$$

where $|\psi'\rangle = |\psi\rangle - C_{000}|000\rangle$.

I will take this approximation of $\hat{\rho}$, and substitute it into the master equation for the system. For a general DDBH lattice and in the frame of the coherent drive, this is given by (2.22) with the Hamiltonian (2.23), but for this purpose I will rewrite it in the lab frame for this specific three site chain as

$$\frac{\partial\hat{\rho}}{\partial t} = -i[\hat{H}_{3site}, \hat{\rho}] + \frac{\gamma}{2}\sum_{j=1}^{3}\left[2\hat{a}_j\hat{\rho}\hat{a}_j^\dagger - \hat{a}_j^\dagger\hat{a}_j\hat{\rho} - \hat{\rho}\hat{a}_j^\dagger\hat{a}_j\right], \tag{C.4a}$$

$$\begin{aligned}\hat{H}_{3site} = &\sum_{j=1}^{3}\left[\omega\hat{a}_j^\dagger\hat{a}_j + \frac{U}{2}\hat{a}_j^\dagger\hat{a}_j^\dagger\hat{a}_j\hat{a}_j\right] + Fe^{-i\omega_p t}\hat{a}_1^\dagger + F^* e^{i\omega_p t}\hat{a}_j \\ &+ J\left(\hat{a}_1^\dagger\hat{a}_2 + \hat{a}_2^\dagger\hat{a}_1 + \hat{a}_2^\dagger\hat{a}_3 + \hat{a}_3^\dagger\hat{a}_2\right).\end{aligned} \tag{C.4b}$$

Using (C.3) and the properties of the creation and annihilation operators, this reduces to

$$\begin{aligned}\frac{\partial C^*_{000}}{\partial t}|\psi\rangle\langle 000| + C^*_{000}\frac{\partial|\psi\rangle}{\partial t}\langle 000| &= C^*_{000}\left(-i\hat{H}_{3site}|\psi\rangle\langle 000| - \frac{\gamma}{2}\sum_{j=1}^{3}\hat{a}_j^\dagger\hat{a}_j|\psi\rangle\langle 000|\right) \\ \Rightarrow \frac{\partial C^*_{000}}{\partial t}|\psi\rangle + C^*_{000}\frac{\partial|\psi\rangle}{\partial t} &= C^*_{000}\left(-i\hat{H}_{3site}|\psi\rangle - \frac{\gamma}{2}\sum_{j=1}^{3}\hat{a}_j^\dagger\hat{a}_j|\psi\rangle\right),\end{aligned} \tag{C.5}$$

and if we consider the steady state, i.e. $\frac{\partial C_{abc}}{\partial t} = 0$ for all the amplitudes C_{abc}, then this further simplifies to

$$\frac{\partial|\psi\rangle}{\partial t} = -i\hat{H}_{3site}|\psi\rangle - \frac{\gamma}{2}\sum_{j=1}^{3}\hat{a}_j^\dagger\hat{a}_j|\psi\rangle. \tag{C.6}$$

Furthermore, in the steady state, the left hand side also can be expanded as

$$\begin{aligned}\frac{\partial|\psi\rangle}{\partial t} = &-i\omega_p e^{-i\omega_p t}\left(C_{100}|100\rangle + C_{010}|010\rangle + C_{001}|001\rangle\right) \\ &- 2i\omega_p e^{-2i\omega_p t}\left(C_{200}|200\rangle + C_{020}|020\rangle + C_{002}|002\rangle\right. \\ &\left.+ C_{110}|110\rangle + C_{101}|101\rangle + C_{011}|011\rangle\right).\end{aligned} \tag{C.7}$$

Substituting this into (C.6) and comparing the coefficients of each Fock state $|abc\rangle$, leads

to a set of nine simultaneous equations for the amplitudes C_{abc}. These are

$$-i\omega_p C_{100} = -i\omega C_{100} - iJC_{010} - iFC_{000} - \frac{\gamma}{2}C_{100}$$
$$\Rightarrow 0 = \left(-\Delta - \frac{i\gamma}{2}\right) C_{100} + JC_{010} + FC_{000}\,, \tag{C.8a}$$

$$-i\omega_p C_{010} = -i\omega C_{010} - iJC_{100} - iJC_{001} - \frac{\gamma}{2}C_{010}$$
$$\Rightarrow 0 = \left(-\Delta - \frac{i\gamma}{2}\right) C_{010} + J\left(C_{100} + C_{001}\right), \tag{C.8b}$$

$$-i\omega_p C_{001} = -i\omega C_{001} - iJC_{010} - \frac{\gamma}{2}C_{001}$$
$$\Rightarrow 0 = \left(-\Delta - \frac{i\gamma}{2}\right) C_{001} + JC_{010}\,, \tag{C.8c}$$

$$-2i\omega_p C_{200} = -2i\omega C_{200} - i\sqrt{2}JC_{110} - i\sqrt{2}FC_{100} - \gamma C_{200} - iUC_{200}$$
$$\Rightarrow 0 = 2\left(-\Delta + \frac{U}{2} - \frac{i\gamma}{2}\right) C_{200} + \sqrt{2}JC_{110} + \sqrt{2}FC_{100}\,, \tag{C.8d}$$

$$-2i\omega_p C_{020} = -2i\omega C_{020} - i\sqrt{2}JC_{110} - i\sqrt{2}JC_{011} - \gamma C_{020} - iUC_{020}$$
$$\Rightarrow 0 = 2\left(-\Delta + \frac{U}{2} - \frac{i\gamma}{2}\right) C_{020} + \sqrt{2}J\left(C_{110} + C_{011}\right), \tag{C.8e}$$

$$-2i\omega_p C_{002} = -2i\omega C_{002} - i\sqrt{2}JC_{011} - \gamma C_{002} - iUC_{002}$$
$$\Rightarrow 0 = 2\left(-\Delta + \frac{U}{2} - \frac{i\gamma}{2}\right) C_{002} + \sqrt{2}JC_{011}\,, \tag{C.8f}$$

$$-2i\omega_p C_{110} = -2i\omega C_{110} - i\sqrt{2}JC_{200} - i\sqrt{2}JC_{020} - iJC_{101} - iFC_{010} - \gamma C_{110}$$
$$\Rightarrow 0 = 2\left(-\Delta - \frac{i\gamma}{2}\right) C_{110} + J\left(C_{101} + \sqrt{2}\left[C_{200} + C_{020}\right]\right) + FC_{010}\,, \tag{C.8g}$$

$$-2i\omega_p C_{101} = -2i\omega C_{101} - iJC_{110} - iJC_{011} - iFC_{001} - \gamma C_{101}$$
$$\Rightarrow 0 = 2\left(-\Delta - \frac{i\gamma}{2}\right) C_{101} + J\left(C_{110} + C_{011}\right) + FC_{001}\,, \tag{C.8h}$$

$$-2i\omega_p C_{011} = -2i\omega C_{011} - i\sqrt{2}JC_{002} - i\sqrt{2}JC_{020} - iJC_{101} - \gamma C_{011}$$
$$\Rightarrow 0 = 2\left(-\Delta - \frac{i\gamma}{2}\right) C_{011} + J\left(C_{101} + \sqrt{2}\left[C_{002} + C_{020}\right]\right), \tag{C.8i}$$

where for the single occupation amplitudes (C.8a)-(C.8c), I have used the approximation (C.2) to neglect any dependence of these on the two boson amplitudes, and $\Delta = \omega_p - \omega$.

Rearranging (C.8c), gives

$$C_{001} = \frac{JC_{010}}{\Delta + \frac{i\gamma}{2}}, \tag{C.9}$$

which can then be substituted into (C.8b) to give

$$\begin{aligned} 0 &= \left(-\Delta - \frac{i\gamma}{2}\right) C_{010} + JC_{100} + \frac{J^2 C_{010}}{\Delta + \frac{i\gamma}{2}} \\ \Rightarrow C_{100} &= \left(\frac{\Delta + \frac{i\gamma}{2}}{J} - \frac{J}{\Delta + \frac{i\gamma}{2}}\right) C_{010}\,. \end{aligned} \tag{C.10}$$

Similarly for (C.8f),

$$C_{002} = \frac{JC_{011}}{\left(\Delta - \frac{U}{2} + \frac{i\gamma}{2}\right)\sqrt{2}}, \tag{C.11}$$

and substituting this into (C.8i) gives

$$\begin{aligned} 0 &= 2\left(-\Delta - \frac{i\gamma}{2}\right) C_{011} + JC_{101} + \sqrt{2}JC_{020} + \frac{J^2 C_{011}}{\Delta - \frac{U}{2} + \frac{i\gamma}{2}} \\ \Rightarrow C_{101} + \sqrt{2}C_{020} &= \left(\frac{2\left(\Delta + \frac{i\gamma}{2}\right)}{J} - \frac{J}{\Delta - \frac{U}{2} + \frac{i\gamma}{2}}\right) C_{011}\,. \end{aligned} \tag{C.12}$$

To obtain the parameters for optimal antibunching on the central site, $g_2^{(2)}(0) = 0$, we can proceed by setting the amplitude for double occupation of that site $C_{020} = 0$. As well as eliminating C_{020} from (C.12) above, this also reduces (C.8e) to a simple relation $C_{110} = -C_{011}$, which when substituted into (C.8h) gives

$$C_{001} = \frac{2\left(\Delta + \frac{i\gamma}{2}\right)}{F} C_{101}\,. \tag{C.13}$$

Applying (C.9) and (C.10) sequentially to this gives equations for the other two single boson amplitudes in terms of C_{101}

$$C_{010} = \frac{2\left(\Delta + \frac{i\gamma}{2}\right)^2}{JF} C_{101}\,, \tag{C.14}$$

$$C_{100} = 2\left(\frac{\left(\Delta+\frac{i\gamma}{2}\right)^3}{J^2F} - \frac{\Delta+\frac{i\gamma}{2}}{F}\right)C_{101}\,, \tag{C.15}$$

the second of which, along with (C.12) to replace $C_{110} = -C_{011}$, can be substituted into (C.8d) to give C_{200} in terms of C_{101},

$$C_{200} = \frac{1}{\sqrt{2}}\left[\frac{2\left(\Delta+\frac{i\gamma}{2}\right)^3}{J^2\left(\Delta-\frac{U}{2}+\frac{i\gamma}{2}\right)} - \frac{2\left(\Delta+\frac{i\gamma}{2}\right)}{\Delta-\frac{U}{2}+\frac{i\gamma}{2}} - \frac{J^2}{2\left(\Delta+\frac{i\gamma}{2}\right)\left(\Delta-\frac{U}{2}+\frac{i\gamma}{2}\right)-J^2}\right]C_{101}\,. \tag{C.16}$$

Finally, I use (C.8g) and, after setting $C_{020} = 0$, rewrite all other amplitudes in terms of C_{101} by substituting in the respective equations above. This leads to an equation with just the parameters of the model and C_{101},

$$\left[\frac{2J\left(\Delta+\frac{i\gamma}{2}\right)\left(\Delta-\frac{U}{2}+\frac{i\gamma}{2}\right)}{2\left(\Delta+\frac{i\gamma}{2}\right)\left(\Delta-\frac{U}{2}+\frac{i\gamma}{2}\right)-J^2} + J + \frac{2\left(\Delta+\frac{i\gamma}{2}\right)^3}{J\left(\Delta-\frac{U}{2}+\frac{i\gamma}{2}\right)} - \frac{2J\left(\Delta+\frac{i\gamma}{2}\right)}{\Delta-\frac{U}{2}+\frac{i\gamma}{2}} - \frac{J^3}{2\left(\Delta+\frac{i\gamma}{2}\right)\left(\Delta-\frac{U}{2}+\frac{i\gamma}{2}\right)-J^2} + \frac{2\left(\Delta+\frac{i\gamma}{2}\right)^2}{J}\right]C_{101} = 0\,, \tag{C.17}$$

which can be further simplified as we need $C_{101} \neq 0$, otherwise all the amplitudes will become 0, allowing C_{101} to be divided through to leave an equation relating only the physical parameters of the DDBH model. After some rearranging of terms, this takes the form

$$4\left(\Delta+\frac{i\gamma}{2}\right)^3 - U\left(\Delta+\frac{i\gamma}{2}\right)^2 - J^2U = 0\,. \tag{C.18}$$

Expanding the powers of $\left(\Delta+\frac{i\gamma}{2}\right)$, we can split this into two equations for the real and imaginary parts, as given by equations (5.11).

Bibliography

[1] K. Dunnett, A. Ferrier, A. Zamora, G. Dagvadorj, and M. H. Szymańska, Properties of the signal mode in the polariton optical parametric oscillator regime, Phys. Rev. B **98**, 165307 (2018).

[2] A. Ferrier, A. Zamora, G. Dagvadorj, and M. H. Szymańska, Searching for the Kardar-Parisi-Zhang phase in microcavity polaritons, arXiv (2020), preprint, ArXiv:2009.05177.

[3] P. Deuar, A. Ferrier, M. Matuszewski, G. Orso, and M. H. Szymańska, Fully Quantum Scalable Description of Driven-Dissipative Lattice Models, PRX Quantum **2**, 010319 (2021).

[4] W. Casteels, R. Rota, F. Storme, and C. Ciuti, Probing photon correlations in the dark sites of geometrically frustrated cavity lattices, Phys. Rev. A **93**, 043833 (2016).

[5] E. Wigner, On the Quantum Correction For Thermodynamic Equilibrium, Phys. Rev. **40**, 749 (1932).

[6] A. Polkovnikov, Phase space representation of quantum dynamics, Annals of Physics **325**, 1790 (2010).

[7] M. J. Steel, M. K. Olsen, L. I. Plimak, P. D. Drummond, S. M. Tan, M. J. Collett, D. F. Walls, and R. Graham, Dynamical quantum noise in trapped Bose-Einstein condensates, Phys. Rev. A **58**, 4824 (1998).

[8] A. Sinatra, C. Lobo, and Y. Castin, The truncated Wigner method for Bose-

condensed gases: limits of validity and applications, Journal of Physics B: Atomic, Molecular and Optical Physics **35**, 3599 (2002).

[9] A. A. Norrie, R. J. Ballagh, and C. W. Gardiner, Quantum Turbulence in Condensate Collisions: An Application of the Classical Field Method, Phys. Rev. Lett. **94**, 040401 (2005).

[10] S. E. Hoffmann, J. F. Corney, and P. D. Drummond, Hybrid phase-space simulation method for interacting Bose fields, Phys. Rev. A **78**, 013622 (2008).

[11] P. Deuar, Simulation of Complete Many-Body Quantum Dynamics Using Controlled Quantum-Semiclassical Hybrids, Phys. Rev. Lett. **103**, 130402 (2009).

[12] A. D. Martin and J. Ruostekoski, Quantum and Thermal Effects of Dark Solitons in a One-Dimensional Bose Gas, Phys. Rev. Lett. **104**, 194102 (2010).

[13] P. Deuar and P. D. Drummond, Correlations in a BEC Collision: First-Principles Quantum Dynamics with 150 000 Atoms, Phys. Rev. Lett. **98**, 120402 (2007).

[14] K. V. Kheruntsyan, J.-C. Jaskula, P. Deuar, M. Bonneau, G. B. Partridge, J. Ruaudel, R. Lopes, D. Boiron, and C. I. Westbrook, Violation of the Cauchy-Schwarz Inequality with Matter Waves, Phys. Rev. Lett. **108**, 260401 (2012).

[15] R. J. Lewis-Swan and K. V. Kheruntsyan, Proposal for demonstrating the Hong–Ou–Mandel effect with matter waves, Nature Commun. **5**, 3752 (2014).

[16] A. V. Kavokin, J. J. Baumberg, G. Malpuech, and F. P. Laussy, *Microcavities* (Oxford University Press, 2007).

[17] H. Deng, H. Haug, and Y. Yamamoto, Exciton-polariton Bose-Einstein condensation, Rev. Mod. Phys. **82**, 1489 (2010).

[18] I. Carusotto and C. Ciuti, Quantum fluids of light, Rev. Mod. Phys. **85**, 299 (2013).

[19] J. J. Hopfield, Theory of the Contribution of Excitons to the Complex Dielectric Constant of Crystals, Phys. Rev. **112**, 1555 (1958).

[20] M. Wouters and I. Carusotto, Parametric oscillation threshold of semiconductor microcavities in the strong coupling regime, Phys. Rev. B **75**, 075332 (2007).

[21] M. Wouters, Resonant polariton-polariton scattering in semiconductor microcavities, Phys. Rev. B **76**, 045319 (2007).

[22] M. Richard, J. Kasprzak, R. Romestain, R. André, and L. S. Dang, Spontaneous Coherent Phase Transition of Polaritons in CdTe Microcavities, Phys. Rev. Lett. **94**, 187401 (2005).

[23] M. Richard, J. Kasprzak, R. André, R. Romestain, L. S. Dang, G. Malpuech, and A. Kavokin, Experimental evidence for nonequilibrium Bose condensation of exciton polaritons, Phys. Rev. B **72**, 201301 (2005).

[24] J. Kasprzak, M. Richard, S. Kundermann, A. Baas, P. Jeambrun, J. M. J. Keeling, F. M. Marchetti, M. H. Szymańska, R. André, J. L. Staehli, V. Savona, P. B. Littlewood, D. B., and L. S. Dang, Bose-Einstein condensation of exciton polaritons, Nature **443**, 409 (2006).

[25] C. Ciuti, P. Schwendimann, and A. Quattropani, Theory of polariton parametric interactions in semiconductor microcavities, Semicond. Sci. Technol. **18**, S279 (2003).

[26] R. M. Stevenson, V. N. Astratov, M. S. Skolnick, D. M. Whittaker, M. Emam-Ismail, A. I. Tartakovskii, P. G. Savvidis, J. J. Baumberg, and J. S. Roberts, Continuous Wave Observation of Massive Polariton Redistribution by Stimulated Scattering in Semiconductor Microcavities, Phys. Rev. Lett. **85**, 3680 (2000).

[27] C. Ciuti, P. Schwendimann, and A. Quattropani, Parametric luminescence of microcavity polaritons, Phys. Rev. B **63**, 041303 (2001).

[28] D. M. Whittaker, Classical treatment of parametric processes in a strong-coupling planar microcavity, Phys. Rev. B **63**, 193305 (2001).

[29] L. Pitaevskii and S. Stringari, *Bose-Einstein Condensation*, International Series of Monographs on Physics No. 116 (Oxford University Press, 2003).

[30] A. Amo, J. Lefrère, S. Pigeon, C. Adrados, C. Ciuti, I. Carusotto, R. Houdré, E. Giacobino, and A. Bramati, Superfluidity of polaritons in semiconductor microcavities, Nature Physics **5**, 805 (2009).

[31] A. Amo, D. Sanvitto, F. P. Laussy, D. Ballarini, E. del Valle, M. D. Martin, A. Lemaître, J. Bloch, D. N. Krizhanovskii, M. S. Skolnick, C. Tejedor, and L. Viña, Collective fluid dynamics of a polariton condensate in a semiconductor microcavity, Nature **457**, 291 (2009).

[32] D. Sanvitto, F. M. Marchetti, M. H. Szymańska, G. Tosi, M. Baudisch, F. P. Laussy, D. N. Krizhanovskii, M. S. Skolnick, L. Marrucci, A. Lemaître, *et al.*, Persistent currents and quantized vortices in a polariton superfluid, Nature Physics **6**, 527 (2010).

[33] K. G. Lagoudakis, M. Wouters, M. Richard, A. Baas, I. Carusotto, R. André, L. S. Dang, and B. Deveaud-Plédran, Quantized vortices in an exciton–polariton condensate, Nature Physics **4**, 706 (2008).

[34] J. Keeling, Superfluid Density of an Open Dissipative Condensate, Phys. Rev. Lett. **107**, 080402 (2011).

[35] O. Penrose and L. Onsager, Bose-Einstein Condensation and Liquid Helium, Phys. Rev. **104**, 576 (1956).

[36] N. D. Mermin and H. Wagner, Absence of Ferromagnetism or Antiferromagnetism in One- or Two-Dimensional Isotropic Heisenberg Models, Phys. Rev. Lett. **17**, 1133 (1966).

[37] D. Caputo, D. Ballarini, G. Dagvadorj, C. Sánchez Muñoz, M. De Giorgi, L. Dominici, K. West, L. N. Pfeiffer, G. Gigli, F. P. Laussy, and et al., Topological order and thermal equilibrium in polariton condensates, Nature Materials **17**, 145–151 (2017).

[38] G. Roumpos, M. Lohse, W. H. Nitsche, J. Keeling, M. H. Szymańska, P. B. Littlewood, A. Löffler, S. Höfling, L. Worschech, A. Forchel, and Y. Yamamoto, Power-

law decay of the spatial correlation function in exciton-polariton condensates, Proceedings of the National Academy of Sciences **109**, 6467 (2012).

[39] G. Dagvadorj, J. M. Fellows, S. Matyjaśkiewicz, F. M. Marchetti, I. Carusotto, and M. H. Szymańska, Nonequilibrium Phase Transition in a Two-Dimensional Driven Open Quantum System, Phys. Rev. X **5**, 041028 (2015).

[40] P. Minnhagen, The two-dimensional Coulomb gas, vortex unbinding, and superfluid-superconducting films, Rev. Mod. Phys. **59**, 1001 (1987).

[41] P. Comaron, G. Dagvadorj, A. Zamora, I. Carusotto, N. P. Proukakis, and M. H. Szymańska, Dynamical Critical Exponents in Driven-Dissipative Quantum Systems, Phys. Rev. Lett. **121**, 095302 (2018).

[42] A. Zamora, G. Dagvadorj, P. Comaron, I. Carusotto, N. P. Proukakis, and M. H. Szymańska, Kibble-Zurek Mechanism in Driven Dissipative Systems Crossing a Nonequilibrium Phase Transition, Phys. Rev. Lett. **125**, 095301 (2020).

[43] E. Altman, L. M. Sieberer, L. Chen, S. Diehl, and J. Toner, Two-Dimensional Superfluidity of Exciton Polaritons Requires Strong Anisotropy, Physical Review X **5**, 011017 (2015).

[44] A. Zamora, L. M. Sieberer, K. Dunnett, S. Diehl, and M. H. Szymańska, Tuning across Universalities with a Driven Open Condensate, Phys. Rev. X **7**, 041006 (2017).

[45] A. Amo and J. Bloch, Exciton-polaritons in lattices: A non-linear photonic simulator, Comptes Rendus Physique **17**, 934 (2016).

[46] C. Schneider, K. Winkler, M. D. Fraser, M. Kamp, Y. Yamamoto, E. A. Ostrovskaya, and S. Höfling, Exciton-polariton trapping and potential landscape engineering, Reports on Progress in Physics **80**, 016503 (2016).

[47] C. W. Lai, N. Y. Kim, S. Utsunomiya, G. Roumpos, H. Deng, M. D. Fraser, T. Byrnes, P. Recher, N. Kumada, T. Fujisawa, and Y. Yamamoto, Coherent zero-

state and π-state in an exciton–polariton condensate array, Nature **450**, 529–532 (2007).

[48] N. Y. Kim, K. Kusudo, C. Wu, N. Masumoto, A. Löffler, S. Höfling, N. Kumada, L. Worschech, A. Forchel, and Y. Yamamoto, Dynamical d-wave condensation of exciton–polaritons in a two-dimensional square-lattice potential, Nature Physics **7**, 681–686 (2011).

[49] M. M. de Lima, M. van der Poel, P. V. Santos, and J. M. Hvam, Phonon-Induced Polariton Superlattices, Phys. Rev. Lett. **97**, 045501 (2006).

[50] E. A. Cerda-Méndez, D. Sarkar, D. N. Krizhanovskii, S. S. Gavrilov, K. Biermann, M. S. Skolnick, and P. V. Santos, Exciton-Polariton Gap Solitons in Two-Dimensional Lattices, Phys. Rev. Lett. **111**, 146401 (2013).

[51] D. Tanese, H. Flayac, D. Solnyshkov, A. Amo, A. Lemaître, E. Galopin, R. Braive, P. Senellart, I. Sagnes, G. Malpuech, and J. Bloch, Polariton condensation in solitonic gap states in a one-dimensional periodic potential, Nature Communications **4**, 1749 (2013).

[52] D. Tanese, E. Gurevich, F. Baboux, T. Jacqmin, A. Lemaître, E. Galopin, I. Sagnes, A. Amo, J. Bloch, and E. Akkermans, Fractal Energy Spectrum of a Polariton Gas in a Fibonacci Quasiperiodic Potential, Phys. Rev. Lett. **112**, 146404 (2014).

[53] B. Zhang, S. Brodbeck, Z. Wang, M. Kamp, C. Schneider, S. Höfling, and H. Deng, Coupling polariton quantum boxes in sub-wavelength grating microcavities, Applied Physics Letters **106**, 051104 (2015).

[54] F. Baboux, L. Ge, T. Jacqmin, M. Biondi, E. Galopin, A. Lemaître, L. Le Gratiet, I. Sagnes, S. Schmidt, H. E. Türeci, A. Amo, and J. Bloch, Bosonic Condensation and Disorder-Induced Localization in a Flat Band, Phys. Rev. Lett. **116**, 066402 (2016).

[55] P. St-Jean, V. Goblot, E. Galopin, A. Lemaître, T. Ozawa, L. Le Gratiet, I. Sagnes,

J. Bloch, and A. Amo, Lasing in topological edge states of a one-dimensional lattice, Nature Photonics **11**, 651–656 (2017).

[56] S. Klembt, T. H. Harder, O. A. Egorov, K. Winkler, H. Suchomel, J. Beierlein, M. Emmerling, C. Schneider, and S. Höfling, Polariton condensation in S- and P-flatbands in a two-dimensional Lieb lattice, Applied Physics Letters **111**, 231102 (2017).

[57] S. Klembt, T. Harder, O. Egorov, K. Winkler, R. Ge, M. Bandres, M. Emmerling, L. Worschech, T. Liew, M. Segev, *et al.*, Exciton-polariton topological insulator, Nature **562**, 552 (2018).

[58] C. E. Whittaker, E. Cancellieri, P. M. Walker, D. R. Gulevich, H. Schomerus, D. Vaitiekus, B. Royall, D. M. Whittaker, E. Clarke, I. V. Iorsh, I. A. Shelykh, M. S. Skolnick, and D. N. Krizhanovskii, Exciton Polaritons in a Two-Dimensional Lieb Lattice with Spin-Orbit Coupling, Phys. Rev. Lett. **120**, 097401 (2018).

[59] V. Goblot, B. Rauer, F. Vicentini, A. Le Boité, E. Galopin, A. Lemaître, L. Le Gratiet, A. Harouri, I. Sagnes, S. Ravets, C. Ciuti, A. Amo, and J. Bloch, Nonlinear Polariton Fluids in a Flatband Reveal Discrete Gap Solitons, Phys. Rev. Lett. **123**, 113901 (2019).

[60] M. Milićević, G. Montambaux, T. Ozawa, O. Jamadi, B. Real, I. Sagnes, A. Lemaître, L. Le Gratiet, A. Harouri, J. Bloch, and A. Amo, Type-III and Tilted Dirac Cones Emerging from Flat Bands in Photonic Orbital Graphene, Phys. Rev. X **9**, 031010 (2019).

[61] R. Su, S. Ghosh, J. Wang, S. Liu, C. Diederichs, T. C. H. Liew, and Q. Xiong, Observation of exciton polariton condensation in a perovskite lattice at room temperature, Nature Physics **16**, 301–306 (2020).

[62] N. H. M. Dang, D. Gerace, E. Drouard, G. Trippé-Allard, F. Lédée, R. Mazurczyk, E. Deleporte, C. Seassal, and H. S. Nguyen, Tailoring Dispersion of Room-Temperature Exciton-Polaritons with Perovskite-Based Subwavelength Metasurfaces, Nano Letters **20**, 2113 (2020).

[63] M. Dusel, S. Betzold, O. Egorov, S. Klembt, J. Ohmer, U. Fischer, S. Höfling, and C. Schneider, Room temperature organic exciton-polariton condensate in a lattice, Nature Communications **11**, 2863 (2020).

[64] O. Jamadi, E. Rozas, G. Salerno, M. Milićević, T. Ozawa, I. Sagnes, A. Lemaître, L. Le Gratiet, A. Harouri, I. Carusotto, and et al., Direct observation of photonic Landau levels and helical edge states in strained honeycomb lattices, Light: Science & Applications **9**, 10.1038/s41377-020-00377-6 (2020).

[65] C. Gardiner and P. Zoller, *Quantum Noise* (Springer, 2004).

[66] R. J. Glauber, Coherent and Incoherent States of the Radiation Field, Phys. Rev. **131**, 2766 (1963).

[67] E. C. G. Sudarshan, Equivalence of Semiclassical and Quantum Mechanical Descriptions of Statistical Light Beams, Phys. Rev. Lett. **10**, 277 (1963).

[68] K. Vogel and H. Risken, Quasiprobability distributions in dispersive optical bistability, Phys. Rev. A **39**, 4675 (1989).

[69] P. D. Drummond and C. W. Gardiner, Generalised P-representations in quantum optics, Journal of Physics A: Mathematical and General **13**, 2353 (1980).

[70] P. Deuar and P. D. Drummond, First-principles quantum dynamics in interacting Bose gases: I. The positive P representation, Journal of Physics A: Mathematical and General **39**, 1163 (2006).

[71] A. Gilchrist, C. W. Gardiner, and P. D. Drummond, Positive P representation: Application and validity, Phys. Rev. A **55**, 3014 (1997).

[72] P. D. Drummond and D. F. Walls, Quantum theory of optical bistability. I. Nonlinear polarisability model, Journal of Physics A: Mathematical and General **13**, 725 (1980).

[73] I. Carusotto and C. Ciuti, Spontaneous microcavity-polariton coherence across the parametric threshold: Quantum Monte Carlo studies, Phys. Rev. B **72**, 125335 (2005).

[74] M. Wouters and V. Savona, Stochastic classical field model for polariton condensates, Phys. Rev. B **79**, 165302 (2009).

[75] L. Dominici, G. Dagvadorj, J. M. Fellows, D. Ballarini, M. De Giorgi, F. M. Marchetti, B. Piccirillo, L. Marrucci, A. Bramati, G. Gigli, and et al., Vortex and half-vortex dynamics in a nonlinear spinor quantum fluid, Science Advances **1**, e1500807 (2015).

[76] S. Donati, L. Dominici, G. Dagvadorj, D. Ballarini, M. De Giorgi, A. Bramati, G. Gigli, Y. G. Rubo, M. H. Szymańska, and D. Sanvitto, Twist of generalized skyrmions and spin vortices in a polariton superfluid, Proceedings of the National Academy of Sciences **113**, 14926–14931 (2016).

[77] D. Ballarini, D. Caputo, G. Dagvadorj, R. Juggins, M. D. Giorgi, L. Dominici, K. West, L. N. Pfeiffer, G. Gigli, M. H. Szymańska, and et al., Directional Goldstone waves in polariton condensates close to equilibrium, Nature Communications **11**, 217 (2020).

[78] G. Wachtel, L. M. Sieberer, S. Diehl, and E. Altman, Electrodynamic duality and vortex unbinding in driven-dissipative condensates, Phys. Rev. B **94**, 104520 (2016).

[79] L. M. Sieberer, G. Wachtel, E. Altman, and S. Diehl, Lattice duality for the compact Kardar-Parisi-Zhang equation, Phys. Rev. B **94**, 104521 (2016).

[80] C. W. Gardiner, *Stochastic Methods*, 4th ed. (Springer-Verlag, Berlin, Heidelberg, 2009).

[81] M. Van Regemortel, W. Casteels, I. Carusotto, and M. Wouters, Spontaneous Beliaev-Landau scattering out of equilibrium, Phys. Rev. A **96**, 053854 (2017).

[82] L. M. Sieberer, M. Buchhold, and S. Diehl, Keldysh field theory for driven open quantum systems, Reports on Progress in Physics **79**, 096001 (2016).

[83] F. A. M. de Oliveira, s-order nondiagonal quasiprobabilities, Phys. Rev. A **45**, 5104 (1992).

[84] P. Deuar, *First-principles quantum simulations of many-mode open interacting Bose gases using stochastic gauge methods*, Ph.D. thesis, University of Queensland, arXiv:cond-mat/0507023 (2005).

[85] G. R. Dennis, J. J. Hope, and M. T. Johnsson, XMDS2: Fast, scalable simulation of coupled stochastic partial differential equations, Computer Physics Communications **184**, 201 (2013).

[86] P. Drummond and I. Mortimer, Computer simulations of multiplicative stochastic differential equations, Journal of Computational Physics **93**, 144 (1991).

[87] C. Ciuti and I. Carusotto, Quantum fluid effects and parametric instabilities in microcavities, Phys. Status Solidi B **242**, 2224 (2005).

[88] D. M. Whittaker, Effects of polariton-energy renormalization in the microcavity optical parametric oscillator, Phys. Rev. B **71**, 115301 (2005).

[89] K. Dunnett and M. H. Szymańska, Keldysh field theory for nonequilibrium condensation in a parametrically pumped polariton system, Phys. Rev. B **93**, 195306 (2016).

[90] M. Wouters and I. Carusotto, Goldstone mode of optical parametric oscillators in planar semiconductor microcavities in the strong-coupling regime, Phys. Rev. A **76**, 043807 (2007).

[91] P. G. Savvidis, C. Ciuti, J. J. Baumberg, D. M. Whittaker, M. S. Skolnick, and J. S. Roberts, Off-branch polaritons and multiple scattering in semiconductor microcavities, Phys. Rev. B **64**, 075311 (2001).

[92] A. I. Tartakovskii, D. N. Krizhanovskii, D. A. Kurysh, V. D. Kulakovskii, M. S. Skolnick, and J. S. Roberts, Polariton parametric scattering processes in semiconductor microcavities observed in continuous wave experiments, Phys. Rev. B **65**, 081308 (2002).

[93] F. M. Marchetti and M. H. Szymańska, Vortices in Polariton OPO Superfluids, in *Exciton Polaritons in Microcavities*, Springer Series in Solid-State Sciences, Vol.

172, edited by V. Timofeev and D. Sanvitto (Springer Berlin Heidelberg, 2012) pp. 173–213.

[94] A. A. Demenev, A. A. Shchekin, A. V. Larionov, S. S. Gavrilov, V. D. Kulakovskii, N. A. Gippius, and S. G. Tikhodeev, Kinetics of Stimulated Polariton Scattering in Planar Microcavities: Evidence for a Dynamically Self-Organized Optical Parametric Oscillator, Phys. Rev. Lett. **101**, 136401 (2008).

[95] N. A. Gippius, S. G. Tikhodeev, V. D. Kulakovsii, D. N. Krizhanovskii, and A. I. Tartakovskii, Nonlinear dynamics of polariton scattering in semiconductor microcavity: bistablity vs. stimulated scattering, Europhys. Lett. **67**, 997 (2004).

[96] M. Wouters and I. Carusotto, Absence of long-range coherence in the parametric emission of photonic wires, Phys. Rev. B **74**, 245316 (2006).

[97] S. S. Gavrilov, N. A. Gippius, V. D. Kulakovskii, and S. G. Tikhodeev, Hard mode of stimulated scattering in the system of quasi-two-dimensional exciton polaritons, Journal of Experimental and Theoretical Physics **104**, 715 (2007).

[98] A. C. Berceanu, L. Dominici, I. Carusotto, D. Ballarini, E. Cancellieri, G. Gigli, M. H. Szymańska, D. Sanvitto, and F. M. Marchetti, Multicomponent polariton superfluidity in the optical parametric oscillator regime, Phys. Rev. B **92**, 035307 (2015).

[99] A. Baas, J. P. Karr, H. Eleuch, and E. Giacobino, Optical bistability in semiconductor microcavities, Phys. Rev. A **69**, 023809 (2004).

[100] S. S. Gavrilov, Blowup dynamics of coherently driven polariton condensates, Phys. Rev. B **90**, 205303 (2014).

[101] R. Butté, M. S. Skolnick, D. M. Whittaker, D. Bajoni, and J. S. Roberts, Dependence of stimulated scattering in semiconductor microcavities on pump power, angle, and energy, Phys. Rev. B **68**, 115325 (2003).

[102] D. N. Krizhanovskii, S. S. Gavrilov, A. P. D. Love, D. Sanvitto, N. A. Gippius, S. G. Tikhodeev, V. D. Kulakovskii, D. M. Whittaker, M. S. Skolnick, and J. S.

Roberts, Self-organization of multiple polariton-polariton scattering in semiconductor microcavities, Phys. Rev. B **77**, 115336 (2008).

[103] M. Kardar, G. Parisi, and Y.-C. Zhang, Dynamic Scaling of Growing Interfaces, Phys. Rev. Lett. **56**, 889 (1986).

[104] J. ichi Wakita, H. Itoh, T. Matsuyama, and M. Matsushita, Self-Affinity for the Growing Interface of Bacterial Colonies, Journal of the Physical Society of Japan **66**, 67 (1997).

[105] M. A. C. Huergo, M. A. Pasquale, A. E. Bolzán, A. J. Arvia, and P. H. González, Morphology and dynamic scaling analysis of cell colonies with linear growth fronts, Phys. Rev. E **82**, 031903 (2010).

[106] J. Maunuksela, M. Myllys, O.-P. Kähkönen, J. Timonen, N. Provatas, M. J. Alava, and T. Ala-Nissila, Kinetic Roughening in Slow Combustion of Paper, Phys. Rev. Lett. **79**, 1515 (1997).

[107] M. Myllys, J. Maunuksela, M. Alava, T. Ala-Nissila, J. Merikoski, and J. Timonen, Kinetic roughening in slow combustion of paper, Phys. Rev. E **64**, 036101 (2001).

[108] L. Miettinen, M. Myllys, J. Merikoski, and J. Timonen, Experimental Determination of KPZ Height-Fluctuation Distributions, Eur. Phys. J. B **46**, 55 (2005).

[109] K. A. Takeuchi, M. Sano, T. Sasamoto, and H. Spohn, Growing Interfaces Uncover Universal Fluctuations Behind Scale Invariance, Sci. Rep. **1**, 10.1038/srep00034 (2011).

[110] K. A. Takeuchi and M. Sano, Evidence for Geometry-Dependent Universal Fluctuations of the Kardar-Parisi-Zhang Interfaces in Liquid-Crystal Turbulence, Journal of Statistical Physics **147**, 853 (2012).

[111] Y. T. Fukai and K. A. Takeuchi, Kardar-Parisi-Zhang Interfaces with Curved Initial Shapes and Variational Formula, Phys. Rev. Lett. **124**, 060601 (2020).

[112] D. E. Wolf, Kinetic roughening of vicinal surfaces, Phys. Rev. Lett. **67**, 1783 (1991).

[113] L. Chen and J. Toner, Universality for Moving Stripes: A Hydrodynamic Theory of Polar Active Smectics, Phys. Rev. Lett. **111**, 088701 (2013).

[114] T. Halpin-Healy and G. Palasantzas, Universal correlators and distributions as experimental signatures of (2 + 1)-dimensional Kardar-Parisi-Zhang growth, EPL (Europhysics Letters) **105**, 50001 (2014).

[115] V. G. Miranda and F. D. A. Aarão Reis, Numerical study of the Kardar-Parisi-Zhang equation, Phys. Rev. E **77**, 031134 (2008).

[116] A. Pagnani and G. Parisi, Numerical estimate of the Kardar-Parisi-Zhang universality class in (2+1) dimensions, Phys. Rev. E **92**, 010101 (2015).

[117] L. M. Sieberer and E. Altman, Topological Defects in Anisotropic Driven Open Systems, Phys. Rev. Lett. **121**, 085704 (2018).

[118] T. C. H. Liew and V. Savona, Single Photons from Coupled Quantum Modes, Phys. Rev. Lett. **104**, 183601 (2010).

[119] M. Bamba, A. Imamoğlu, I. Carusotto, and C. Ciuti, Origin of strong photon antibunching in weakly nonlinear photonic molecules, Phys. Rev. A **83**, 021802 (2011).

[120] M. Bamba and C. Ciuti, Counter-polarized single-photon generation from the auxiliary cavity of a weakly nonlinear photonic molecule, Applied Physics Letters **99**, 171111 (2011).

[121] S. Ferretti, L. C. Andreani, H. E. Türeci, and D. Gerace, Photon correlations in a two-site nonlinear cavity system under coherent drive and dissipation, Phys. Rev. A **82**, 013841 (2010).

[122] H. Flayac and V. Savona, Input-output theory of the unconventional photon blockade, Phys. Rev. A **88**, 033836 (2013).

[123] S. Ferretti, V. Savona, and D. Gerace, Optimal antibunching in passive photonic devices based on coupled nonlinear resonators, New Journal of Physics **15**, 025012 (2013).

[124] T. C. H. Liew and V. Savona, Multimode entanglement in coupled cavity arrays, New Journal of Physics **15**, 025015 (2013).

[125] D. Gerace and V. Savona, Unconventional photon blockade in doubly resonant microcavities with second-order nonlinearity, Phys. Rev. A **89**, 031803 (2014).

[126] X.-W. Xu and Y. Li, Strong photon antibunching of symmetric and antisymmetric modes in weakly nonlinear photonic molecules, Phys. Rev. A **90**, 033809 (2014).

[127] M.-A. Lemonde, N. Didier, and A. A. Clerk, Antibunching and unconventional photon blockade with Gaussian squeezed states, Phys. Rev. A **90**, 063824 (2014).

[128] H. Flayac and V. Savona, Single photons from dissipation in coupled cavities, Phys. Rev. A **94**, 013815 (2016).

[129] H. Flayac and V. Savona, Unconventional photon blockade, Phys. Rev. A **96**, 053810 (2017).

[130] H. J. Snijders, J. A. Frey, J. Norman, H. Flayac, V. Savona, A. C. Gossard, J. E. Bowers, M. P. van Exter, D. Bouwmeester, and W. Löffler, Observation of the Unconventional Photon Blockade, Phys. Rev. Lett. **121**, 043601 (2018).

[131] C. Vaneph, A. Morvan, G. Aiello, M. Féchant, M. Aprili, J. Gabelli, and J. Estève, Observation of the Unconventional Photon Blockade in the Microwave Domain, Phys. Rev. Lett. **121**, 043602 (2018).

[132] M. Biondi, E. P. L. van Nieuwenburg, G. Blatter, S. D. Huber, and S. Schmidt, Incompressible Polaritons in a Flat Band, Phys. Rev. Lett. **115**, 143601 (2015).

[133] M. Hyrkäs, V. Apaja, and M. Manninen, Many-particle dynamics of bosons and fermions in quasi-one-dimensional flat-band lattices, Phys. Rev. A **87**, 023614 (2013).

[134] R. Ng, E. S. Sørensen, and P. Deuar, Simulation of the dynamics of many-body quantum spin systems using phase-space techniques, Phys. Rev. B **88**, 144304 (2013).

[135] S. Mandt, D. Sadri, A. A. Houck, and H. E. Türeci, Stochastic differential equations for quantum dynamics of spin-boson networks, New Journal of Physics **17**, 053018 (2015).

[136] R. Ng and E. S. Sørensen, Exact real-time dynamics of quantum spin systems using the positive-P representation, J. Phys. A **44**, 065305 (2011).

[137] J. Huber, P. Kirton, and P. Rabl, Phase-Space Methods for Simulating the Dissipative Many-Body Dynamics of Collective Spin Systems, SciPost Phys. **10**, 45 (2021).

[138] A. Nunnenkamp, J. Koch, and S. M. Girvin, Synthetic gauge fields and homodyne transmission in Jaynes–Cummings lattices, New Journal of Physics **13**, 095008 (2011).

[139] T. Grujic, S. R. Clark, D. Jaksch, and D. G. Angelakis, Non-equilibrium many-body effects in driven nonlinear resonator arrays, New Journal of Physics **14**, 103025 (2012).

[140] F. Nissen, S. Schmidt, M. Biondi, G. Blatter, H. E. Türeci, and J. Keeling, Nonequilibrium Dynamics of Coupled Qubit-Cavity Arrays, Phys. Rev. Lett. **108**, 233603 (2012).

[141] A. A. Houck, H. E. Türeci, and J. Koch, On-chip quantum simulation with superconducting circuits, Nature Physics **8**, 292 (2012).

[142] S. Schmidt and J. Koch, Circuit QED lattices: Towards quantum simulation with superconducting circuits, Annalen der Physik **525**, 395 (2013).

[143] C. Noh and D. G. Angelakis, Quantum simulations and many-body physics with light, Reports on Progress in Physics **80**, 016401 (2016).

[144] P. Deuar and P. D. Drummond, First-principles quantum dynamics in interacting Bose gases: II: stochastic gauges, Journal of Physics A: Mathematical and General **39**, 2723 (2006).

[145] A. J. Kollár, M. Fitzpatrick, and A. A. Houck, Hyperbolic lattices in circuit quantum electrodynamics, Nature **571**, 45–50 (2019).